

**A Thesis Submitted for the Degree of PhD at the University of Warwick**

**Permanent WRAP URL:**

<http://wrap.warwick.ac.uk/93665>

**Copyright and reuse:**

This thesis is made available online and is protected by original copyright.

Please scroll down to view the document itself.

Please refer to the repository record for this item for information to help you to cite it.

Our policy information is available from the repository home page.

For more information, please contact the WRAP Team at: [wrap@warwick.ac.uk](mailto:wrap@warwick.ac.uk)



**Approaches to Scaling Phenomena in Space and  
Laboratory Plasma**

by

**Bogdan A. Hnat**

**Thesis**

Submitted to the University of Warwick

for the degree of

**Doctor of Philosophy**

**Physics**

January 2003

616631 632



[Cross]

D 15

2003

15

# Contents

<b>List of Tables</b>	<b>iv</b>
<b>List of Figures</b>	<b>v</b>
<b>Acknowledgments</b>	<b>ix</b>
<b>Declarations</b>	<b>x</b>
<b>Abstract</b>	<b>xi</b>
<b>Abbreviations</b>	<b>xiii</b>
<b>Chapter 1 Introduction</b>	<b>1</b>
1.1 General concepts . . . . .	1
1.1.1 Self-Organized Criticality. Sandpile models . . . . .	5
1.1.2 Turbulence . . . . .	7
1.2 Tokamak plasma . . . . .	11
1.3 Solar wind . . . . .	13
<b>Chapter 2 Models and Methods</b>	<b>19</b>
2.1 Our sandpile model . . . . .	20
2.1.1 Renormalization Group . . . . .	23
2.1.2 System Dynamics . . . . .	26
2.2 Fokker-Planck equation . . . . .	31
2.2.1 Stochastic Markov process and Fokker-Planck Equation . . .	31



2.2.2	Finite size scaling for turbulent systems. . . . .	34
2.2.3	Finite size scaling for spatially extended systems. . . . .	37
2.3	Fractal analysis . . . . .	41
2.3.1	Self-similarity and fractal dimension of time series . . . . .	42
2.3.2	Embedding, phase space reconstruction and fractal dimension of the attractor . . . . .	45
<b>Chapter 3</b>	<b>Scientific Visualization and Data Mining</b>	<b>49</b>
3.1	Virtual Reality and Scientific Visualization . . . . .	50
3.1.1	System and Application Overview . . . . .	51
3.1.2	Visualization Methods . . . . .	53
3.1.3	Data Set Reduction and Surface Optimization . . . . .	54
3.1.4	Data Mining and Visualization Results . . . . .	56
3.1.5	Quantitative Sonification . . . . .	58
3.1.6	Conclusions . . . . .	60
<b>Chapter 4</b>	<b>Statistical Analysis of the Sandpile Model</b>	<b>61</b>
4.1	Finite size scaling for the sandpile model . . . . .	62
4.2	Self-similarity and length scaling of the time series . . . . .	67
4.3	Phase Space Reconstruction . . . . .	72
4.3.1	Constant critical gradient . . . . .	73
4.3.2	Randomized critical gradient . . . . .	77
4.4	Conclusions . . . . .	80
<b>Chapter 5</b>	<b>Modeling tokamak plasmas with the Sandpile Model</b>	<b>82</b>
5.1	Tokamak-like enhanced confinement phenomenology from the sand- pile model . . . . .	83
5.2	Self Organization of Edge and Internal Pedestals in a Sandpile . . .	88
5.3	Conclusions . . . . .	94
<b>Chapter 6</b>	<b>Intermittency, scaling and a Fokker-Planck approach to</b>	

<b>solar wind fluctuations and coupled solar wind-magnetosphere system</b>	<b>96</b>
6.1 The Dataset . . . . .	97
6.2 Estimates of the rescaling index . . . . .	99
6.3 Scaling in the solar wind bulk plasma parameters . . . . .	100
6.4 Scaling in the solar wind $\epsilon$ and geomagnetic indices . . . . .	105
6.5 Modelling the data . . . . .	108
6.5.1 Diffusion model . . . . .	109
6.5.2 Castaing model . . . . .	111
6.6 Conclusions . . . . .	113
<b>Chapter 7 Conclusions</b>	<b>115</b>
7.1 Conclusions from the sandpile model study . . . . .	115
7.1.1 Qualitative results . . . . .	116
7.1.2 Quantitative results . . . . .	117
7.1.3 Application of the sandpile model . . . . .	119
7.2 Conclusions from the finite size scaling and a Fokker-Planck approach to space plasmas . . . . .	120
7.2.1 Solar wind fluctuations . . . . .	121
7.2.2 Coupled solar wind-magnetosphere system . . . . .	122
7.2.3 Results from the Fokker-Planck model . . . . .	122
7.3 Future work . . . . .	123
<b>Appendix A Fokker-Planck model of solar wind fluctuations</b>	<b>125</b>
<b>Appendix B Langevin equation for solar wind fluctuations</b>	<b>127</b>

# List of Tables

1.1	Typical parameters of tokamak plasmas. . . . .	12
3.1	Data set size before and after optimization. . . . .	57
6.1	Typical parameters of the solar wind at 1AU. . . . .	99
6.2	Scaling indices for solar wind quantities. . . . .	102
6.3	Scaling indices for magnetospheric quantities. . . . .	107

# List of Figures

1.1	Complex turbulent flow. . . . .	8
1.2	Magnetic field generation in Tokamak . . . . .	14
1.3	The coupled solar wind-magnetosphere-ionosphere system. . . . .	16
2.1	Schematic of the sandpile algorithm. . . . .	20
2.2	Phase space plots of the sandpile stationary state. . . . .	22
2.3	Reducing the complexity of the system via Renormalization. . . . .	23
2.4	RG coarse-graining procedure for the sandpile model. . . . .	23
2.5	System dynamics for system length $N = 1024$ with $L_f = N$ and $L_f = 200$ . . . . .	26
2.6	System dynamics for system length $N = 1024$ with $L_f = N$ and $L_f = 200$ and randomized critica gradient. . . . .	28
2.7	Mean normalized energy stored in the system and mean height profile. 30	
2.8	Integrated Brownian walk and the PDFs of increments. . . . .	35
2.9	PDF rescaling of a Brownian walk (1). . . . .	36
2.10	PDF rescaling of a Brownian walk (2). . . . .	38
2.11	Example of a fractal curve–von Koch snowflake. . . . .	41
2.12	Length scaling of the curve . . . . .	44
2.13	Von Koch curve fractal dimension estimation. . . . .	45
3.1	The interface of the sandpile simulation. . . . .	52
3.2	Vertex reduction method based on the normal vector direction change. 54	

3.3	(a): State variable (total energy) of the sandpile dynamics and (b) corresponding 3-D view of the sandpile height profile. . . . .	56
3.4	3-D visualization of the sandpile height profiles. . . . .	59
4.1	Probability Distribution Function of the avalanche lengths and dissipated energy. . . . .	63
4.2	Finite size scaling of the sandpile model for $L_f = N$ . . . . .	64
4.3	PDFs of the avalanche lengths and dissipated energy away from criticality. . . . .	65
4.4	Finite size scaling of avalanche lengths and dissipated energy away from criticality. . . . .	66
4.5	Reconstruct the energy time series. . . . .	68
4.6	Fractal dimension estimation for the energy time series obtained through the successive midpoint division. . . . .	70
4.7	Total energy time series for the sandpile with various parameters $L_f$ . . . . .	71
4.8	Curve length scaling for the energy time series. . . . .	72
4.9	Phase space structures for the sandpile with various parameters $L_f$ . . . . .	74
4.10	Mutual information and the local slope of the correlation sum. $L_f = N$ and constant critical gradient. . . . .	75
4.11	Mutual information and the local slope of the correlation sum. $L_f = N/2$ and constant critical gradient. . . . .	76
4.12	Mutual information and the local slope of the correlation sum. $L_f = 48$ and constant critical gradient. . . . .	77
4.13	Mutual information and the local slope of the correlation sum. $L_f = N$ and randomized critical gradient. . . . .	78
4.14	Mutual information and the local slope of the correlation sum. $L_f = N/2$ and randomized critical gradient. . . . .	79
4.15	Mutual information and the local slope of the correlation sum. $L_f = 48$ and randomized critical gradient. . . . .	80

5.1	Time averaged height profiles of the 512 cell sandpile for $L_f =$ (a)50, (b)150, and (c)250. Inset: edge structure. . . . .	84
5.2	Time evolution of the 512 cell sandpile with $L_f = 50$ . . . . .	84
5.3	As in figure 5.2, for $L_f = 150$ . . . . .	85
5.4	As in figure 5.2, for $L_f = 250$ . . . . .	85
5.5	Energy confinement versus ELM frequency from $H_{98}$ (top) and $H_{93}$ (bottom) measurements. Solid curve corresponds to the model developed in <i>Fishpool</i> (1998). . . . .	87
5.6	Average stored energy versus MLE frequency. . . . .	87
5.7	Time evolution of (top) stored energy, (middle) sandpile edge position, and (lower) MLEs, as $L_f$ changes slowly and linearly from 250 to 50. . . . .	88
5.8	3D view of the sandpile height profile for $L_f = 50$ . . . . .	88
5.9	Time evolution of the electron temperature at various major radii for DIII-D discharge No. 94100 ( <i>Kinsey et al.</i> , 2001). . . . .	90
5.10	Local height of sand as a function of time at different locations in the sandpile. . . . .	90
5.11	Location of cells where the value of the local gradient exceeds $g_c/2$ for (a) $L_f = 50$ and (b) $L_f = 250$ . . . . .	91
5.12	Local gradient normalized to the local value of $g_c$ for cells at the edge and halfway into the sandpile. . . . .	93
5.13	Phase space reconstruction of the dynamics of the edge position $ep(t)$ . . . . .	94
6.1	Unscaled PDFs of the ion density fluctuations . . . . .	98
6.2	Scaling of the PDF peaks for solar wind quantities. . . . .	100
6.3	One parameter rescaling of the PDF for solar wind fluctuations. . . . .	101
6.4	Direct comparison of the fluctuation PDFs for solar wind. . . . .	103
6.5	One parameter rescaling of the PDF for $\delta B$ and $\delta v$ . . . . .	104
6.6	Unscaled PDFs of the AE index fluctuations. . . . .	105
6.7	Scaling of the PDF peaks for magnetosperic quantities. . . . .	106
6.8	One parameter rescaling of the PDF for magnetospheric fluctuations. . . . .	108

6.9	Direct comparison of the fluctuations PDFs for $\epsilon$ ( $\diamond$ ) and AE index ( $\circ$ ). Insert shows overlaid PDFs of $AU(\square)$ and $-AL(\triangle)$ fluctuations.	109
6.10	Example of the fit of the PDF functional form predicted by a Fokker-Planck description (6.4) (solid line) and a Castaing model (dash line) to the fluctuations PDF of the $\delta(\rho v^2)$ bulk parameter. . . . .	112

# Acknowledgments

I would like to thank my supervisor, Prof. Sandra Chapman, for giving me the opportunity to do this PhD and for her continued support over the last four years.

I also thank Prof. George Rowlands for his invaluable advise and contribution to many parts of this work. My thanks also extend to Dr. Nicholas Watkins (BAS) and Dr. Richard Dendy (UKAEA) for many inspirational ideas and useful discussions concerning this research. Many thanks to all the members of the Space & Astrophysics Group, past and present, for providing an enjoyable working environment.

The computational resources, without which this research would not have been possible, were funded by the Particle Physics and Astronomy Research Council (PPARC) and the Higher Education Funding Council for England (HEFCE). This includes usage of GOCHIP and the Virtual Reality CAVE system (SGI Onyx2 at the Space & Astrophysics Group, University of Warwick).

I would like to acknowledge R. P. Lepping and K. Ogilvie from NASA for provision of data from the NASA WIND spacecraft and the World Data Center C2, Kyoto for geomagnetic indices. I thank N. W. Watkins and M. P. Freeman for advice concerning the post processing of data.

This PhD was founded by a PPARC studentship.



# Declarations

I hereby declare that this is my own work, except where explicitly stated, and that it has not been submitted for a degree at the University of Warwick, or any other university.

Bogdan A. Hnat.

November 2002.

# Abstract

Many laboratory and space plasma phenomena exhibit scaling, i.e., no characteristic spatial and/or temporal scale can be identified in their dynamics. This lack of a characteristic scale makes the dynamics of these systems extremely complex and intractable to analytical approaches. Their statistical features, however, appear to be simple and exhibit a degree of universality. We will explore two approaches to scaling in plasma systems, one based on avalanching sandpile model and the second one based on turbulence.

The avalanching model developed here exhibits a wide range of dynamic behavior and incorporates other established models as limiting cases. A single control parameter that specifies the length scale over which the redistribution rule operates compared to the finite system size, allows us to explore different regimes of the model's dynamics close to and away from the existing fixed points. An advanced Virtual Reality visualization technique was employed to gain a better qualitative understanding of the sandpile behavior in the parameter space. This sandpile model was used to simulate features found in the fusion plasma in both low and high confinement modes. Because of the simplicity of this model, it was possible to formally characterize and explain the mechanisms underlying steep gradients formation and appearance of internal transport barriers, and to identify links to tokamak plasma behavior.

The solar wind is a supersonic, super-Alfvénic flow of compressible and inhomogeneous plasma from the Sun. The solar wind provides a natural laboratory for observations of MHD turbulence over extended temporal scales. In this case a generic and model independent method of differencing and rescaling was applied to identify self-similarity in the Probability Density Functions (PDF) of fluctuations in solar wind bulk plasma parameters as seen by the WIND spacecraft. The single curve, which we found to describe the fluctuations PDF of some quantities, is non-Gaussian. We model this PDF with two approaches—Fokker-Planck, for which we derived the transport coefficients and associated Langevin equation, and the Castaing distribution that arises from a model for the intermittent turbulent cascade. The technique was also used to quantify the statistical properties of fluctuations in the coupled solar wind-magnetosphere system. These quantitative and model-independent results place important constraints on models for the coupled solar wind-magnetosphere system.



# Abbreviations

AE Auroral Electrojet index

AL Auroral Lower bound index

AU Auroral Upper bound index

ELM Edge Localized Mode

EFDA European Fusion Development Agreement

CHAWS Charge Hazards and Wake Studies

CML Coupled Map Lattices

$n$ D  $n$ -dimensional

F-P Fokker-Planck

FPE Fokker-Planck Equation

FSOC Forced Self-Organized Criticality

H-mode High Confinement mode

IMF Interplanetary Magnetic Field

JET Joint European Torus

L-mode Low Confinement mode

LOD Level of Details

MFI Magnetic Fields Instrument

MHD MagnetoHydroDynamics

MLE Mass Loss Events

NASA National Aeronautics and Space Administration

PDF Probability Density Function

PDIF Probability Distribution Function

RG Renormalization Group

SOC Self-Organized Criticality

SWE Solar Wind Experiment

TIN Triangulated Irregular Network

VR Virtual Reality

# Chapter 1

## Introduction

### 1.1 General concepts

A large class of physical phenomena can be characterized as dynamic processes occurring on many different spatial and temporal scales. Ordinarily a set of distinct scales, independent or weakly coupled, can be identified and the physical theories are then developed to treat the dynamics on each scale separately. Let us imagine, for example, that local 15 minutes averaged measurements of temperature are used to develop a linear dynamical model for the weather prediction. Such measurements will clearly reveal several important temporal scales. The temperature at night will be usually much lower than during the day. Seasonal changes will be noticeable when time scales longer than a year are considered. Finally, long term processes, such as these related to ocean currents changes, may be detected for data samples that span very long (several years) periods. Which of these processes need to be taken into account for the weather prediction model depends on the temporal scale of interest. To model observed changes in the temperature during one week, we do not have to include seasonal changes or other processes with long characteristic temporal scales. Similarly, in the description of long and systematic changes of the climate, 24 hours and seasonal cycles are clearly irrelevant.

The dynamical theory of plasma, where a hierarchy of scales can be identified, is also a good example of such an approach. The most detailed descrip-

tion of the plasma is given by a Liouville equation. Let  $j$ th particle in the system be specified by its phase space coordinates  $(\mathbf{x}_j, \mathbf{v}_j)$ , which we will abbreviate as  $X_j$ . A Liouville probability density  $f_L(X_j, t)$ , defined in such way that  $f_L(X_1, \dots, X_N, t)dX_1 \dots dX_N$  gives the probability that the system is in state  $[(X_1, X_1 + dX_1), \dots, (X_N, X_N + dX_N)]$  at time  $t$ , satisfies the Liouville equation (*Clemmow and Dougherty, 1990*):

$$\frac{\partial f_L}{\partial t} + \sum_{j=1}^N \mathbf{v}_j \frac{\partial f_L}{\partial \mathbf{x}_j} + \sum_{j=1}^N \mathbf{a}_j \frac{\partial f_L}{\partial \mathbf{v}_j} = 0. \quad (1.1)$$

Here  $\mathbf{a}_j$  is an exact acceleration of the  $j$ th particle due to all the other particles, without any smoothing. Solving such large number of equations is both impossible and not informative. A simplified approach is to consider a phase space of a single particle. This leads to Boltzmann's one-particle probability distribution equation (*Krall and Trivelpiece, 1986*):

$$\frac{\partial f}{\partial t} + \mathbf{v} \frac{\partial f}{\partial \mathbf{x}} + \frac{q}{m} \langle \mathbf{E} + \frac{\mathbf{v} \times \mathbf{B}}{c} \rangle \frac{\partial f}{\partial \mathbf{v}} = \left( \frac{\partial f}{\partial t} \right)_c, \quad (1.2)$$

where  $\langle \mathbf{E} \rangle$  and  $\langle \mathbf{B} \rangle$  represent a sum of all external and averaged internal fields. The latter satisfy Maxwell's equations:

$$\nabla \cdot \langle \mathbf{E} \rangle = 4\pi \langle \rho \rangle \quad \text{and} \quad \nabla \times \langle \mathbf{B} \rangle = \frac{1}{c} \frac{\partial \langle \mathbf{E} \rangle}{\partial t} + \frac{4\pi}{c} \langle \mathbf{J} \rangle. \quad (1.3)$$

Probability density  $f \equiv f(\mathbf{x}, \mathbf{v}, t)$  in (1.2) is defined so that  $f d^3x d^3v$  gives a number of particles in the range  $(\mathbf{x}, \mathbf{x} + d\mathbf{x})$ ,  $(\mathbf{v}, \mathbf{v} + d\mathbf{v})$ . The right-hand side of (1.2) is the effect of collisions between near-neighbor particles. The first characteristic scale of the plasma dynamics can be associated with the mean free path  $\ell_{mfp}$ , i.e., the mean distance that a particle moves between two successive collisions. If the phenomena of interest occurs on the scale  $L_c$  that is much shorter than  $\ell_{mfp}$ , the collision term in (1.2) can be neglected. In the same regime, where  $L_c \ll \ell_{mfp}$ , the motion of the individual charge can be studied using classical mechanics with the Lorentz force included in the Hamiltonian. If the length scale  $L_c$  is larger than a gyro radius given by

$$R_g = \frac{mv_{\perp}}{|q|B} \quad (1.4)$$

where  $v_{\perp}$  is a velocity perpendicular to the magnetic field  $B$ , a so called guiding center approach can be used (*Krall and Trivelpiece*, 1986). In the opposite case, when  $L_c \gg \ell_{mfp}$ , the collision term in (1.2) has to be prescribed. The Boltzmann equation, however, is often too detailed for large systems and a different set of approximations can be used to obtain a simplified set of equations on the relevant scale. Taking the limits of the infinite system size  $L \rightarrow \infty$  and small frequency  $\omega \rightarrow 0$  magnetohydrodynamical (MHD) equations can be derived (*Clemmow and Dougherty*, 1990; *Jackson*, 1975) where the particles are treated as a fluid and variations of local quantities are described by differential equations. The incompressible MHD equations relate magnetic field  $\mathbf{B}$ , plasma velocity  $\mathbf{v}$ , pressure  $P$  and density  $\rho$ :

$$\partial_t \rho + \nabla(\rho \mathbf{v}) = 0, \quad (1.5)$$

$$\partial_t \mathbf{v} + (\mathbf{v} \nabla) \mathbf{v} = -\frac{1}{\rho} \nabla P - \frac{1}{\rho \mu_0} \mathbf{B} \times (\nabla \times \mathbf{B}), \quad (1.6)$$

$$\partial_t \mathbf{B} = \nabla \times (\mathbf{v} \times \mathbf{B}), \quad (1.7)$$

$$\frac{D}{Dt} \left( \frac{P}{\rho^\gamma} \right) = 0. \quad (1.8)$$

Here  $\partial_t$  denotes a partial derivative with respect to time and  $\gamma$  is the ratio of the specific heat at constant pressure to that at constant volume ( $\gamma = 5/3$  for a monoatomic gas). In the case where ions and electrons need to be treated separately due to, for example, a large temperature difference between them, a two fluid description of the plasma can be invoked.

The above-described approach fails when the relevant dominant scale can not be identified in a given system. Its evolution is then equally influenced by all spatial or/and temporal scales. We will refer to such phenomena as a complex system. One could point out the abundance of such systems in nature (*Jensen*, 1998; *Bohr et al.*, 1998), here we mention just one. Bursty turbulent magnetic reconnection is a crucial process in understanding the dynamics of the Earth magnetotail, dynamics of Sun



and the processes occurring in the solar wind. Turbulent reconnection leading to the change in the magnetic field topology can occur in the system with non-zero resistivity and large magnetic field gradients. During this process a large amount of energy is released and plasma is accelerated to very high velocities. These effects must be included in any proper description of the plasma systems mentioned above. MHD equations, used to describe the magnetotail dynamics, can not, however, completely model these effects as the reconnection requires localized breaking of the frozen-in condition. This break usually occurs on distances comparable to the gyro radius where the MHD approximation fails. The underlying nonlinear dynamics of such multi-scale confined plasma systems prohibits the use of the traditional electrodynamics and fluid equations. To study these systems, a different approach can be taken. A simple model, capable of reproducing the features of the original system, is constructed and the emergent phenomenology of this model is used to explain the dynamics of the physical system. Examples are shell models, coupled map lattices (*Kaneko, 1992*) (which are reversible on the micro scale) and avalanche (sandpile) models (which on the micro scale have some hysteresis or irreversibility) (*Vlahos et al., 1995*). All these models have similar essential features. They exhibit self-similar and nontrivial (fractal) scaling and long range correlations. Their advantage is in their simplicity. Numerical implementations of these models do not require large computational resources. Some of them are also tractable to Renormalization Group and other dynamical systems approaches.

The statistical features of complex systems are of great importance as they seem to represent the unifying and simplifying aspect of their dynamics. Namely, many systems of interest exhibit a power law distribution of the relevant physical quantities. Such power laws could arise from a strong coupling between all scales relevant to the system's dynamics. We note that a power law  $P(x) \propto x^s$  exhibits a natural lack of scale as a relative change  $P(kx)/P(x) \propto k^s$  is independent of the scale  $x$ . It can be shown that power law statistics are consistent with long range correlations within the system (*Jensen, 1998; Sornette, 2000*). Intriguingly, these features may lead to the development of fractal spatio-temporal patterns found

in many complex systems. Although such statistical features are indicative of the multi-scale behavior they, do not provide a unambiguous test for the existence of the complex dynamics. Indeed, in *Jensen* (1998) the  $1/f$  power law was obtained from the linear superposition of many signals, each exhibiting exponentially decaying autocorrelation function. Thus any description of the complex system's dynamics must include the general statistical features, as discussed before, and other specific characteristics such as the existence of the self-similar energy cascade in space assumed in most turbulence models. Here we will investigate two manifestations of complex systems, Self-Organized Criticality (SOC) and turbulence and their relevance to confined plasma phenomena. Both, SOC and turbulence models are capable of reproducing observed statistical features of complex systems but the origin of the underlying self-similarity may be quite different (avalanching vs. semi-local energy cascade). Interestingly, SOC and turbulence can be studied using similar analysis methods such as finite size scaling presented in Chapter 2. The possible relation between avalanching models and turbulence is an important and topical issue of modern physics.

### 1.1.1 Self-Organized Criticality. Sandpile models

Since its introduction in 1987 by Bak, Tang and Wiesenfeld (BTW) Self-Organized Criticality (*Bak et al.*, 1987) attracted much attention from the scientific community. The concept offered a way to treat a whole class of physical systems that exhibit critical behavior (phase transition) without the need of any tuning parameters. The underlying features of these systems are scale invariance, self-similarity and power-law distributions of any observable. These features indicate the existence of long range (spatial and temporal) correlations within the system which in turn leads to the appearance of highly organized structures and fractal patterns (*Hwa and Kardar*, 1992; *Jensen*, 1998; *Sornette*, 2000). The underlying idea of the SOC theory is that the competition between simple dynamical rules, namely a driving process and the diffusive response of the system to that drive, can create a very complex and in some cases, critical behavior.

Over the years, a large number of models that encapsulate the SOC paradigm has been developed (*Sneppen, 1992; Jensen, 1998*). Prototypical models widely used to demonstrate SOC are these of the sandpile (*Ivashkevich and Priezzhev, 1998*). Sandpiles are dissipative systems in which the energy is dissipated through discharge events called avalanches. The phenomenology of the sandpile models has been applied successfully to a variety of physical systems such as earthquakes (*Chen et al., 1991*), biological evolution (*Sole and Manrubia, 1996*) or interface growth (*Sneppen, 1992*). Its applicability to complex, confined plasma systems remains, however, questionable. To date, a number of studies has used sandpile methodology to investigate the dynamics of energy transport in both astrophysical and laboratory plasma systems. These included astrophysical accretion disks (*Mineshige et al., 1994; Dendy et al., 1998*), energy releases in the Earth’s magnetotail (see (*Chang, 1992*) and references therein, (*Chapman et al., 1999; Chapman and Watkins, 2001a*)) as well as nonlocal and non diffusive energy transport processes in laboratory tokamak plasma investigated in *Carreras and Newman (1996); Chapman et al. (2001c)*. All sandpile models feature thresholded dynamics and as such exhibit local stepwise instability, i.e., the stability of the model is determined by the value of the local gradient  $g_i$ . If the value of  $g_i$  at some point  $i$  is larger then the threshold the sand will be redistributed down the pile. Different realizations of the sandpile model are obtained by varying the redistribution rules (i.e., microscopic dynamical rules) as well as the driving methods. These changes do not necessarily lead to a detectable variation in the global behavior (for example, observed power law indices) thus allowing one to categorize models by means of the universality classes (*Amaral and Lauritsen, 1997; Kadanoff et al., 1989*). Despite many differences between existing “classical” sandpile models, there is one feature shared by all of them – the relaxation of the system is much faster than the growth rate of the instability (drive). Recent studies of standard sandpile models strongly suggest that this separation of time scales is absolutely necessary for the emergence of critical behavior in spatially extended systems (*Hwa and Kardar, 1992*). In essence, it has been proposed that the driving rate  $\lambda$  is a tuning parameter for the sandpile model, similar to these found

in the ordinary systems exhibiting phase transition. The criticality then emerges as a limiting behavior of the system with the constant driving rate  $\lambda \rightarrow 0$  (*Vespignanni and Zapperi*, 1997, 1998). This result is hard to reconcile with apparent ubiquity of SOC in nature where the driving rate is often strong and highly variable. Yet, statistical features found in the observed time series are very similar to these of classic SOC models, strongly suggesting the presence of criticality (*Lu and Hamilton*, 1995; *Dendy et al.*, 1998; *Chapman et al.*, 2001b).

Indeed, the problem of applicability of the sandpile models, and SOC in general, to natural phenomena can not be understated. The microscopic rules are often prescribed arbitrarily, without any apparent physical motivation. Additionally, results of the Renormalization Group analysis are obtained only in the limit of infinite system size. These results may not be relevant for the finite size natural systems. These difficulties motivated the development of a new sandpile model presented in the next section. The model exhibits a wide range of dynamic behavior and incorporates other established models as limiting cases. Self-similar behavior on the large scale is robust against strong and variable driver (*Chapman et al.*, 1999; *Watkins et al.*, 1999). A single control parameter that specifies the length scale over which the redistribution rule operates compared to the finite system size, allows us to explore different regimes of the model's dynamics close to and away from the critical regime. Within certain range of this control parameter, the system exhibits features characteristic of SOC dynamics. Another regime has been also identified where features reminiscent of low-dimensional chaos, such as inverse cascade structures, intermittency and period doubling of a limit cycle, emerge (*Chapman*, 2000). Similar to real physical systems, the dynamics of the model can be strongly influenced by both its finite size and its interaction with boundaries.

### 1.1.2 Turbulence

Turbulence is an intrinsically nonlinear and complex phenomenon that, at least on small scales, can be extremely sensitive to the initial and boundary conditions. Figure 1.1 shows one possible realization of the high Reynolds number turbulent flow

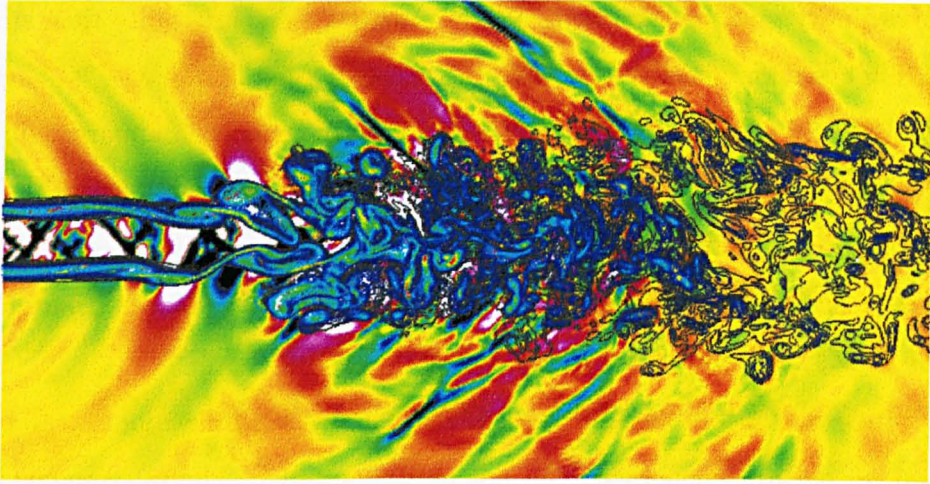


Figure 1.1: Color contours of the vorticity magnitude in Direct Numerical Simulations of supersonic turbulent jet with near acoustic field. The simulations were performed by Jonathan Freund, Parviz Moin and Sanjiva K. Lele. at NASA's Center for Turbulence Research.

obtained by computer simulation. The complexity of the flow is obvious – one can observe the existence of self-similar structures on all scales as well as the emergence of the certain large scale patterns in the flow.

The systematic studies of turbulence started in 1920's when Richardson proposed a mechanism for the creation of turbulence by large scale forcing, that propagates toward the small spatial scales by the nonlinearities of fluid motion. This is often referred to as a spectral paradigm and was later further developed by Kolmogorov in his celebrated 1941 theory (K41). In this work, the Gaussian distributed energy is inputted randomly at large spatial scale. It sets up the nonlinear and semilocal energy cascade that allows the energy to transfer toward smaller and smaller scales until it dissipates due to viscous heating. All scales between the largest one  $L$ , where the energy is injected, and the viscous scale  $\eta$  are referred to as the inertial range  $R$ . The introduction of the inertial range brought universality into studies of turbulence. According to Kolmogorov's theory, the only relevant parameter for the dynamics in the inertial range  $R$ , is the energy flux  $\epsilon$  between different scales. This assumption led Kolmogorov to the development of the dimensional analysis where only  $R$ ,  $\epsilon$  and the fluid density  $\rho$  are considered. Parallel to these theo-

retical predictions, experimental methods were developed to study turbulent flows. Among them, statistical methods proved to be the most robust under perturbations allowing one to extract and characterize (by means of scaling exponents, for example) a macroscopic description of the fluid. Richardson, in his early studies, found that the velocity field itself is too sensitive to the boundary conditions and is not suitable for the statistical measurements. Instead, he suggested the velocity difference  $\delta \mathbf{v}(\mathbf{r}_1, \mathbf{r}_2) = \mathbf{v}(\mathbf{r}_2) - \mathbf{v}(\mathbf{r}_1)$  as an ideal field for statistical studies. Often one dimensional cuts of the velocity fields are considered:

$$\delta v_l(R) = \delta \mathbf{v}(\mathbf{r}_1, \mathbf{r}_2) \cdot \frac{\mathbf{R}}{R}, \quad (1.9)$$

where  $\mathbf{R} = \mathbf{r}_2 - \mathbf{r}_1$  is a separation vector between  $\mathbf{r}_1$  and  $\mathbf{r}_2$ . The main interest lies in the probability distribution function of  $\delta \mathbf{v}(\mathbf{r}_1, \mathbf{r}_2)$  and its moments. These moments are the structure functions and according to Kolmogorov's theory they should scale as:

$$S_n(\mathbf{R}) \equiv \langle \delta v_l(R)^n \rangle \propto (\epsilon \ell)^{n/3}. \quad (1.10)$$

Here,  $n$  is the moment and symbols  $\langle \dots \rangle$  indicate an ensemble average. Experimental results do not confirm that scaling, however, and modification of the theory (Kolmogorov, 1962) includes intermittency by means of randomly varying energy transfer rate  $\epsilon$ . Intermittency modifies scaling of the structure function and experimental data show significant departure of higher moments from these predicted by (1.10). In this context, a plethora of computer models has been suggested to capture this observed scaling. The picture of turbulence emerging from these models is much more complex than that suggested by the original Kolmogorov theory. It requires a multi-fractal phenomenology to be invoked as the self-similarity of the cascade is broken by the introduction of the intermittency. We stress that statistical studies of higher moments of the structure function are very important as the distribution function of the turbulent flows can depart significantly from a Gaussian distribution. This non Gaussian shape of the PDF, corresponding to the increased probability of finding large events, is called statistical intermittency and is most pronounced for small temporal or spatial scales. In a finite sized system, large scale

PDFs should converge to the Gaussian distribution as indicated by the central limit theorem (*Sornette, 2000*).

All aspects of the turbulence, discussed above, are common for neutral fluids and Magnetohydrodynamics. There are, however, some differences in the physics of the magnetized plasma turbulence and we will mention few of them now. One of the profound differences between plasma and the neutral fluid is the variety of linear waves that the plasma can support. This comes from the coupling between charged particles and a self-consistent field that they generate. It is also a result of the linear low frequency solutions of the plasma equations such as (1.5)-(1.8). These oscillations may lead to, so called, weak turbulence where the turbulent eddies, now considered as wave packets, are well separated in space and do not interact (*Krommes, 2002*). The presence of the strong magnetic field  $\mathbf{B}$  introduces a natural anisotropy as the motion in the direction perpendicular to the field is strongly suppressed. This makes MHD turbulence to be in some sense a 2-D phenomenon, while the neutral-fluid turbulence occurs in three dimensions. We should mention here that 2-D and 3-D turbulence is quite different and the differences in the scaling indices are detectable (see for example, *Biskamp (1993)*) in simulations. For experimental reasons, the ability to estimate the extent of the inertial range is very important as it is within this range of spatial scales that the theoretical predictions can be applied. The development of a well-defined inertial range can be strongly inhibited in a plasma due to the linear dissipation mechanisms such as Landau damping (*Krommes, 2002*). Significant differences may also arise from the existence of additional invariants of motion, associated with the magnetic field, in MHD. It can be shown (*Biskamp, 1993*) that equations (1.5)-(1.8) have three quadratic invariants, namely total energy:

$$\mathcal{E} = \frac{1}{2} \int_0^\infty (v^2 + B^2) d^3x, \quad (1.11)$$

the cross-helicity defined as

$$\mathcal{K} = \int_0^\infty \mathbf{v} \cdot \mathbf{B} d^3x, \quad (1.12)$$



and the magnetic helicity

$$\mathcal{H} = \int_0^\infty \mathbf{A} \cdot \mathbf{B} d^3x, \quad (1.13)$$

where  $\mathbf{A}$  is a magnetic potential. In two dimensions, magnetic helicity is replaced by the mean square magnetic potential. These invariants are conserved in a turbulent flow. Their spectral components, defined in the wave number  $k$  space, must obey strict energy conservation relations. If any of these quantities are injected (excited) into a turbulent system all other modes in  $k$  space will be excited as well (*Biskamp*, 1993; *Paret and Tabeling*, 1998). Such a nonlocal (in  $k$  space) transfer process is called cascade and was already mentioned. Recent experimental results from *Paret and Tabeling* (1998); *Biskamp* (1993) confirm the cascade of the total energy and the inverse cascade of the magnetic helicity in 3-D as well as the mean square magnetic potential  $A$  in 2-D turbulence. It was also found that the inverse cascade leads to self-organization and emergence of large magnetic structures as well as an alignment of currents  $\mathbf{j}$  and magnetic field  $\mathbf{B}$  (*Biskamp*, 1993; *Krommes*, 2002).

The experimental observations of plasma turbulence are extremely difficult, with most experiments being conducted in magnetized fluids (*Paret and Tabeling*, 1998). Two systems, however, allow us to observe plasma with high Reynolds numbers directly. The laboratory fusion devices, such as tokamak, are one of them. The second is a natural system – the solar wind. These systems give us an insight into two very different states of the plasma. We now introduce these systems and discuss their properties.

## 1.2 Tokamak plasma

In a tokamak, the plasma is confined by strong magnetic fields. Table 1.1 outlines typical values of physical quantities characteristic of the tokamak plasma. Figure 1.2 shows how the typical configuration of the magnetic field is produced. The toroidal component  $B_\Theta$  is generated by external coils. A smaller, poloidal magnetic field is produced by toroidal currents induced in the plasma. The complete magnetic field



Parameter	Typical Value
Plasma volume	1 – 100m <sup>3</sup>
Ion concentration	10 <sup>19</sup> – 10 <sup>20</sup> m <sup>3</sup>
Temperature	1 – 7keV
Pressure	0.1 – 1atmosphere
Magnetic field	1 – 10Tesla
Total plasma current	0.1 – 5MA

Table 1.1: Typical parameters of tokamak plasmas.

produces an infinite set of nested, toroidal magnetic surfaces. The direction of the magnetic field changes from surface to surface, making it prone to many instabilities. These instabilities are thought to be responsible for the enhanced loss of energy of the confined plasma which is much faster than this predicted by a simple particle collision calculations. This anomalous confinement can result, for example, from  $\mathbf{E} \times \mathbf{B}$  drifts arising from electric field fluctuations. Magnetic instabilities are also present and can modify the structure of the magnetic field. Among them *tearing modes* can produce the rapid transport of energy along the distorted field lines and result in an enhanced radial transport.

It has been well established that the transport in the confinement zone of a tokamak device is dominated by turbulence (*Diamond and Hahm, 1995*). This turbulent transport is triggered by so called marginal instabilities in the plasma. The marginal instability concept simply states that, when the local gradient exceeds the critical value, the flux increases rapidly bringing the local gradient below criticality. The large scale transport events or bursts, consistent with such mechanism, has been observed in both computer simulations (*Garbet and Waltz, 1998; Sarazin and Ghendrih, 1998*) and tokamak experiments (*Rhodes et al., 1999*). Faced with plethora of possible mechanisms for the enhanced transport and energy loss, analytical theory of these phenomena is not well developed. The marginally stable system can, however, be modeled using avalanching models, for example, the sand-pile model described previously. In *Carreras and Newman (1996)* a SOC paradigm for turbulent transport in magnetically confined plasma was proposed to model

plasma transition from low to high confinement state. This high confinement state, or the H-mode, is usually attributed to a transport barrier developing spontaneously within the system. Such barrier causes the local reduction of turbulent transport near the edge of the plasma. The H-mode can be detected by observing the pressure and temperature profiles of the plasma. These exhibit a steep gradient close to the plasma edge. Steady high confinement state is accompanied by edge localized modes (ELMs). These ELMs are periodic rapid energy and particle loss events. In Chapter 5, we will show how the previously described sandpile can be used to model the appearance of such transport barriers in the plasma. Because of the simplicity of this model, it is possible to formally characterize and explain the mechanisms underlying pedestal formation and to identify links to tokamak plasma behavior (*Chapman et al.*, 2001c). In contrast with *Carreras and Newman* (1996), where the transport barriers were created artificially, confinement phenomenology characteristic of the tokamak plasma emerges naturally from the simple sandpile model presented here. We find close analogs for enhanced confinement, edge pedestal and ELMs (*Chapman et al.*, 2001c). The quantitative measures of correlation between stored energy and edge localized mode frequency are in good agreement with available experimental results. The overall picture that emerges from this study suggests that the low confinement mode corresponds to the SOC state of the plasma, while the H-mode or high confinement mode exhibits features characteristic of deterministic chaotic systems such as limit cycles and period doubling.

### 1.3 Solar wind

Statistical properties of the interplanetary magnetic field (IMF) fluctuations are a topic of considerable interest in space research. The subject is closely related to energy transport and acceleration processes in the solar wind (*Tu and Marsch*, 1995; *Burlaga*, 2001). Statistical features of the velocity field fluctuations recorded in the wind tunnels and these obtained from the solar wind observations exhibit striking similarities (*Carbone et al.*, 1995; *Veltri*, 1999). A unifying feature found

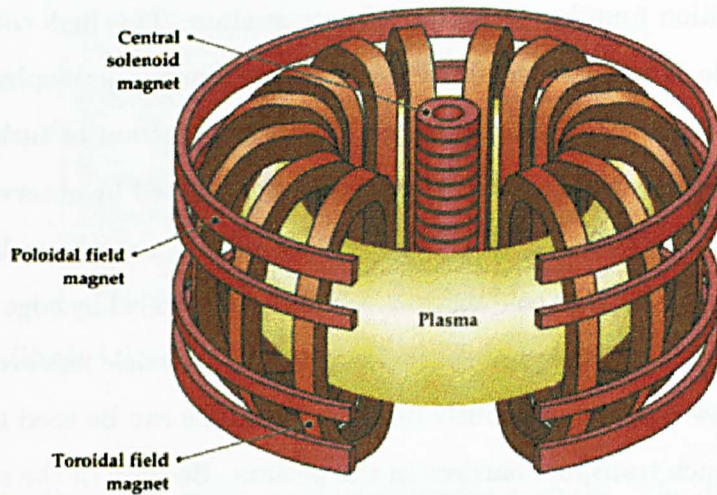


Figure 1.2: Magnetic field generation in tokamak. Image courtesy of Lawrence Livermore National Laboratory.

in these fluctuations is statistical intermittency defined as the presence of large deviations from the average value. Intermittency can be detected and characterized by the Probability Density Function (PDFs) of these fluctuations. The PDFs, unlike the power spectra that do not reveal intermittency, show a clear departure from the Normal distribution on small temporal scales (*Bohr et al.*, 1998; *Frisch*, 1995) while large scale features appear to be uncorrelated and converge toward a Gaussian distribution. These similarities suggest a common origin of the fluctuations in the turbulent fluid and the solar wind. The approach is to treat the solar wind as an active highly nonlinear system with fluctuations arising *in situ* in manner similar to that of hydrodynamic turbulence (*Tu and Marsch*, 1995; *Goldstein and Roberts*, 1999; *Milovanov and Zelenyi*, 1998).

Single point measurements can not uniquely determine the existence of turbulence (*Frisch*, 1995) and ideally, one needs to construct a structure function from a range of spatial locations in the fluid. However, data taken over long intervals in the solar wind is routinely single point and can yield strongly suggestive, if not definitive results, and it is this type of data that we treat in Chapter 6. Data analysis methods applied to investigate solar wind turbulence so far has relied on existing turbulence models. Spectral methods, used in *Goldstein and Roberts* (1999) or *Hor-*

*bury and Schmidt* (1999), are used to examine the scaling of the power spectrum of the Elsässer variables defined as:

$$\mathbf{Z}_{\pm} = \delta \mathbf{v} \pm \frac{\delta \mathbf{b}}{\sqrt{4\pi\rho}}, \quad (1.14)$$

where  $\delta \mathbf{v}$  and  $\delta \mathbf{b}$  are velocity and magnetic field fluctuations around mean. Calculated power spectra show a power law regions with slope near 5/3 as predicted by Kolmogorov's dimensional analysis. The result, however, assumes that the magnetic field fluctuations are dominated by Alfvén waves. Only then, knowing the exact dispersion relation, can one transform the result to  $k$  space for direct comparison with Kolmogorov's theory. Obtaining a clean power spectrum is, however, difficult due to bursty character of the data. Stationarity of the data is often an issue. In recent years, studies of the PDF of both velocity and magnetic field fluctuations experienced a significant development. Following Kolmogorov's 1962 theory (*Kolmogorov*, 1962), where the observed statistical intermittency appeared as a result of the fluctuations in the rate of energy transfer of the turbulent cascade, Castaing proposed an empirical model for the PDF of velocity differences (*Castaing et al.*, 1990). Given that: 1) for a constant energy transfer rate  $\epsilon$ , the fluctuating quantity has a Gaussian distribution and 2) the width of the Gaussian has a log-normal distribution, it was shown that the resultant Castaing distribution gives a good fit to the velocity difference PDFs in laboratory fluid turbulence experiments. In the case of the solar wind, one can obtain a good fit to the PDF of velocity and magnetic field fluctuations by this method (*Sorriso-Valvo et al.*, 1999, 2001) or one can consider the fluctuations about the mean value (*Padhye et al.*, 2001). In Chapter 2, we will discuss a finite size scaling method that can be used not only to study the PDF scaling but also to obtain the analytical functional form of the asymptotic PDF. Our analysis suggests that the magnetic field energy density fluctuations are governed by the mono-scaling process that can be described by a Fokker-Planck equation. In Chapter 6, we will demonstrate how the diffusion coefficient can be calculated directly from our results.

The interaction of the solar wind with the Earth's magnetic field creates a natural plasma confinement system with complex dynamics. This solar wind-magnetosphere-ionosphere system is shown in figure 1.3. The solar wind energy is



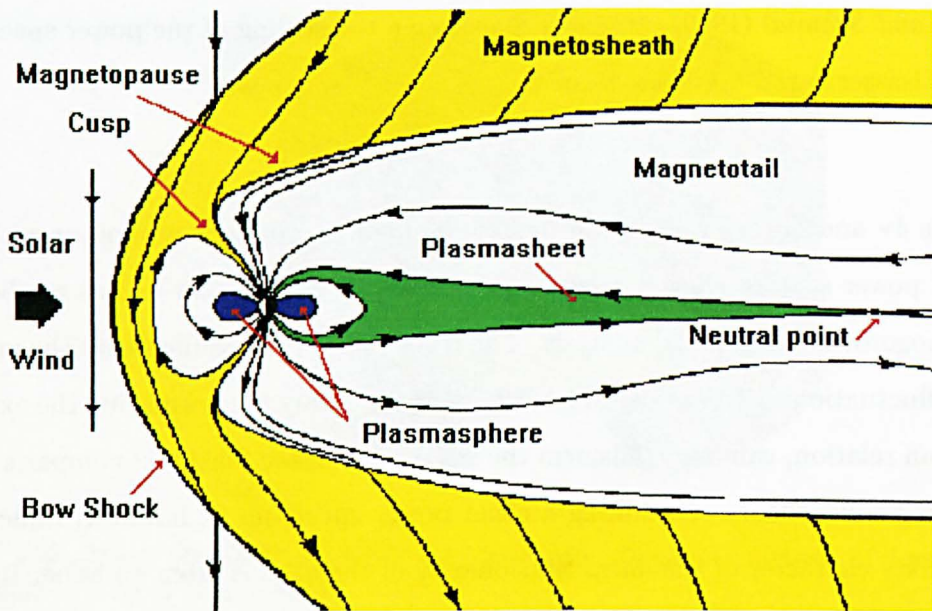


Figure 1.3: The coupled solar wind-magnetosphere-ionosphere system.

constantly transferred into the magnetosphere keeping it out of equilibrium. The energy is then released by a range of mechanisms such as plasma sheet heating or the kinetic energy of a plasmoid ejection. Recently, there has been considerable interest in viewing the coupled solar wind-magnetosphere as a complex system where multi-scale coupling is a fundamental aspect of the dynamics (see (Chang, 1999; Chapman and Watkins, 2001a; Consolini and Chang, 2002) and references therein). Examples of the observational motivation for this approach are bursty transport events in the magnetotail (Angelopoulos *et al.*, 1992) and evidence that the statistics of these events are self-similar (as seen in auroral images (Lui *et al.*, 2000)). Geomagnetic indices are of particular interest in this context as they provide a global measure of magnetospheric output and are evenly sampled over a long time interval. There is a wealth of literature on the magnetosphere as an input-output system (see for example, Klimas *et al.* (1996); Sitnov *et al.* (2000); Tsurutani *et al.* (1990); Vassiliadis *et al.* (2000); Vörös *et al.* (1998)). Recent work has focussed on comparing some aspects of the scaling properties of input parameters such as  $\epsilon$  (Perreault and Akasofu, 1978) and the AE index (Davis and Sugiura, 1966) to establish whether, to the lowest order, they are directly related (Freeman *et al.*, 2000a; Uritsky *et al.*,

2001). Although these studies are directed at understanding the coupled solar wind-magnetosphere in the context of Self-Organized Criticality (SOC), a comprehensive comparison of the scaling properties of the indices and some proxy for the driver ( $\epsilon$ ) also has relevance for the predictability of this magnetospheric “output” from the input. Importantly, both “burstiness” (or intermittency) and self-similarity can arise from several processes including SOC and turbulence. Indeed, SOC models exhibit threshold instabilities, bursty flow events and statistical features consistent with the “scale-free” dynamics such as power law power spectra. It has been proposed by *Chang* (1992, 1999) that magnetospheric dynamics is indeed in the critical state or near it. Alternatively, *Consolini and De Michelis* (1998) used the Castaing distribution – the empirical model derived in *Castaing et al.* (1990) and based on a turbulent energy cascade – to obtain a two parameter functional form for the Probability Density Functions (PDF) of the AE fluctuations on various temporal scales. Turbulent descriptions of magnetospheric measures also model observed statistical intermittency, i.e., the presence of large deviations from the average value on different scales (*Consolini et al.*, 1996; *Vörös et al.*, 1998). An increased probability of finding such large deviations is manifested in the departure of the PDF from Gaussian toward a leptokurtic distribution (*Sornette*, 2000).

In Chapter 6, we will apply a finite size scaling to parameters that quantify the coupling between the solar wind and the magnetosphere. This investigation includes the Akasofu’s  $\epsilon$  parameter as well as AL, AU and AE magnetospheric indices. The Akasofu’s  $\epsilon$  parameter (*Perreault and Akasofu*, 1978), the energy flux entering the magnetosphere, is closely related to the Poynting flux and is defined as:

$$\epsilon = v \frac{B^2}{\mu_0} l_0^2 \sin^4(\Theta/2) \quad \text{where} \quad (1.15)$$

$$l_0 \approx 7R_E \quad \text{and} \quad \Theta = \arctan(|B_y|/B_z). \quad (1.16)$$

The AL and AU indices measure the magnetic activity of the magnetosphere through the range of the ground based magnetometers. We will discuss the results of finite

## Chapter 2

# Models and Methods

Analytical description of a complex system's dynamics is often intractable. In some cases, the allowed number of degrees of freedom is too large and traditional attempts to solve exact dynamical equations fail. The sandpile model used in this work represent a good example of such systems. Although the local rules, from which the overall dynamics arise, are very simple, the strong coupling between different parts of the system, combined with the long range correlation imposed on it, makes it impossible to construct continuous differential equations describing the system's dynamics. In the case of turbulence, the situation is different. Here the equation that, as it is widely believed, describes all possible aspects of the fluid flow is given in the form of the Navier-Stokes equation. It is impossible, however, to obtain all possible solutions of this equation and map them onto all possible experimental flows. The lack of an exact analytical approach, in both cases, forces us to use other methods to characterize the systems and differentiate between the various modes of its behavior. One of the possible approaches is statistical analysis. This chapter is structured in the following way. First, we introduce the sandpile model, used throughout this work, and discuss already published results. Section 2 introduces a Fokker-Planck equation and two finite size scaling techniques, one for spatially localized data, another for spatially extended systems. Phase space reconstruction will be discussed in Section 3. These techniques will be applied to experimental in the following chapters. Finite size scaling and phase space reconstruction will

## Chapter 2

# Models and Methods

Analytical description of a complex system's dynamics is often intractable. In some cases, the allowed number of degrees of freedom is too large and traditional attempts to solve exact dynamical equations fail. The sandpile model used in this work represent a good example of such systems. Although the local rules, from which the overall dynamics arise, are very simple, the strong coupling between different parts of the system, combined with the long range correlation imposed on it, makes it impossible to construct continuous differential equations describing the system's dynamics. In the case of turbulence, the situation is different. Here the equation that, as it is widely believed, describes all possible aspects of the fluid flow is given in the form of the Navier-Stokes equation. It is impossible, however, to obtain all possible solutions of this equation and map them onto all possible experimental flows. The lack of an exact analytical approach, in both cases, forces us to use other methods to characterize the systems and differentiate between the various modes of its behavior. One of the possible approaches is statistical analysis. This chapter is structured in the following way. First, we introduce the sandpile model, used throughout this work, and discuss already published results. Section 2 introduces a Fokker-Planck equation and two finite size scaling techniques, one for spatially localized data, another for spatially extended systems. Phase space reconstruction will be discussed in Section 3. These techniques will be applied to experimental in the following chapters. Finite size scaling and phase space reconstruction will



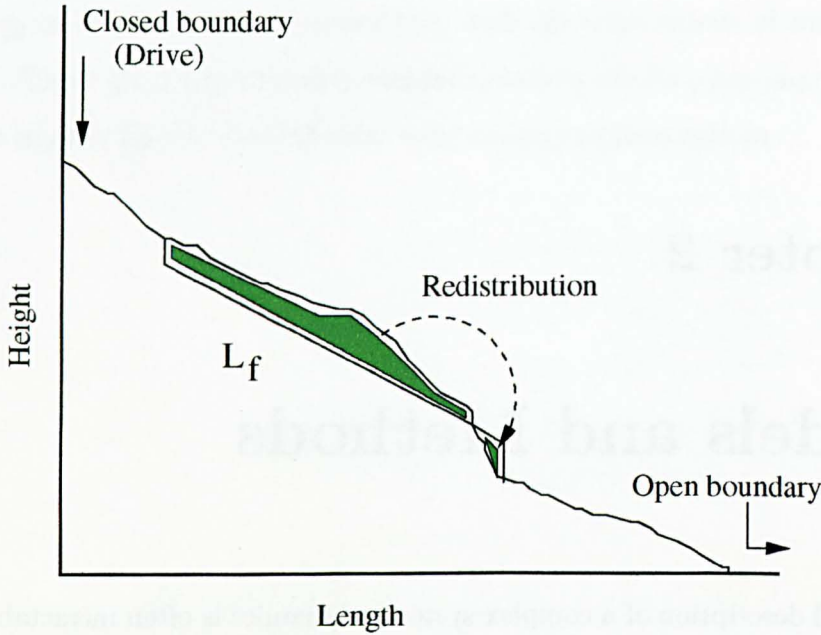


Figure 2.1: Schematic of the sandpile algorithm described in this section.

be used in Chapter 4 to obtain new results for the sandpile model. In Chapter 6, a finite size scaling method will be used for our studies of the solar wind and its interaction with the Earth's magnetosphere.

## 2.1 Our sandpile model

The sandpile algorithm (*Chapman et al.*, 1999; *Tam et al.*, 1999; *Chapman*, 2000) investigated here is defined on a one-dimensional grid of  $N$  equally spaced cells as shown on the figure 2.1. The real variable  $h_i$ , representing the height of the sand, is assigned at each node. The local gradient at cell  $i$  is given by  $g_i = h_i - h_{i+1}$ . Stability of the model at any given time is determined by the value of the local gradient  $g_i$ . All points with the value of  $g_i$  smaller than some assigned threshold  $g_c$  are stable. If, however, the value of  $g_i$  at some point  $i$  is larger than the threshold the sand will be redistributed down the pile. The system is driven by adding sand to cell 1 at a constant rate  $g$ . The inflow rate of the sand is slow compared to the time between avalanches, i.e.,  $g_c/g \gg 1$  and the dynamics of the system has been found to be insensitive to the choice of  $g$  as long as this condition holds. Assuming

that the critical gradient is exceeded in node  $i$  our redistribution rules are given by following equations:

$$h_{i-k,i-k+1,\dots,i}^* = h_{i-k,i-k+1,\dots,i} - \Delta \quad (2.1)$$

$$h_{i+1}^* = h_{i+1} + k \times \Delta. \quad (2.2)$$

Where  $*$  indicates intermediate steps in the relaxation,  $\Delta$  is equal to  $g_i/(k+1)$ , index  $k = \min(i, L_f)$  and  $L_f$  is the tuning parameter that can assume values between 1 and the length of the lattice  $N$ . The value of the parameter  $L_f$  is fixed for every run of the simulation. The boundary conditions are such that the system is closed at node 1 and open at node  $N$ . If the avalanche of the tumbling sand reaches the open boundary the sand simply exits the system. The parameter  $L_f$  is a major, new feature of this algorithm. By modifying the value of  $L_f$ , one can change the number of interacting sites within the model. In the case of  $L_f = N$ , the instantaneous propagation of information across the entire avalanche gives rise to a scale free dynamics of the system and the existence of the nontrivial fixed point (*Tam et al.*, 1999).

Since the avalanches propagate instantaneously, there is no sand added during the transport process. The minimum time increment is then taken as time elapsed between two consecutive avalanches. We define the energy of the sandpile at any given time  $t$  as its potential energy

$$E(t) = \left( \sum_{i=1}^N h_i^2 \right)_t. \quad (2.3)$$

The energy dissipated during one event is simply the difference of this potential energy of the sandpile immediately before and after the event:

$$dE(t) = E_t^{bef} - E_t^{aft}. \quad (2.4)$$

These two quantities,  $E(t)$  and  $dE(t)$  represent a phase space in which dynamics of our sandpile can be represented (see Figure 2.2). We will use this approach in the next section when presenting different dynamical regimes of the system. The

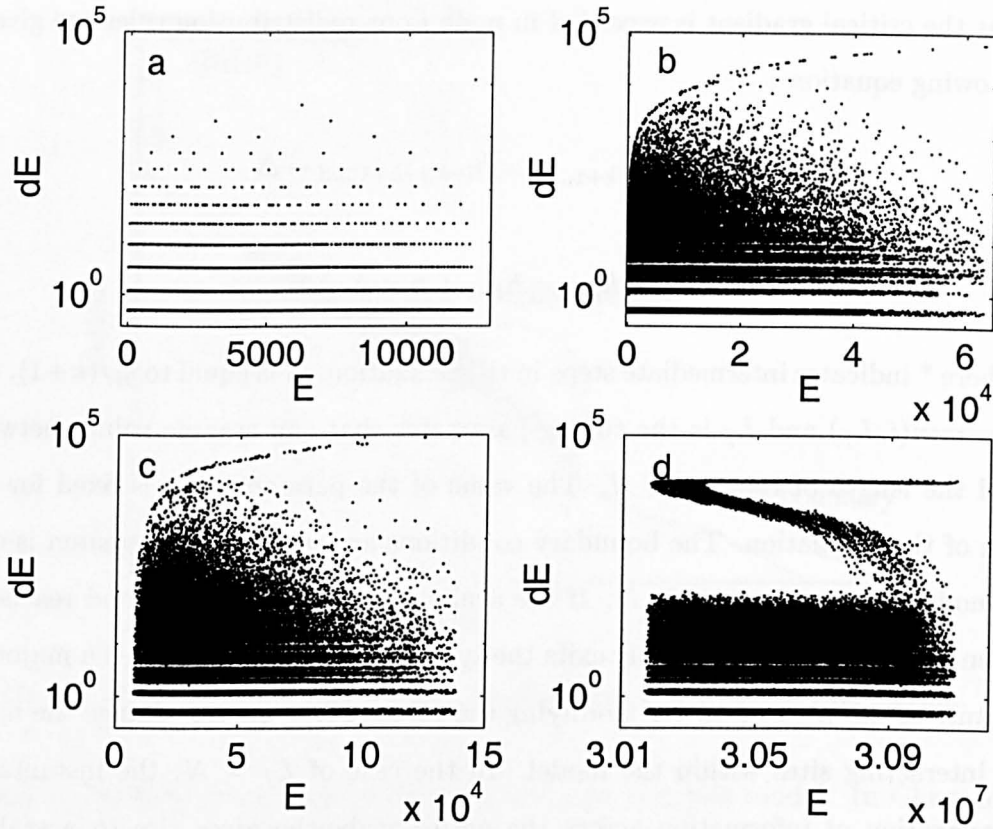


Figure 2.2: Phase space plots of the sandpile stationary state constructed by plotting  $dE$  as defined in (2.4) versus total energy  $E$  of the system. System Length  $N = 4096$ ; (a)  $L_f = N$  and no randomization, (b)  $L_f = N$  and 2% randomization, (c)  $L_f = 2000$  and 2% randomization, (d)  $L_f = 50$  and 2% randomization.

control parameter  $L_f$  is not the only one relevant to the dynamics of the model. Since the value of the critical gradient  $g_c$  is assigned to every node of the grid one can investigate if the system performs differently under different assignment schemes. There are two cases leading to distinct dynamics:

1. The parameter  $g_c$  is constant.
2. The parameter  $g_c$  is a random variable with a given (here, a top-hat) probability distribution.

The first scenario is tractable analytically and was used in an analytical calculation of the fractal dimension for the energy curve. We will present this result in Chapter 4. The second case is more appropriate for modeling the real physical systems where

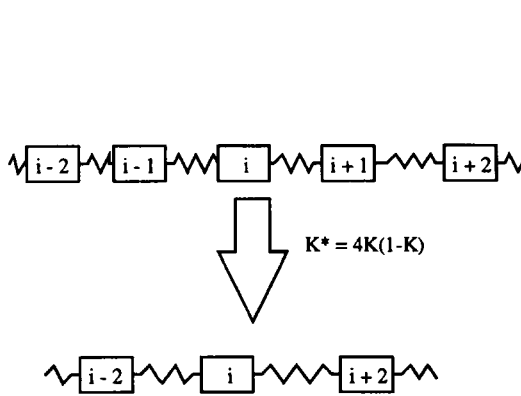


Figure 2.3: Reducing the complexity of the dynamical system via Renormalization procedure.

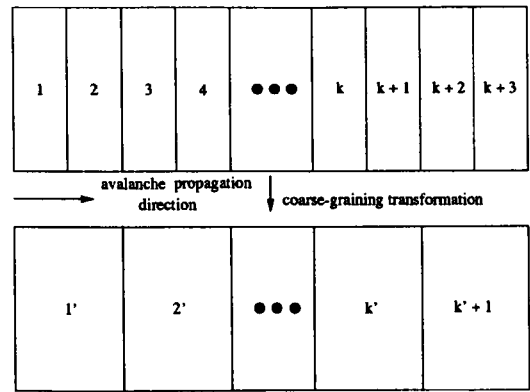


Figure 2.4: Coarse-graining procedure for the one-dimensional directional sandpile model.

the driving rate is nonuniform and the fluctuating critical gradient represent possible values of the threshold for various instabilities within the system.

### 2.1.1 Renormalization Group

The sandpile model presented here was previously studied using Renormalization Group (RG). We will briefly described the use of RG method for critical systems before we discuss the dynamics of the model. Consider the behaviour of the macroscopic magnetization of the material undergoing a transition of the ferromagnetic type. The spins of individual atoms are uncorrelated and no magnetization can be detected in the material for high temperatures. When the temperature decreases, some correlation of spins appear and isolated islands of magnetization can be detected. These ordered regions persist for a certain length of time and one can attempt to characterize this phase by introducing a correlation time  $\tau$  and a correlation length  $\xi$ . For the critical temperature  $T_c$ , this correlation length become infinite and the entire material, no matter how large in size, becomes spontaneously magnetized. Such divergence of the correlation length at the critical point makes the analytical studies of critical systems difficult. Indeed, the most widely used approximation methods neglect the correlation between large number of particles and work only for small correlation lengths. In plasma physics, for example, which is not critical but where the long correlation length is imposed by the electrostatic

forces, many problems are approximated by considering only two particle interaction (*Clemmow and Dougherty, 1990*).

RG methods allow us to establish a correspondence between a system with a given correlation length and another where the correlation length is smaller by a certain factor. At the critical point, the system should be invariant under dilation, while in the vicinity of it there is a certain mean correlation length that destroys this invariance. In that sense, the RG is an essential and central tool for critical system analysis as it is simplified when the correlation length tends to infinity. We will now use a simple dynamical model to illustrate how RG analysis can be applied to study a many-body system. Let us consider a large number of blocks, each with mass  $m$ , connected with identical springs with Hook's constant  $k$  as illustrated in figure 2.3. If  $x_i$  represents the displacement of the  $i$ -th block, the equation of motion can be written as:

$$m \frac{d^2 x_i}{dt^2} = k(x_{i+1} - x_i) - k(x_i - x_{i-1}). \quad (2.5)$$

We then propose the solutions of (2.5) to be in the form  $x_i = a_i e^{i\omega t}$ , where  $a_i$  is independent of time. Equation (2.5) can now be reduced to

$$-4Ka_i = a_{i+1} + a_{i-1} - 2a_i, \quad \text{where} \quad K = \frac{m\omega}{4k}. \quad (2.6)$$

Similar equations can be written for  $a_{i-1}$  and  $a_{i+1}$  and solved for these quantities. Results, now expressed in terms of  $a_{i-2}$  and  $a_{i+2}$ , can be substituted into (2.6) which then takes form of:

$$-16K(1 - K)a_i = a_{i+2} + a_{i-2} - 2a_i. \quad (2.7)$$

We now note that equation (2.7) is identical in form to (2.6) if one defines a renormalized coefficient  $K^*$ ,

$$K^* = 4K(1 - K). \quad (2.8)$$

Thus we have eliminated all odd blocks in the chain, reducing the complexity of the problem. We have done it by redefining the quantity  $K$  and doubling all distances

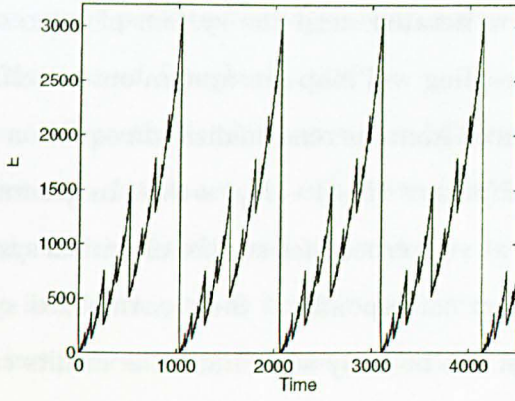
between blocks. This procedure can be iterated until the system of interest can no longer be reduced, i.e., each next rescaling will map our system onto itself. The existence of such *fixed point* can be deduced from the renormalization equation (2.8). One looks for such values of  $K_f$  that,  $F(K_f) \equiv 4K_f(1 - K_f) = K_f$ . In general, the existence of a fixed point is not trivial but very crucial for studies of critical systems. In our simplified example, the fixed point corresponds to the renormalized system with only one block left. Such equation can be easily solved and the results can be related to the original system by transforming back parameters of the system. In summary, the objective of the renormalization group approach is not to solve the equations of motion but to reduce original equations by means of the renormalization transformation similar to (2.8).

In the case of the directional and one dimensional sandpile models, the renormalization procedure is often discussed in terms of the scaling found in the avalanche length distribution. We consider an ongoing avalanche propagating in the sandpile system and define a conditional probabilities  $Q_k$  that a given avalanche stops at cell  $k$  (Tam *et al.*, 1999). The coarse graining procedure, illustrated in figure 2.4, is equivalent to doubling the size of the system at each iteration. It was then shown in Tam *et al.* (1999) that the renormalization transformation of the probability  $Q$  is given by:

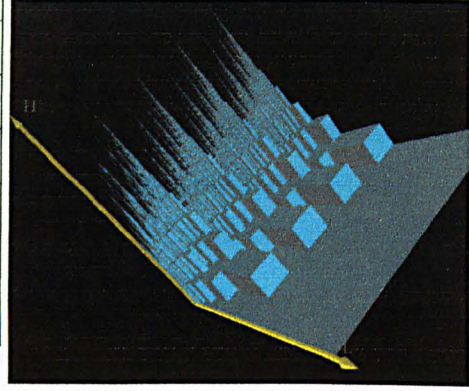
$$R(Q) = 2Q - Q^2. \quad (2.9)$$

Similarly to the RG analysis of Vespignanni *et al.* (1995), no site-site correlation was assumed here. The probability that, after reaching site  $k$ , the avalanche will continue to site  $k + 1$  is given by product  $(1 - Q_k)(1 - Q_{k+1})$ . The RG analysis confirmed the existence of a fixed point for the system with parameter  $L_f = N$  and the randomization of the critical gradient. The previously reported power law index of  $-1$  for the avalanche and dissipated energy probability distributions was also found to be valid for the large scale events.

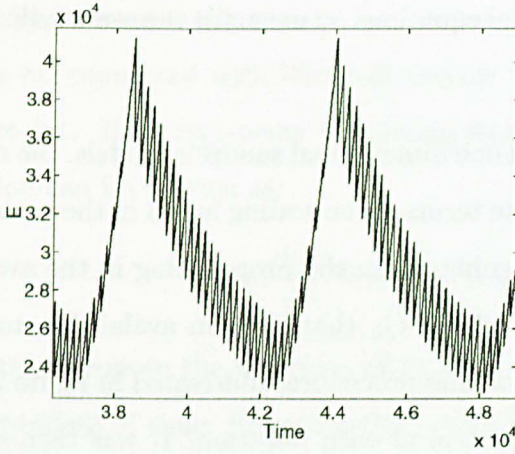




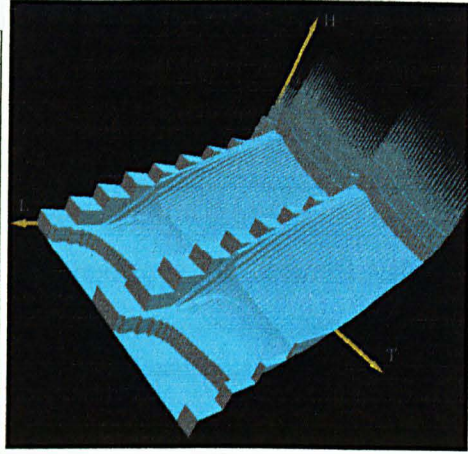
(a) : Total Energy vs. Time



(b): 3D height profile evolution



(c) : Total Energy vs. Time



(d): 3D height profile evolution

Figure 2.5: System dynamics for system length  $N = 1024$  with  $L_f = N$  (a,b) and  $L_f = 200$  (c,d). Critical gradient is constant.

### 2.1.2 System Dynamics

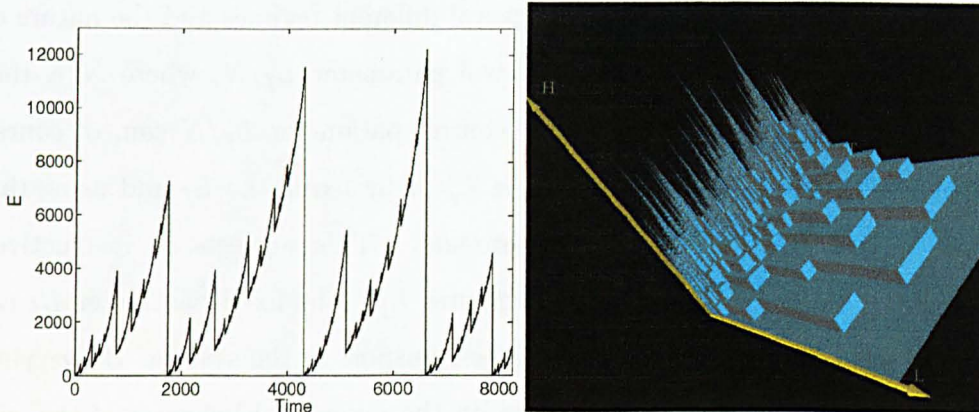
The behavior of the system has been described in some detail in *Chapman et al. (1999)*; *Tam et al. (1999)*; *Chapman (2000)*. Here, we will summarize these results and present some additional interpretations. New results, obtained using a finite size scaling and a nonlinear time series analysis, will be discussed in Chapter 4. These results will address a question of quantifying the proximity of the system to its fixed point through time series analysis.

To study the system, we let it evolve until the energy time series reaches a stationary state indicated by a constant value of the mean i.e.,  $\langle E(t) \rangle = \text{const.}$

The behavior of the system exhibits several different regimes and the nature of the regime is solely dependent on the control parameter  $L_f/N$ , where  $N$  is the size of the sandpile. A given value of the control parameter  $L_f/N$  can, of course, be achieved either by fixing  $N$  and varying  $L_f$  or by fixing the  $L_f$  and using the size of the system,  $N$ , as the dynamic parameter. This suggests an instructive way of considering the role the control parameter  $L_f$ . The fixed parameter  $L_f$  can be treated as the scale size of the anomalous transport in the system. By varying the size of the system  $N$ , one can then obtain the dynamical behavior of the system. This implies that a finite size system with an anomalous transport scale ( $L_f$ ) and dynamic boundaries (corresponding to different values of  $N$  in the model) or a variable anomalous transport scale and fixed boundaries can explore a large portion of its dynamical range and is unlikely to remain at the  $L_f = N$  fixed point (at criticality). For astrophysical observation and most laboratory plasma systems, the driving rate is not slow and can be non-uniform. Importantly, the statistics of the large scale events in the model are unaffected by increased fluctuations in the driving rate ( $g_c/g$ ) (*Chapman et al.*, 1999; *Watkins et al.*, 1999) and, as we will discuss, dynamics of these events is controlled by a nontrivial fixed point ( $L_f = N$ ).

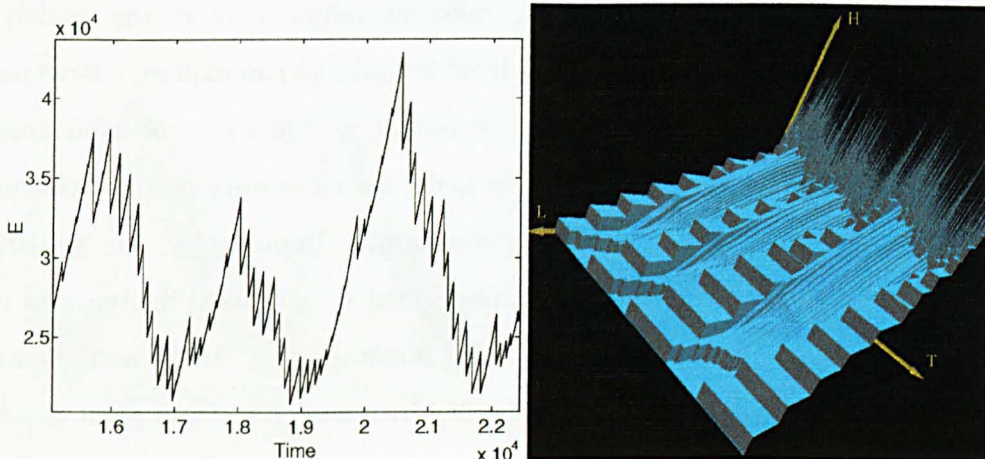
We start the discussion of the system's dynamics with the case when the critical gradient  $g_c$  is constant. For  $L_f = 1$  the model is essentially the original BTW sandpile in one dimension (*Bak et al.*, 1987). The dynamics of this system is dominated by the attractive fixed point in the parameter space. A state where all nodes of the sandpile are marginally below a critical gradient is a strong attractor of its dynamics. Once this state is reached all perturbations, such as an added grain of sand, are immediately suppressed via system-wide avalanche and the system returns to the marginally stable configuration. This state of the system can be represented by a single point in the phase space given by the total energy  $E(t)$  of the system and the change of the energy  $dE(t)$ . Another limiting case is when  $L_f = N$ . A number of results have been obtained in this regime. For the constant critical gradient  $g_c$ , the evolution of the sandpile can be obtained analytically (*Helander et al.*, 1999).





(a) : Total Energy vs. Time

(b): 3D height profile evolution



(c) : Total Energy vs. Time

(d): 3D height profile evolution

Figure 2.6: System dynamics for system length  $N = 1024$  with  $L_f = N$  (a,b) and  $L_f = 200$  (c,d). 2% fluctuations of the critical gradient are added.

Probability distributions of the avalanche lengths and energy dissipated show power law behavior with index equal to  $-1$ . The phase space plot, shown on 2.2(a), is a set of the line segments spaced  $2^\ell$  units apart ( $\ell$  is integer). The behavior of the system is strongly influenced by the closed boundary in this regime. The three-dimensional surface in 2.5(b) shows that the edge of the sandpile never remains in the immediate vicinity of the open boundary. As soon as the avalanche reaches the end of the system, the edge is pushed back. The length of the horizontal step-like features in the height profile appears at values given by  $2^\ell$  ( $\ell$  integer). In such configuration, the majority of the energy stored in the system is located near the closed boundary of the sandpile. As long as the dynamic parameter is of the order of the system's

length  $N$ , the dynamics of the system is reminiscent of that for  $L_f = N$ . The probability distributions of the avalanche length and energy dissipated show similar scaling as before (see Fig. 12-15 in *Chapman* (2000)). The most interesting region of the systems behaviour can be observed for  $2 < L_f < N/4$ . The signal is now oscillating (see 2.5(c)) and has a period doubling sequence (*Chapman*, 2000). A clear case of the scale separation emerges from the phase space plots. The small scale behaviour (avalanche length  $< L_f$ ) is identical to that of the system with  $L_f = N$  and emerges as the set of linear segments. On the large scale, we have a low-dimensional nontrivial structure representing a limit cycle of the oscillatory dynamics (see figure 7 in *Chapman* (2000)). Figure 2.5(d) shows that the dynamics of the system is influenced much more by the open boundary rather than the closed one. Avalanche statistics show the increase in the probability of system wide events in this regime. These long avalanches push the edge of the sandpile up to the open boundary. The edge is then slowly retracted and this backward movement of the edge creates horizontal steps of approximately equal length.

We now discuss the case when statistical fluctuations are added to the value of the critical gradient. We use a "top hat" probability distribution  $P(g_c)$  for values of the random numbers assign to the local critical gradient i.e.,  $P(g_c)$  is nonzero and constant in range  $[a, b]$  and zero elsewhere. It can be shown that, for  $L_f = N$ , the system has a repulsive fixed point and the avalanche length probability distribution varies as  $l^{-1}$  for large scale events (*Tam et al.*, 1999). For small avalanches dissipated energy exhibits different scaling (*Chapman et al.*, 1999) which extends to about 128 in avalanche length units for the system size of 4096. The fact that there are two fixed points and the evidence that the repulsive fixed point only governs the dynamics of the large scale events makes the small events scaling relevant for the further investigation. When the fluctuation of the critical gradient reaches 2%, the phase space plot, shown on 2.2(b), changes very profoundly. The scale separation appears and linear segments, although still present in the small  $dE$  region, are replaced by a parabolic curve for the large events. For values of the parameter  $L_f$  between  $N/4$  and  $N$ , the dynamics of the system is now irregular. Figure 2.6(a,b) shows the time

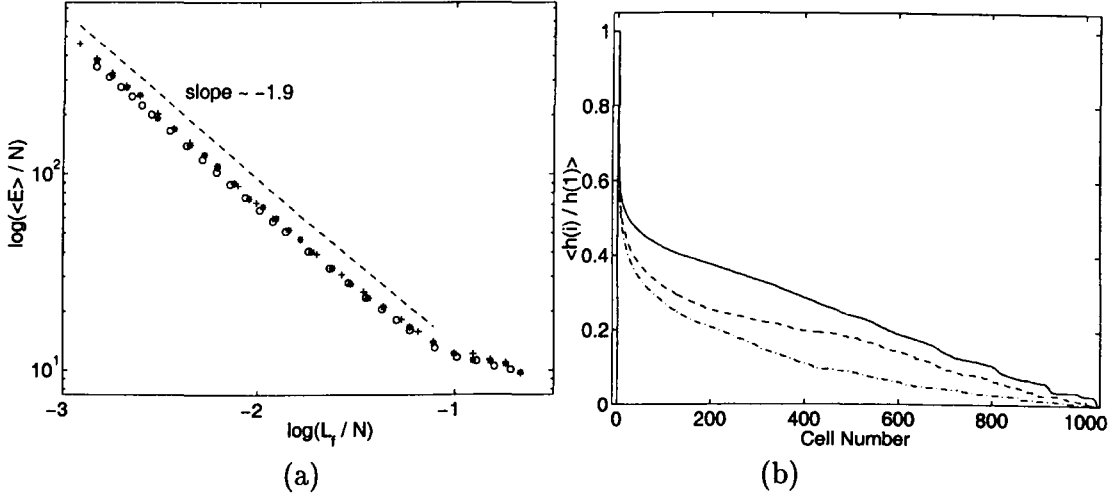


Figure 2.7: (a): Mean normalized energy stored in the system as a function of the control parameter for three different system sizes: ( $\circ$ )  $\equiv 512$ , ( $\star$ )  $\equiv 4096$  and ( $+$ )  $\equiv 8192$ . The region of slope -1.9 corresponds to  $L_f/N < 1/4$ . (b): Mean height profile for the system length  $N = 1024$  and  $L_f$  parameter equal to 800 (solid line), 550 (dashed line) and 200 (dash-dot line).

evolution of the system for the same values of input parameters as used on 2.6(a,b) but with 2% critical gradient fluctuations.

Similar to the case of constant critical gradient, the transition in behaviour occurs approximately for  $L_f \approx N/4$ . Interestingly, figure 2.7(a) shows that the system's energy scales with its finite size  $N$  for small and large values of the control parameter  $L_f/N$  and the break in scaling appears at  $L_f/N \approx 1/4$ . The region of dynamics given by  $1 \leq L_f \leq N/4$  is weakly sensitive to the added fluctuations and all of the features of the time series observed for constant critical gradient are preserved (Chapman, 2000). For  $L_f/N \leq 1/4$  horizontal steps of approximately equal size appear in the height profile. This linear (rather than as  $2^\ell$ ) dependence of the length of the step on its position on the grid leads to the increase of the total energy stored in the system (see figure 2.7(b)), when compared with the  $1/4 < L_f \leq N$  dynamics. Increased level of fluctuations does not change the appearance of the phase space attractor shown in figure 2.2(d). This apparent low dimensionality of the model's dynamics, with or without randomization, is its essential feature. Figure 2.6(c,d) shows the time series and 3-D height profile for the same values of input parameters as used in figure 2.5(c,d) but with 2% critical gradient fluctuations. The

periodicity of the signal is preserved on the large scale in this case and the amplitude does not differ from that with constant critical gradient.

## 2.2 Fokker-Planck equation

The Fokker-Planck equation (FPE) provides an important link between statistical studies and the dynamical approach expressed by the Langevin equation (*Sornette, 2000; Schertzer et al., 1995*):

$$Y(t + dt) - Y(t) \equiv m(Y(t), t)dt + \sigma(Y(t), t)dS \quad (2.10)$$

where  $m$  is a deterministic term and  $dS$  represent a stochastic driving source. To derive the FPE for the system described by (2.10), we need to start with definitions of some quantities and concepts of probability theory.

### 2.2.1 Stochastic Markov process and Fokker-Planck Equation

The fundamental quantity of the stochastic analysis is a random variable. A random variable  $Y$  is a function that ascribes a numerical value to any point  $\omega$  drawn from the sample space  $\Omega$ , in mathematical terms,  $\omega \rightarrow Y(\omega)$ . We can, then, consider a mapping  $x \rightarrow P_Y(x)$ , where the function  $P_Y(x)$  is defined on the real axis from  $-\infty$  to  $\infty$ , and insist it has following properties (*Haken, 1978*):

1.  $\forall x : P_Y(x) \geq 0$
2.  $\int_{-\infty}^{\infty} P_Y(x)dx = 1$

If the function  $P_Y(x)$  operates on the domain of the random variables  $Y(\omega)$  then  $P_Y(x)$  is called a probability density function (PDF) and the probability that a sampling of the random variable  $Y$  gives values between  $x$  and  $x + dx$  is given by:

$$p(x \leq x \leq x + dx) = \int_x^{x+dx} P(x)dx \quad (2.11)$$

where the continuous limit has been applied to the density function  $P(x)$ . We can now define a stochastic process  $Y(t)$  as a random variable such that its probability

density function depends on time. A Markov stochastic process is a process where the variable  $Y(t + dt)$  depends only on the previous step, i.e.,  $Y(t)$ ,  $t$  and  $dt$ :

$$Y(t + dt) - Y(t) = \mathcal{M} \quad (2.12)$$

where  $\mathcal{M}$  is drawn from the set of independent and identically distributed (iid) samples. Let us consider  $n - 1$  steps of Markovian process  $y_1, y_2, \dots, y_{n-1}$ . Due to the lack of memory in the process, the probability that in the next step the random variable  $Y(t) = y_n$  is given by the conditional probability density

$$P(y_n, t_n | y_{n-1}, t_{n-1}; \dots; x_1, t_1) = P(y_n, t_n | y_{n-1}, t_{n-1}) \quad (2.13)$$

where  $t_n > \dots > t_1$ . The density  $P(y_n, t_n | y_{n-1}, t_{n-1})$  is often called transition probability. The transition probability allows us to calculate the PDF of the Markov random variable  $\mathcal{M}$  at the time  $t + dt$ :

$$P(y, t + \tau) = \int_{-\infty}^{\infty} P(y, t + \tau | y', t) P(y', t) dy' \quad (2.14)$$

Assuming a one dimensional process where  $y - y' = \ell$  and writing  $P(y, t + \tau | y', t) = P_{\mathcal{M}}(\ell)$  we obtain:

$$P(y, t + \tau) = \int_{-\infty}^{\infty} P_{\mathcal{M}}(\ell) P(y - \ell, t) d\ell \quad (2.15)$$

We will now expand both  $P(y, t + \tau)$  and  $P(y - \ell, t)$  in a Taylor series around  $\tau$  and  $\ell$  respectively.

$$P(y, t + \tau) = P(y, t) + \tau \frac{\partial P}{\partial t} + \mathcal{O}(\tau^2) \quad (2.16)$$

$$P(y - \ell, t) = P(y, t) + \ell \frac{\partial P}{\partial y} + \frac{\ell^2}{2} \frac{\partial^2 P}{\partial y^2} + \mathcal{O}(\ell^3) \quad (2.17)$$

For the  $\delta$ -correlated Markov process, the mean value  $\langle \ell^2 \rangle \propto \tau$  when  $\tau \rightarrow 0$  and thus one needs to keep the quadratic term in (2.17) as it is linear in time. Substituting both (2.16) and (2.17) into (2.15) we get:

$$P(y, t) + \tau \frac{\partial P(y, t)}{\partial t} = \int_{-\infty}^{\infty} P_{\mathcal{M}}(\ell) d\ell \left[ P(y, t) + \ell \frac{\partial P(y, t)}{\partial y} + \frac{\ell^2}{2} \frac{\partial^2 P(y, t)}{\partial y^2} \right] \quad (2.18)$$

We note that all the terms involved in  $P(y, t)$  on the right hand side (rhs) do not depend on  $\ell$  and so the integrals are simply the moments of the PDF  $P_{\mathcal{M}}$ . Writing the moments as:

$$\int_{-\infty}^{\infty} P_{\mathcal{M}} d\ell = 1, \quad (2.19)$$

$$\int_{-\infty}^{\infty} \ell P_{\mathcal{M}} d\ell = \langle \ell \rangle, \quad (2.20)$$

$$\int_{-\infty}^{\infty} \ell^2 P_{\mathcal{M}} d\ell = \langle \ell^2 \rangle, \quad (2.21)$$

we obtain the linear Fokker-Planck equation:

$$\frac{\partial P(y, t)}{\partial t} = \gamma \frac{\partial P(y, t)}{\partial y} + D \frac{\partial^2 P(y, t)}{\partial y^2}, \quad (2.22)$$

where  $\gamma = \frac{\langle \ell \rangle}{\tau}$  and  $D = \frac{\langle \ell^2 \rangle}{2\tau}$ . The coefficient  $D$  is called the diffusion coefficient. Coefficient  $D$  obtained by means of the FPE should be identical to that calculated from the normal diffusion of the physical quantity in space. Equation (2.22) was obtained under the assumption that the mean  $\langle \ell^2 \rangle \propto \tau$ . In many systems, however, this relation is not found and instead we have  $\langle \ell^2 \rangle \propto \tau^\alpha$ . Such processes are referred to as anomalous diffusion. They can be modeled either by allowing functional dependence of the diffusion coefficient on the spatial coordinate,  $D \equiv D(y)$  or by introducing a fractional derivatives in the FPE (*Schertzer et al.*, 1995). In terms of the FPE, this result can be obtained by allowing moments given by (2.19)-(2.21) to vary with spatial coordinate  $y$ . The result is a FPE that can be written as:

$$\frac{\partial P(y, t)}{\partial t} = \frac{\partial}{\partial y} D(y) \frac{\partial P(y, t)}{\partial y}, \quad (2.23)$$

where  $P(y, t)$  is normalized so that  $\int P(y, t) = 1$ . Equation (2.23) describes the dynamic evolution of the probability density function  $P(y, t)$  in terms of a diffusion process in space  $y$  characterized by the diffusion coefficient  $D(y)$ . We note that the F-P approach is also valid for non Markov processes, provided the time scale of interest exceeds the correlation time of the individual steps.

### 2.2.2 Finite size scaling for turbulent systems.

The Fokker-Planck equation (2.23) is a second order parabolic partial differential equation and as such is very difficult to solve. Both initial conditions and boundary conditions must be known to obtain its exact solution. A considerable insight into physical processes of interest can be gained, without knowing the exact solution, by studying a generic class of self-similar functions satisfying the FPE. As was already mentioned earlier, statistical self-similarity emerges as a simplifying aspect for both SOC and turbulence. The simplest process exhibiting statistical self-similarity is a diffusion process often modeled by a purely self-similar Brownian walk. A Brownian walk is obtained by summing independent identically distributed (iid) samples drawn from a zero-centered Gaussian distribution. A typical time series of a Brownian walk is shown in figure 2.8(a). The dynamics of the PDF in such case is given by the linear FPE (2.22). It can be shown (*Tikhanov and Samarskii*, 1988) that the solutions of (2.22) are invariant under the change of variables:

$$y \rightarrow \frac{y}{\sqrt{t}}. \quad (2.24)$$

In other words, if  $P(y, t)$  represents a solution of (2.22) then the rescaled function  $P(y/\sqrt{t}, t)$  also satisfies equation (2.22). The function that satisfies such rescaling is the well known Gaussian curve.

We will now illustrate how the existence of such self-similar solution can be deduced from the time series  $Y(t)$  of the Brownian walk. The analysis is applied to the PDFs of the individual events (increments) and thus, in the case of the Brownian walk, one first needs to difference the original time series. This is done for several different temporal scales  $\tau$ . After the differencing, we obtain several time series:

$$\delta Y(t, \tau) = Y(t) - Y(t + \tau). \quad (2.25)$$

The PDF  $P(\delta Y, \tau)$  is then calculated for each time series  $\delta Y(t, \tau)$  which, in the case of a Brownian walk, is a Gaussian (see figure 2.8(b)). Statistical self-similarity, if present, guarantees that the statistical features of the observed process should not change under dilation of the time interval, i.e., the PDFs  $P(\delta Y, \tau)$ , obtained for the

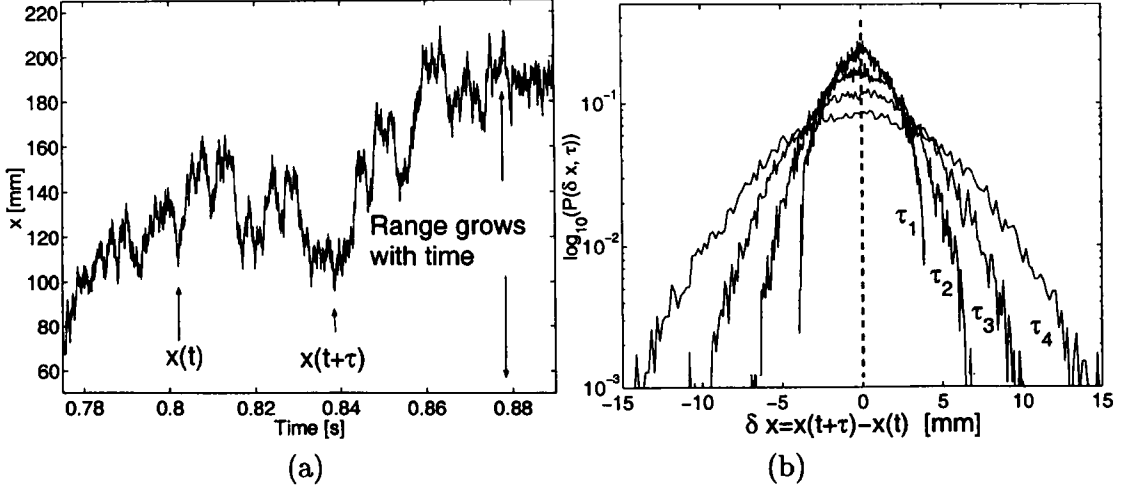


Figure 2.8: Brownian walk time series (a) and corresponding PDFs of the increments for different values of the time lag  $\tau$  (b).

different time dilated intervals, should be equivalent. To test this conjecture, we will compute the standard deviation  $\sigma$ , as a function of the dilated time interval  $\tau$  and assume the most general change of variables:

$$y \rightarrow y/\sigma(\tau) \quad \text{and} \quad P \rightarrow P\sigma(\tau), \quad (2.26)$$

where the rescaling  $P \rightarrow P\sigma(\tau)$  assures that the area under the curve is kept unchanged as required by the definition of the probability. If the underlying process is indeed statistically self-similar all PDFs, corresponding to different time dilated intervals  $\tau$ , should be identical after transformation (2.26) is applied. Figure 2.9(b) shows the collapse of the Gaussian PDFs obtained for the increments of the Brownian walk and after the rescaling is performed. The nearly perfect collapse achieved in this case is merely a representation of the Gaussian law stating that a sum of  $N$  Gaussians with variance  $\sigma^2$  is still a Gaussian with variance  $N\sigma^2$  (Sornette, 2000). One immediately notices that the slope of the fitted line in figure 2.9(b) is  $1/2$  and so  $\sigma(\tau) \propto \sqrt{\tau}$ . This reduces our general rescaling of argument in (2.26) into that found in (2.24), as it should for the Gaussian PDFs.

The goal now is to generalize the above-described rescaling procedure to study time series obtained from turbulent systems where the departure of the PDFs from the Gaussian function is well documented for small values of  $\tau$ . The following



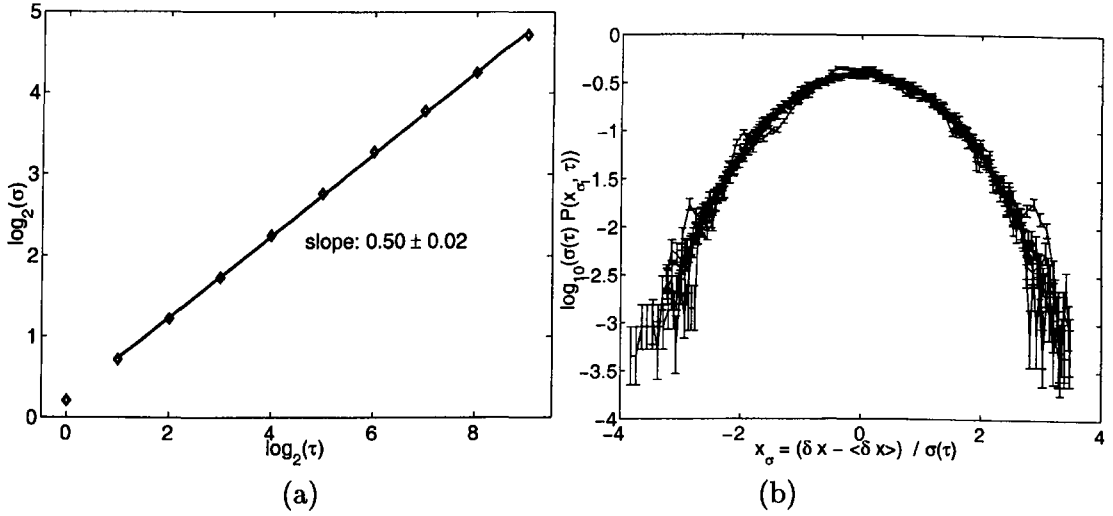


Figure 2.9: Standard deviation scaling as a function of time lag  $\tau$  (a) and the PDFs rescaled according to (2.26) (b) for a Brownian walk time series.

rescaling procedure is based on that introduced in *Mantegna and Stanley* (1995, 2000). To the best of our knowledge, this method was never used to study turbulent systems before. We also extend the analysis to connect the results obtained from the rescaling procedure to the Fokker-Planck approach. We are now looking for the self-similar solutions of the nonlinear FPE (2.23) and these should exhibit the following scaling:

$$P(\delta Y, \tau) = \tau^{-\alpha} P_s(\delta Y \tau^{-\alpha}), \quad (2.27)$$

where  $P_s(\delta Y \tau^{-\alpha})$  is a self-replicating “master” PDF obtained by rescaling  $P(\delta Y, \tau)$  with different temporal dilation factors  $\tau^{-\alpha}$ . Here, rescaling index  $\alpha$  ( $\alpha = 1/2$  for the Brownian walk) is unknown *a priori* and has to be determined from the observed time series. We use the peaks of the PDFs to obtain the scaling exponent  $\alpha$ . This is important as the peaks are the most accurate parts of the distributions. Figure 2.10(a) shows the peaks  $P(0, \tau)$  of the unscaled Gaussian PDFs plotted versus  $\tau$  on log-log axes. We see that there is a range of  $\tau$  for which  $P(0, \tau)$  is well described by a power law  $\tau^{-\alpha}$ . Within this range, we attempt to collapse the entire unscaled PDF shown in figure 2.8(b) onto a single master curve (2.27). A single parameter rescaling, given by equation (2.27), for a mono-fractal process, should give a perfect collapse of the PDFs on all scales. Indeed, figure 2.10(b) shows the expected result.

The successful single parameter rescaling of the PDFs can reveal some key features of the processes governing the fluctuations of the investigated quantity. In particular, one can quantify an asymptotic behavior of the rescaled PDFs. The index given by  $1/\alpha$  characterizes the common functional form of the distributions  $P(\delta Y)$  viz:

- $0 < 1/\alpha < 2$  Lévy (power-law with  $\sigma \rightarrow \infty$ )
- $1/\alpha = 2$  Gaussian (finite  $\sigma$ )
- $1/\alpha > 2$  power-law with finite  $\sigma$

where the distribution is given by:

$$P(\delta Y) \sim \|\delta Y\|^{-(1+1/\alpha)} \quad \text{for } \delta Y \rightarrow \pm\infty \quad (2.28)$$

The rescaling allows us to conclude that the fluctuations are described by the same law on different temporal scales. And last, but not least, it gives us a good estimation of the maximum temporal scale within which that common law can be applied. One can treat the identification of the scaling exponent  $\alpha$  and, as we will see, the non-Gaussian nature of the rescaled PDFs ( $P_s$ ) as a method for quantifying the intermittent character of the time series. A possible interpretation of the rescaling is to treat  $P(\delta Y, \tau)$  as the self-similar solution of the equation describing the PDF dynamics. The mono-scaling of the studied PDFs, together with the finite value of the samples' variance if such exists, indicates that a Fokker-Planck approach can be used to study the dynamics of the unscaled PDF  $P(\delta Y, t)$  in time and with respect to the coordinate  $\delta Y$  (*van Kampen*, 1992). Recently a fractional FPE has been obtained that can be used to treat Lévy walk PDF dynamics (*Schertzer et al.*, 1995). Alternatively, the anomalous diffusion of the PDF, consistent with truncated Lévy walk, can be obtained by introduction of a functional dependence of the diffusion coefficient on the “spatial” coordinate.

### 2.2.3 Finite size scaling for spatially extended systems.

So far, the rescaling procedures we described operated in the temporal domain. In the case of the spatially extended systems a similar techniques are used but the

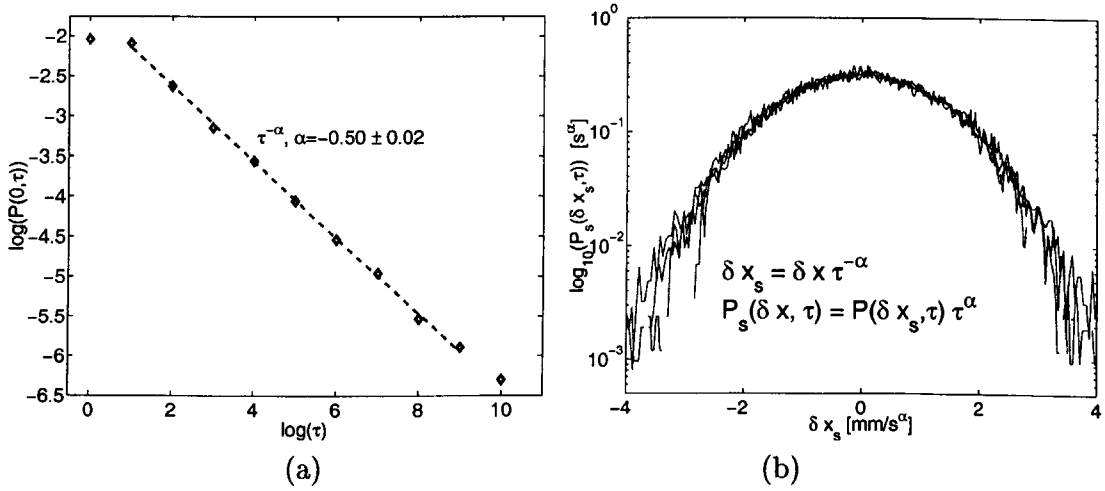


Figure 2.10:  $P(0, \tau)$  scaling as a function of time lag  $\tau$  (a) and the PDFs rescaled according to (2.27) (b) for a Brownian walk time series.

rescaling is performed for spatial variables. SOC models are often studied analytically using Renormalization Group which requires taking a limit of the infinite system size (*Tam et al.*, 1999; *Jensen*, 1998). Thus, strictly speaking, the analytical results obtained from such analysis are relevant only for infinite size systems. Available experimental data as well as computer simulated results, however, are always obtained from finite size systems. That presents a problem of developing methods to verify the relevance of the analytical results, obtained for infinite system, to the finite size system investigation. One of the possible solutions is to look for the scale-invariance in the probability density functions. If such scale-invariance can be detected, then the size of the system is not a relevant parameter and analytical and experimental results can be compared. In practice, one tries to determine if the PDFs obtained from the systems of different size are exactly equivalent. For different system sizes  $N$  one tries to collapse the PDFs on a single curve using the following formula:

$$P(\delta Y, N) = N^{-\beta} P_s(\delta Y N^\alpha). \quad (2.29)$$

We should mention that formula (2.29) applies only to purely self-similar processes where the observable of interest scales with a system size  $N$  as  $\propto N^\alpha$ .

Many complex systems exhibits richer scaling where the exponent  $\alpha$  may

be a function of the position within the system itself. Such behaviour is often termed multi-fractal or, in certain cases, multi-scaling and we will now show how such an approach leads to a different scalings than that given by (2.29). Let  $S$  represent a support on which a probability density function of the scalar variable  $X$  is computed. We can imagine that this variable is distributed in patches, each with its own scaling exponent  $\alpha$  and thus  $S$  itself has a fractal structure described by the function  $f(\alpha)$ . Using a box counting method we partition the support  $S$  by covering it with dimensionless boxes of size  $\epsilon \sim 1/N$ , where  $N$  is the size of  $S$ . We assume that the probability of finding a point in the box number  $i$  is proportional to its size  $\epsilon$ :

$$p_i(\alpha, N) \sim A(\alpha)N^{-\alpha}. \quad (2.30)$$

We then suggest that the number of boxes covering set  $S$  for which the scaling exponent assumes value of  $\alpha$  is of the form (*Helsey et al.*, 1986):

$$n(\alpha, N) \sim B(\alpha)N^{f(\alpha)}, \quad (2.31)$$

where  $f(\alpha)$  is a continuous function. With this assumed form of the probability (2.30) we can write the variable  $X_i$ , an averaged value of  $X$  in the box  $i$ , associated with the probability distribution function as:

$$X_i(\alpha, N) \sim A(\alpha)N^{-\alpha} \sum_j^N X_j(\alpha, N). \quad (2.32)$$

, where the sum is over all possible values of  $X$ . Writing the last sum in (2.32) as constant  $C_0$  and dropping the index  $i$  we rewrite (2.32) as:

$$X(\alpha, N) \sim C_0 A(\alpha)N^{-\alpha}. \quad (2.33)$$

Similarly, based on (2.31) we can write down the probability the the measurement  $X$  was drawn from the region with the scaling exponent  $\alpha$  as:

$$P(\alpha) \sim P_0 B(\alpha)N^{f(\alpha)}. \quad (2.34)$$

Equations (2.33) and (2.34) will form the basis of our further analysis. First, we will consider a case where both  $A(\alpha)$  and  $B(\alpha)$  themselves exhibit a power law scaling with index  $\alpha$ . In such case, we will write

$$X(\alpha) \sim X_0 \left( \frac{N}{N_0} \right)^{-\alpha}, \quad (2.35)$$

and

$$P(\alpha) \sim \left( \frac{N}{N_0} \right)^{f(\alpha)}. \quad (2.36)$$

These assumptions lead to the following scaling formula (indices  $i$  has been omitted) (*Kadanoff et al.*, 1989):

$$\frac{\log(P)}{\log(N/N_0)} = f(\alpha) \quad \text{where} \quad \alpha = -\frac{\log(X/X_0)}{\log(N/N_0)} \quad (2.37)$$

Parameters  $X_0$  and  $N_0$  are fitting constants that optimize the collapse of all  $P(X, N)$  onto a single curve given by  $f(\alpha)$ . This procedure is quite different from the simplest rescaling (2.29) where exponents  $\alpha$  and  $\beta$  are usually chosen in an *ad hoc* manner. We also note that constants  $X_0$  and  $N_0$  are typically, but not always, related to the smallest observed values of observable  $X$  and the size of the grid.

In *Vlahos et al.* (1995) another approach, termed multi-fractal, has been proposed. The appropriate scaling formula has been derived from (2.33) and (2.34) by assuming that both  $A(\alpha)$  and  $B(\alpha)$  are represented by constants. This multi-fractal scaling form is than given by:

$$\frac{\log(P/P_0)}{\log(N)} = f(\alpha) \quad \text{where} \quad \alpha = \frac{\log(X_0/X)}{\log(N)} \quad (2.38)$$

Parameters  $X_0$  and  $P_0$  are, again, fitting constants that optimize the collapse of all  $P(X, N)$  onto a single curve. Rescalings (2.37) and (2.38) yield a spectrum of the scaling indices, given by the derivatives  $df/d\alpha$ . We shall note that the PDF of the SOC systems are power laws and as such do not fall into a class of the stable distributions. Experiments show, however, that such power laws are stable in the sense that their power law index is the same regardless of the length of the considered time interval. We should also point out that, especially in computer simulations,

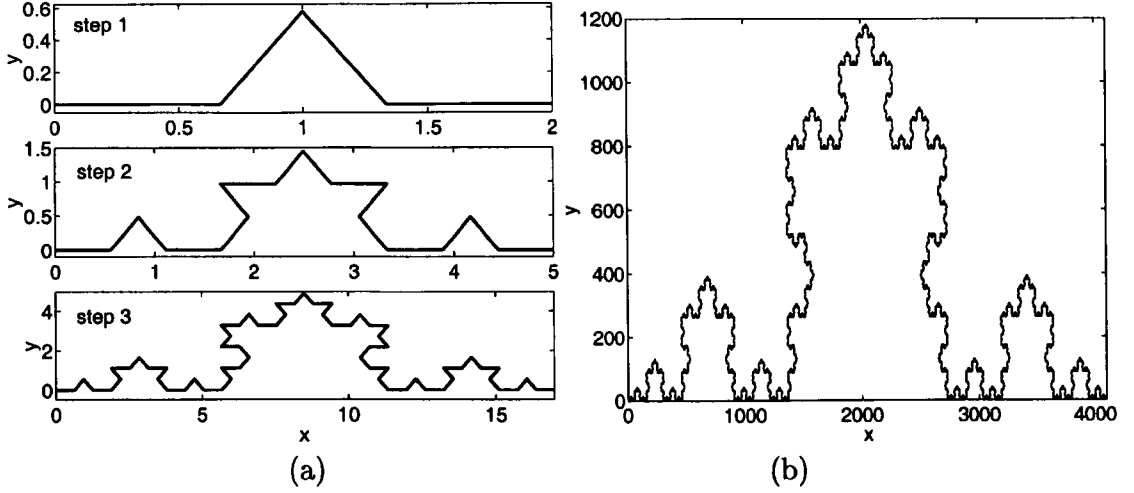


Figure 2.11: First three iterations of the von Koch snowflake (a) and the same curve after 6 iterations (b).

one can obtain directly the increments of the investigated variable. In such case, the differencing (2.25) is not performed. The time series  $\delta Y(t, N)$  is then experimentally obtained from the system of size  $N$ .

## 2.3 Fractal analysis

Both SOC and turbulent systems exhibit complex and nonlinear dynamics. The time series obtained from these systems lack periodic oscillations and have a very intermittent character that can not be reproduced using a linear system with stochastic input. The classical data analysis methods, such as spectral analysis, are not adequate in such cases and new nonlinear time series analysis methods need to be applied. Among these methods, one can consider a fractal and multi-fractal approach which can be applied to time series itself or to a reconstructed phase space attractors.

The concept of fractals was introduced around 1975 by Mandelbrot to characterize geometrical objects that possess no natural length scale. Self-similarity and fractional dimension are two most celebrated features of such geometrical objects. Self-similarity, the consequence of the lack of a characteristic scale, means that the given object preserves its features under the change of scale. The fractional dimen-

sion allows us to distinguish between regular Euclidean objects and fractal ones. Fractal dimension of a Euclidean object is identical to its topological dimension and is represented by an integer. The dimension of a straight line is 1 and that of a square is 2. A concept of dimension can be generalized for any compact subset of a metric space. For each  $r > 0$ , let  $N(r)$  be the smallest number of balls of radius  $\leq r$  necessary to cover a compact subset  $S$ . Suppose

$$D = \lim_{r \rightarrow 0^+} \frac{\log(N)}{\log(1/r)} \quad (2.39)$$

exists. Then,  $D$  is called the fractal dimension of  $S$ . Such defined dimension, unlike the topological dimension, need not be an integer. It does, however, give a correct integer value for the dimension of the typical Euclidean objects. Figure 2.11(a,b) presents iterative procedure for constructing a fractal curve, the von Koch snowflake. Using the equation 2.39 one obtains the fractal dimension of the Koch curve to be  $D = 1.26\dots$ . This non-integer dimension reveals unusual properties of the fractal curve. It fills more space than a line but less than a Euclidean area of a plane. After the infinite number of iterations, the length of the curve is infinite but the area enclosed by it is finite. Although fractals were originally developed to investigate the properties of the geometrical objects, the concept can be applied to investigate the dynamics of the complex natural systems. Such studies can be done in several different ways. Here, we will explore two possibilities: using the time series itself as a geometrical object and reconstructing a low-dimensional attractor in the phase space.

### 2.3.1 Self-similarity and fractal dimension of time series

An observed time series is often the only link between the natural system and the physical theory or a model developed to describe its dynamics. The complexity and irregularity of the time series obtained from the complex systems is such that no single model can be found to recreate the behavior. The ultimate goal of fractal analysis is to establish an iterative algorithm, similar in concept to that of von Koch snowflake, that would allow us to create a time series of any desired length and any

requested resolution. The quest for such a prescription must start with detecting self-similarity and then, if such can be found, proceed to obtain a fractal dimension. There is, however, an important difference between geometrical objects and time series traces when detecting self-similarity is considered. For geometrical curves embedded in a 2-dimensional plane, both axes represent the same physical variable, while two axes of the time series usually represent different physical variables, with different units and scales. Such non-uniform scaling, where the object is invariant under transformation that scales different coordinates by different amounts, is known as self-affinity. Comparing original and a rescaled copy of the time series also requires a different approach from that applied to geometrical objects. The rescaled copy of a time series should represent the same dynamical process that generated the original sample but occurring on a different scale. One can easily imagine the situation where, by rescaling the spatial or temporal domain, a different physical processes may come into play or vanish. To verify that the rescaled time series still represents the same physical processes, statistical measures, such as Probability Distribution Function (PDF), can be used. Hence a test for detection of self-affinity of the time series needs to include two steps. First, we take a subset of the object and rescale it to the same size of the original object, using different magnification factors for its width and height. Then we compare the statistical properties of the rescaled object with the original one. The procedure can be represented by the following statement:

$$\forall r \in (0, t_{max}] \quad \exists H \quad \text{such that} \quad Y(t) \doteq r^H Y\left(\frac{t}{r}\right) \quad (2.40)$$

where  $r$  is a rescaling factor and  $\doteq$  means that the statistical properties of both sides of the equation are identical. The exponent  $H$  is called the self-affinity or Hurst exponent. One should note that in practice the statistical equivalence in (2.40) should apply to all moments of the PDF. The weaker approximation is usually used that examines only the first two moments. For the time series with a PDF represented by a power law, with an exponent close to 1, not only variance but even a mean value may not exist.

Although, as we discussed above, a time series rarely exhibits pure self-similarity, the fractal dimension can still be used to obtain the Hurst exponent.



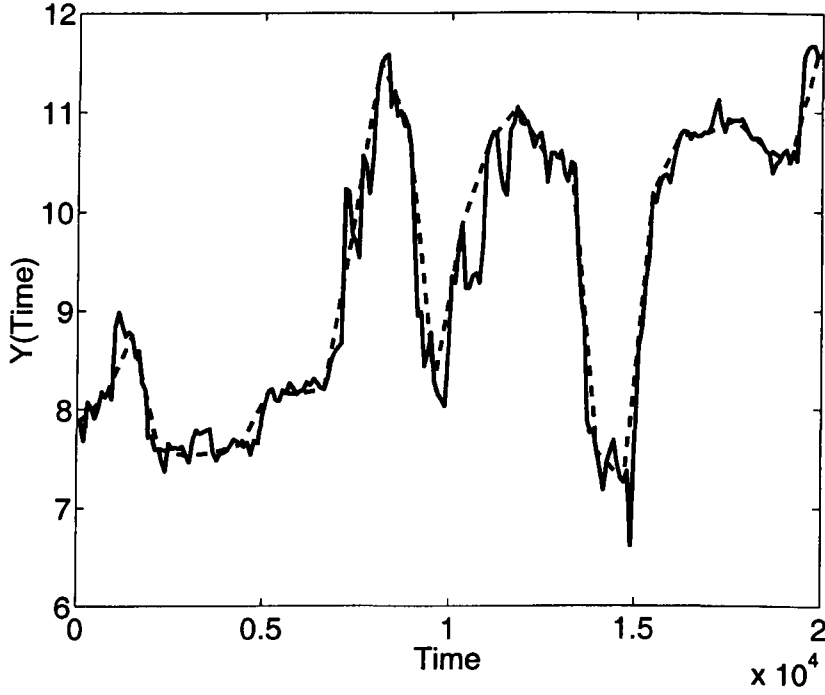


Figure 2.12: Time series length approximation with a yardstick of length  $r$ . Here  $r^2 = (Y_{i+8} - Y_i)^2 + (T_{i+8} - T_i)^2$ .

Many methods exist that when applied to a time series allow us to find an approximate value of the fractal dimension. Among the most popular are the box counting method and the divider or length scaling method. Here, we will concentrate on the second method which was used, both analytically and numerically, to study the energy curve of the sandpile model presented earlier. The technique consists of computing the length of the given curve by measuring it with the yardstick of length  $r$ . As the length of the yardstick decreases and the measurement becomes more detailed, the length of the curve increases. Figure 2.12 shows such curve length approximation with a yardstick of length  $r$ . The length of the yardstick is given by its end points  $r^2 = \delta y^2 + \delta t^2$ , where  $\delta y$  is the difference between two measurements in the time series separated by time difference  $\delta t$ . The results obtained from this method are sensitive to the ratio  $\delta y / \delta t$ . It was shown in *Schmittbuhl et al. (1995)* that the correct scaling can be obtained only if  $\delta y \gg \delta t$ . In such case, the length of the time series is given by:

$$L(r, t_{max}) = N(r, t_{max})r \propto t_{max} r^{1-D}, \quad (2.41)$$

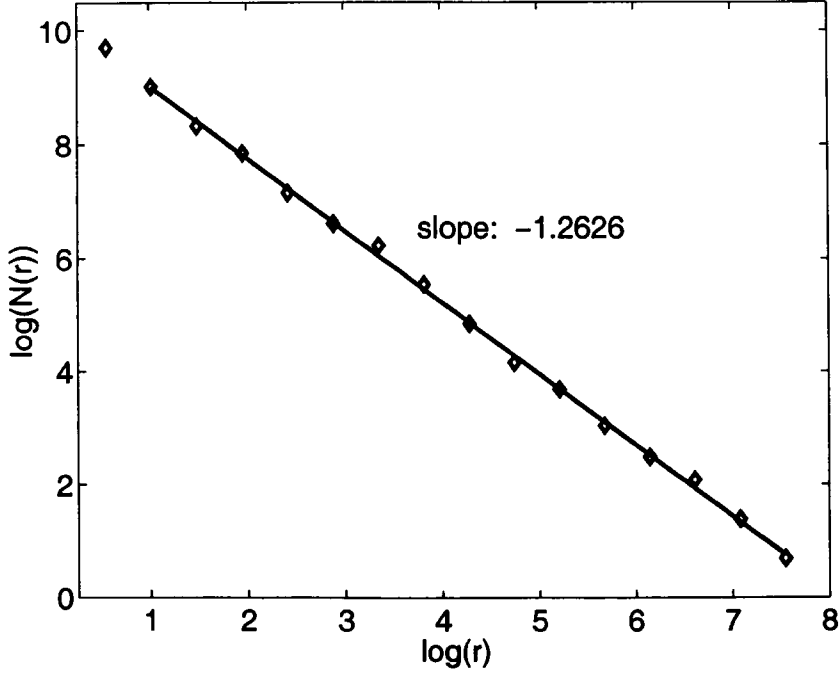


Figure 2.13: Fractal dimension estimation via the length measurement of the von Koch curve. Fractal dimension  $D = 1.2626$  is given by the slope of the fitted line. Confidence level 95%.

where  $N(r, t_{max})$  is the number of the line segments of length  $r$  and  $D$  is a fractal dimension. It can be shown (*Hentschel and Procaccia*, 1984) that the relation between the fractal dimension  $D$  and the Hurst exponent  $H$ , in two dimensions, is given by  $D = 2 - H$ . Figure 2.13 shows the scaling  $N(r, t_{max}) \propto r^D$ , on the log-log plot, obtained for the von Koch fractal with 6 iterations applied. The fractal dimension obtained here is quite accurate and agrees with one found by (2.39).

### 2.3.2 Embedding, phase space reconstruction and fractal dimension of the attractor

The self-similarity of the time series is a strong indicator of a self-similar processes occurring within the system, but the connection between the features of the time series and the dynamics of the system is not straightforward. Phase space reconstruction allows us to study the dynamics of the complex systems in their canonical form, i.e., using the optimal number of the degrees of freedom (*Crutchfield and McNamara*, 1987; *Crutchfield and Young*, 1989). The method was originally de-

veloped to study chaotic systems where the complex dynamics coincides with the low dimensional attractor in phase space. The fractal dimension of the attractor provides an upper bound on the number of the differential equations needed to fully describe the dynamics of the system. Recent studies by *Chang* (1992); *Osborne and Provenzale* (1989) indicate that this technique can be used for the analysis of the dynamics of the spatially extended self-organizing systems such as sandpile. Indeed, such systems often exhibit low dimensional structures in phase space. To obtain a fractal dimension of the attractor from the time series, a phase space reconstruction process needs to be applied first to find the right embedding dimension for the system's dynamics. This is done by the method of the delay reconstruction of the time series. Let  $s_n$  be the  $n$ -th value in the time series. A delay reconstruction in  $m$  dimensions is formed by the vectors  $B_n = (s_{n-(m-1)v}, s_{n-(m-2)v}, \dots, s_{n-v}, s_n)$ . The parameter  $v$  is the delay parameter. The embedding dimension theorem guarantees that, for relatively noise-free data, there exist a dimension  $m$  such that vectors  $B_n$  are equivalent to the phase space vectors. For an infinitely long time series an arbitrary delay parameter  $v$  can be taken, but in practice results of the reconstruction are very sensitive to the choice of value for  $v$ . Generally, a delay parameter has to be selected in such a way to assure the independence of coordinates for the reconstructed vector  $B_n$ . Several algorithms can be used to estimated the optimal time delay  $v$ . The most popular method is based on the autocorrelation function of the signal defined as:

$$c_v = \frac{1}{\sigma^2} \langle (s_n - \langle s \rangle)(s_{n-v} - \langle s \rangle) \rangle, \quad (2.42)$$

where  $\sigma^2$  is the variance of the investigated time series. A rule, discussed in *Kantz and Schreiber* (1997), is to choose the time where the autocorrelation function decays to  $1/e$  with increasing time delay. This value of  $v$  should minimize the spreading of the attractor in phase space and lead to a good estimate of the fractal dimension. *Fraser and Swinney* (1986) demonstrated, however, that the first minimum of the mutual information could give a better estimate of the optimal  $v$ . Let  $p_i$  be a probability that the signal assumes a value given by the  $i$ th bin of the signals histogram. We find conditional probability  $p_{ij}(v)$  that the signals value  $s(t+v)$  is in bin  $j$  while

$s(t)$  is in bin  $i$ . We then define the mutual information as:

$$I(v) = \sum_{ij} p_{ij}(v) \ln(p_{ij}(v)) - 2 \sum_i p_i \ln(p_i). \quad (2.43)$$

Quantity  $I(v)$  expresses the amount of information about  $s(t+v)$  that one can recover from the known value  $s(t)$ . The first minimum of (2.43) indicates the time lag  $v$  where  $s(t+v)$  contributes maximum additional information to that already obtained from the measurement  $s(t)$ .

Knowing the values for both embedding dimension and the delay parameter, it is possible to reconstruct the attractor and estimate, numerically, the value of its fractal dimension. Fractal dimension estimation of the complex phase space structure represents natural extension of the methods used in the studies of the self-similar geometrical objects. The dimension can be estimated by dividing the  $n$  dimensional Euclidean space, containing the data set, into the grid of hypercubes of size  $L^n$  and counting the number of such cubes  $n(L)$  that are non-empty. Let the self-similar object be initially covered by a box of  $L_{max}$  size. If one subdivide the maximum box each of the  $N = \frac{1}{r^D}$  points will fall within one box of size  $L = rL_{max}$  where  $r < 1$  and  $D$  is a box counting or capacity dimension. One can also generalized the concept and consider a higher moments of the fractal dimension. The generalized dimension of order  $q$  is defined as:

$$D_q = \frac{1}{q-1} \lim_{\epsilon \rightarrow 0} \frac{\ln(\sum_{i=1}^{N(\epsilon)} p_i^q)}{\ln(\epsilon)} \quad (2.44)$$

Where  $p_i^q$  is a probability density of  $N_i$  points being present in box  $i$ ,  $\epsilon = 1/r$  is a size of the covering boxes and  $N(\epsilon)$  is the number of boxes used to cover a given set. First three moments are the most widely used in the literature and are called:

1.  $q = 0$  Capacity Dimension
2.  $q = 1$  Information Dimension
3.  $q = 2$  Correlation Dimension

The correlation dimension is the most widely used statistical parameter to characterize fractal phase space structures of a dynamical system. The correlation sum

algorithm is the least sensitive to noise and exhibits good convergence for the finite size data sets (*Kantz and Schreiber, 1997*). Calculation of the correlation dimension is relatively easy but the definition, given by (2.44), is not optimal for numerical implementation. It has been shown that the same results can be obtain if one counts the number of pairs in the time series with a distance smaller then  $\epsilon$  (*Grassberger and Procaccia, 1983*). The correlation sum can then be defined as:

$$C(\epsilon) = \frac{2}{N(N-1)} \sum_{i=1}^N \sum_{j=i+1}^N \Theta(\epsilon - |x_i - x_j|) \quad (2.45)$$

Where  $\Theta$  is a Heaviside function. One usually plots  $C(\epsilon)$  as a function of  $\epsilon$ , on a log-log scale, and then looks for the linear behavior on the plot in its middle section. The slope of the fitted line estimates the correlation dimension. To eliminate the pairs that are close due to residual time correlation and not their true position in the phase space, a space-time plots can be used. The plots provide a value of the maximum window needed for the numerical search of the near neighbors. We should stress the difference between the analysis of the sandpile model and a system where chaotic dynamics is expected. In the later case one needs to determine that the dynamics is deterministic and not purely stochastic. This can be done by computing Lyapunov exponents or performing a surrogate data test. If the dynamics of the system is indeed deterministic, one can use correlation dimension to determine the number of degrees of freedom needed to describe the system. In the case of the sandpile, the exact character of the dynamics is known, i.e., we know that the complex behavior is due to the nonlinearities and the long range correlations. Here we attempt to use the correlation dimension of the phase space structure to determine the proximity of the system to its critical point. In Chapter 4, we will apply this technique to investigate the phase space attractor of the sandpile model.

## Chapter 3

# Scientific Visualization and Data Mining

Recently, advanced visualization techniques has received increasing attention among scientists and engineers. These techniques not only allow a direct analysis of multi-dimensional structures to provide intuitive and quick comparison of experimental data with model results, but also yield quantitative measures to support or negate the model itself (*Hnat et al.*, 2000). Here, we demonstrate the use of the immersive Virtual Reality (VR) visualization in the study of the sandpile model described in section 1.1. The emergent phenomenology of the model is broadband, but can be represented on a finite grid making it very suitable for scientific visualization. Two generic features of a sandpile model, namely the large number of degrees of freedom and a multi-scale character of the dynamics, introduce some complex problems to the task of the visualization (*Hnat and Chapman*, 2000). The large number of the degrees of freedom contributes to extremely large data sets while the multi-scale character of the data does not allow us to neglect any of the details. This represents a generic problem of visualizing multi-scale structures in data sets derived from non-linear systems, where one needs to retain all the information required for understanding a decimated data set without a priori knowledge of the region of interest. To achieve sufficient speed in real time display and to ultimately facilitate

fast responds to user's requests, the full data set must be represented graphically in a compact form without loss of information. We present a novel approach into data set reduction and visualization of the multi-scale surface. We discuss a development of the intelligent data set reduction algorithm as well as a data mining technique that combines traditional two-dimensional representation of the data with three-dimensional view of the complex surfaces. This is a new approach to the studies of the avalanching systems, such as the sandpile model, and we will discuss immediate benefits of this method in understanding the complex behavior of the system. The software modules were developed in OpenGL<sup>TM</sup> and Glut<sup>TM</sup> library and are implemented in semi-immersive VR on ImmersaDesk<sup>TM</sup>.

### 3.1 Virtual Reality and Scientific Visualization

Most physical experiments, be they laboratory measurements or computer simulations, generate time series characteristic for the investigated system. Very often collected data presents more structure that can be analyzed using traditional methods. One of the possibilities to enhance the well-known techniques is to supplement the researcher with a three-dimensional visualization tool. Here, we discuss software developed to visualize results of the sandpile simulation with inherently multi-scale output. Many complex models of non-linear physical systems (such as Computational Fluid Dynamics or CML) characteristically yield gridded data that are inherently multi-scale (*Bak et al.*, 1987). The sandpile model provides a relatively straightforward test case for other multi-scale systems where grids may be in addition irregular and non-uniform. To study the dynamics of the sandpile in space and time, requires simultaneous display of structures differing in scale by several orders of magnitude.

The challenge in visualization of the data from the spatially extended models comes not only from its multi-scale character but also the size and complexity. Available algorithms such as visibility culling, triangle or polygonal surface simplification (*Watt and Watt*, 1998) have serious limitations when used for scientific

applications. Details of the structure are often neglected or compromised to minimize the size of the data set (*Chow, 1997; Barnsley et al., 1988*). This may lead to false conclusions about the investigated system. Therefore, in this case, it is critical that the full three-dimensional surface is retained with all the information required for understanding a decimated data set without a priori knowledge of the region of interest. Another problem that most visualization applications must overcome is real-time managing and rendering of the data. For applications that perform data storage, some optimization and compression of the geometry can be performed to speed up future rendering. Most scientific applications, however, must respond to user's interrupts at a speed that makes any disk storage rather impractical to use. A scientific visualization of the multi-scale data sets must balance the amount of data required to study the system and amount of time needed to compute, encode and display that data. The goal of this project was to develop a tool for display and analysis of the large, multi-scale structures, that is, with generic features on different scales. To achieve this, one has to be able to select interesting regions of the structure and focus on its detailed topology as well as gain an appreciation of trends in the data over its entire dynamic range. We will discuss developing, in OpenGL<sup>TM</sup>, rendering techniques for real-time display of the multi-scale data. We also attempt to combine two data sets, using OpenGL<sup>TM</sup> blending algorithms to study the impact of the changing parameters on the sandpile evolution. Information of detailed structure in the sandpile has also been coded into the sound, which can be played simultaneously by the user to further enhance pattern recognition in the data.

### 3.1.1 System and Application Overview

The development of the program was performed on two different platforms. The concept was prototyped on the SUN Ultra-2 workstation with 256 MB of memory and Creator 3D graphics card. After initial code verification, the program was ported to the ImmersaDesk<sup>TM</sup> VR system driven by Silicon Graphics Origin2000 machine with 8 processors, 2 graphics pipes and Onyx2 operating system. The ImmersaDesk<sup>TM</sup>



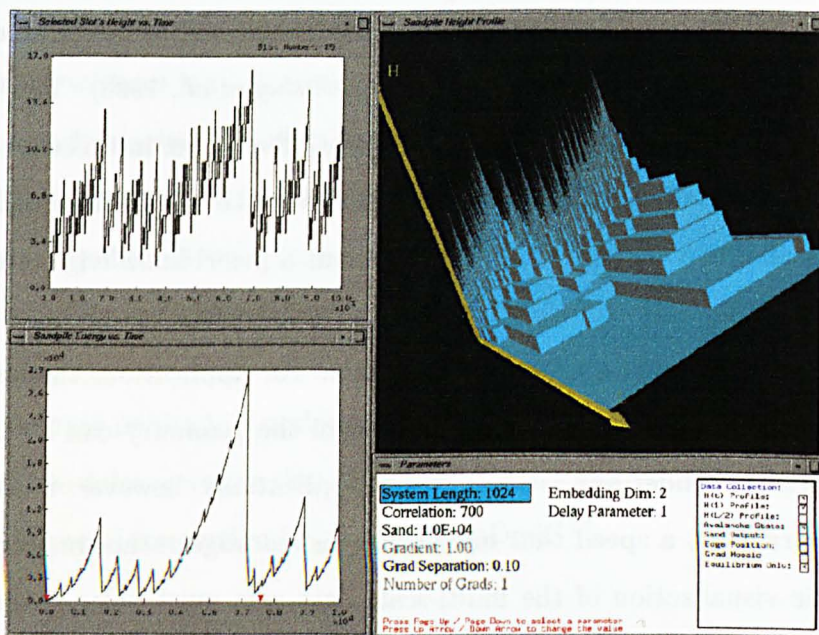


Figure 3.1: A complete user interface of the sandpile simulation and visualization program. The interface allows rapid visualization of the sandpile dynamics in 3-D VR space as well as performing basic analysis of the collected data.

is a drafting-table format virtual prototyping system. Using stereo glasses and IR head and hand tracking, this projection-based system offers virtual reality that is semi-immersive and shared. The system features  $4 \times 5$ -foot rear-projected screen at  $45^\circ$  angle. The size and position of the screen give a sufficiently wide-angle view and the ability to look down as well as forward. The resolution is  $1024 \times 768$  at 96 Hz. The application described here was developed using *C* and OpenGL<sup>TM</sup> graphics library on the UNIX platform. OpenGL<sup>TM</sup> is an industry standard for three-dimensional visualization. It provides not only a complete Application Programming Interface (API) for drawing 3-D primitives but also sophisticated shading, lighting and blending algorithms. The Graphical User Interface (GUI) was developed using Glut<sup>TM</sup> library. Figure 3.1 shows the complete user interface with a sample output data. The application uses four windows to display all the required information. The “Parameters” window provides the top-level control of the software. It allows the user to modify input parameters to the simulation and select the amount of output data to be stored in memory for the more detailed analysis. The

“Time Series” window, apart from displaying the output data, makes it possible to zoom-in (holding down third mouse button) on a region of interest that will be also represented as a three-dimensional surface. The “Analysis” window provides the user with numerical tools to investigate the data. These include line fit, building histograms and computing fractal dimensions of the curves. All options relevant to a given window are available through the pop-up menus.

### 3.1.2 Visualization Methods

The choice of the visualization algorithms used in this program, was influenced by the following factors related to application’s specification:

1. Real-time display rate for the large range of the system parameters and sustaining frame rates up to 22 frames per second required by ImmersaDesk<sup>TM</sup> environment.
2. Maintaining the original accuracy of the evolution surface with smooth transitions between the regions with varying levels of detail.

The majority of the visualization and surface optimization methods used for the height field structures evolved around triangulated irregular network (TIN) algorithm (*Chow, 1997; Lindstrom and Turk, 1998*). In this method, the grid is modified to contain larger number of points in the areas of more detailed topology. Using a TIN algorithm, one can approximate the surface with any given accuracy and with fewer polygons then required by other methods. The TIN method, however has one serious drawback – it requires some *a priori* knowledge about the generated surface. One has to know which areas of the surface will contain higher levels of detail to build the grid appropriately. If the position of these areas can not be predicted correctly, even a small size TIN may require a spatial reorganization of the grid and the visualization can not be performed in real-time.

The second method researched for this project was a “level of detail” (LOD) algorithm introduced in *Lindstrom et al. (1994)*. The algorithm operates on the uniform grid and does not require any pre-processing or any *a priori* knowledge

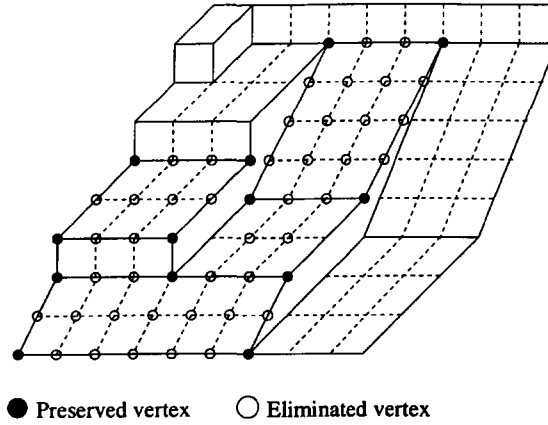


Figure 3.2: Vertex reduction method based on the normal vector direction change.

about the surface. We will discuss the details of this algorithm in a later section. A uniform grid representation is often superior to irregular grid method, it is compact, easier to manipulate and allows fast reconstruction of the surface for different level of detail. Clear spatial organization of the grid makes it easy to index and store efficiently in the memory - a very important feature if the real-time rendering has to be achieved. We selected a rectangular topology for the grid as the most intuitive in our case. Each vertex of the grid contains its coordinates, normal vector, needed for the surface optimization process, and a color index that can be used to visualize additional system parameter (through the color coding technique), for example, the avalanche length associated with each relaxation. It should be pointed out, however, that the color coding must be done using texture mapping as not to interfere with the surface optimization algorithm. Finally, the mesh is generated using the OpenGL<sup>TM</sup> display list facility combined with lighting, shading and blending algorithms.

### 3.1.3 Data Set Reduction and Surface Optimization

The storage requirements for the presented problem are quite stringent. A typical run of the simulation generates between  $10^5$  to  $10^6$  records. Each record contains energy data, avalanche data and heights profile. If the performance of the application is not to be compromised, one has to find simple, yet efficient methods to reasonably reduce the original data set. Closer analysis of the sandpile output struc-

tures suggested that two reduction schemes could be applied. First of all, one need to store only that part of the height profile that was effected by the last relaxation event - other heights remain the same. Secondly, the run length encoding can be used for further data size reduction. After each relaxation, the modified heights are scanned. If the heights in the neighboring sites are the same, only one record is used to record the heights together with its start and end position. Additionally, the size of the data set increases if the dynamic parameter color mesh is displayed together with the height profile. The color mesh of the dynamic parameter is stored in a very compact form; no value of the parameter is stored but only an index to a matrix where the two possible values of the parameter are stored. Since the index can be only zero or one, we pack 8 indices in one character type variable (8 bits long). One of the common problems with using regular grid representations of the surface is that the polygonal mesh is never the optimal one. Since large, flat areas may coexist with very dynamic ones different regions need to be optimized differently based on the details of the topology it included. The simplification method used here is the "level of detail" (LOD) algorithm (*Lindstrom et al.*, 1994). We use iterative reduction code that replaces many small polygons with fewer larger ones. The normal vector direction change is used to estimate the amount of information loss during the surface coarse graining process. If selected polygons are to be fused, we require that the normal vectors had exactly the same direction. The process starts with a grid at its highest resolution. A doubly link list, used to store the mesh, is traversed and all polygons that meet our criteria are joined together. Figure 3.2 shows how few polygons with the same slope are replaced with a larger one without any loss in accuracy. The data structure used allows immediate release of the purged polygons. This reduces the number of polygons by an order of magnitude on average (see table 3.1.3). The algorithm is applied only once before the final polygonal mesh is created using OpenGL<sup>TM</sup> functions. We do not re-optimize the surface for every rendered frame and allow OpenGL<sup>TM</sup> algorithms to handle the viewpoint or field of view changes. It should be stressed that this method does not eliminate any details from the original data set and thus the image always reflects the true evolution of the



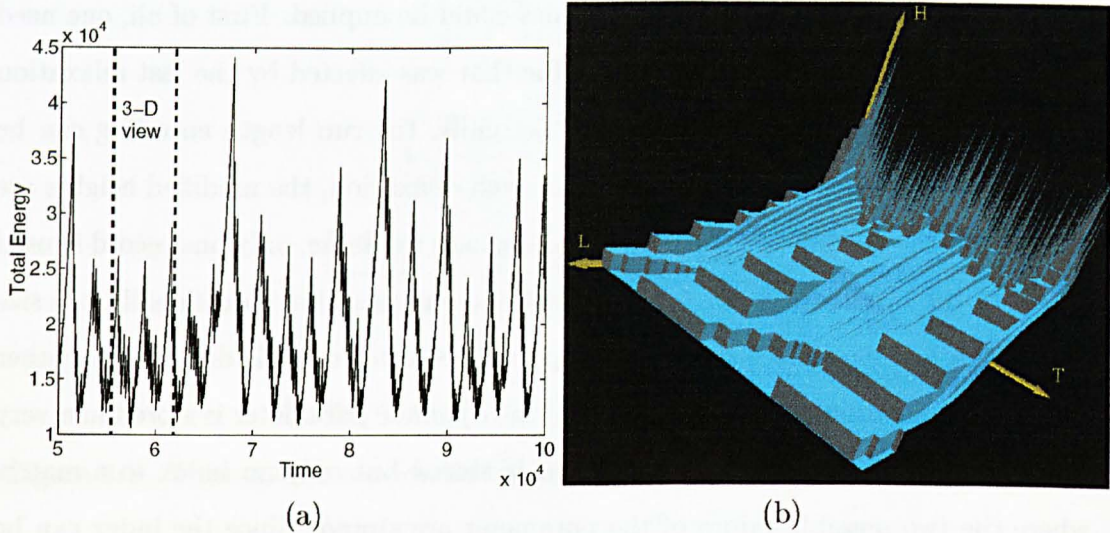


Figure 3.3: (a): State variable (total energy) of the sandpile dynamics and (b) corresponding 3-D view of the sandpile height profile.

system. If, however, one needs to reduce the size of the structure further an error parameter can be added to allow the fusion of the polygons with normal vectors differing by a given amount. This optimization is fast and allows a real-time display of the surfaces originally consisting of up to 500,000 polygons.

One of the most common method used to visualize high-dimensional data sets is color meshing. Additional system parameters may be mapped to a color of the underlying polygons. The use of the LOD algorithm, however, makes the simple color coding of the surface impossible as some polygons will be eliminated during the process. Since all our additional parameters are functions of time (and not the position within the system), one could restrict LOD algorithm to coarse grain the surface only along the system length axis. In our case, this method did not provide sufficient enough reduction in the number of polygons. The texture mapping technique will be explored to avoid the constraints of the color meshing.

### 3.1.4 Data Mining and Visualization Results

The usual method of summarizing the evolution of a complex system over its entire bandwidth is to use a state variable graph. Figure 3.3(a) shows a time evolution of the total energy (the state variable) of the thresholded sandpile system. The

simplicity of the plot allows display of the entire evolution of the system. This is crucial, since it indicates the interval where the time series reached a steady state. The multi-scale character of the system is also revealed. In the equilibrium state, the energy plot has a clearly self-repeating pattern. Different spatio-temporal scales of these oscillations allow us to expect the existence of similar features in the generated three-dimensional image. A state variable graph, although very informative, does not provide enough clues to understand collective behavior of the sand in the model.

Figure 3.3(b) presents the surface of the sandpile profile in time that corresponds to this steady state. The three-dimensional surface can be rotated, translated and viewed in a close-up mode by the user. Such a method, where the user is guided through the full data set to search for relationships and global patterns that exist in it, is called data mining. The novelty of our method lies in the fact that we employ a simple two-dimensional graph that is capable of displaying the entire data set, regardless of its size and complexity as a guide. The researcher is allowed to select a region of interest and explore the trends, otherwise hidden among the vast amounts of data, in three-dimensions. The benefits of this approach are: the fast display of the 3-D images (only the selected region needs to be processed), ability to examine different regions of the model's dynamics quickly and the opportunity to compare generic features in the state variable graph with those present in the 3-D height profiles.

Looking at figure 3.3(b) the multi-scale character of the structure is very obvious. The topology of the surface varies strongly with distance across the system and time—it is an inverse cascade from small to large scales. Over a short length

System Size	Algorithm Applied	Output	Polygons
256	None	69 MB	132608
256	Data Reduction	8.0 MB	30500
256	Data Reduction and Surface Optimization	6.4 MB	2500

Table 3.1: Data set size before and after optimization.

range, one can observe short peaks oscillating in time. The structure contains complex patterns that could not be predicted without three-dimensional imaging. Two very distinct regions are clearly visible on the figure 3.3(b). First one takes the form of long and smooth slopes and corresponds to a descending side of the total energy curve. The other, "step-like" structures are characteristic of a growing side of the energy curve. Since different regions of the surface must be studied in a close-up mode, it is very apparent that the use of LOD algorithm was necessary. The image on figure 3.4(a) presents a special case in our studies—an exact analytical solution exists for this sandpile model (*Helander et al.*, 1999). This special case has simple self-similarity and in consequence information on all scales is of equal importance. This case allowed us to test the efficiency of our visualization techniques against the existing mathematical model. The next simplest case is when the dynamic rules include a control parameter that can assume only two values (with equal probability). To study the correlation of this dynamic parameter with the behavior of the system, the two data sets are visualized simultaneously in a three-dimensional view (see figure 3.4(b)). A flat color mesh representing two values of the dynamic parameter is drawn under the translucent, three-dimensional sandpile profile surface. OpenGL<sup>TM</sup> alpha blending algorithm was used to achieve the effect of the translucent evolution surface. In this three-dimensional view, one can notice that the edges of the surface facets tend to align with the area of change of the dynamic parameter.

The scientific visualization of the complex structure is not a goal in itself, of course. The methods presented here allow an instant insight into the dynamics of the system and thus allows us to draw analogies between the model and real physical systems (*Hnat et al.*, 2000).

### 3.1.5 Quantitative Sonification

Quantitative sonification was also used to enhance user's experience of the explored system. In our case, we used sound to improve the analysis of the most complex areas of the surface. The frequency of the sound, its volume and duration are all based on



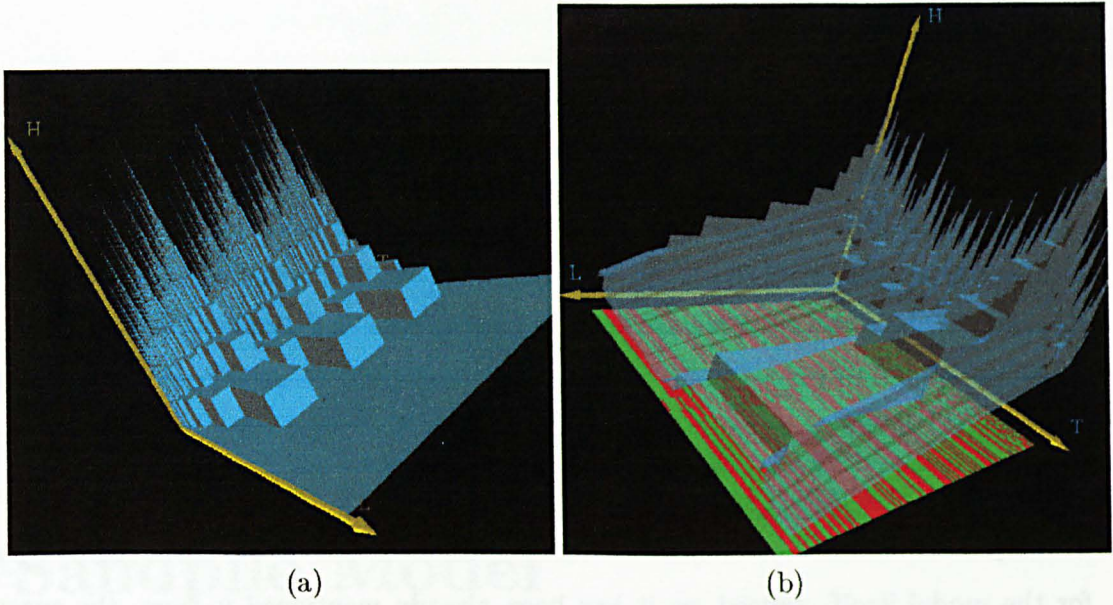


Figure 3.4: 3-D visualization of the sandpile height profiles for (a) purely self-similar solution and (b) with stochastic parameter represented as a colour mesh.

the sequence of avalanche lengths in time. The choice of the parameter was based on the analytical solution presented in figure 3.4(a). In this special case, of the sandpile with dynamic rule acting over the length of the system, avalanche lengths are shown to only exist with lengths  $2^n$  cells (where  $n$  is an integer) (*Helander et al., 1999*). For other values of the range of the redistribution rule, the small avalanches cluster around values of  $2^n$ . The avalanche lengths are hence approximately always linear on the logarithmic scale and so are tones in the octave. Combined with a "close-up" view of the structure sonification is an additional tool for visualization of the multi-scale topology. In particular it flags to the user underlying regular patterns in the time series that would be difficult to see on the visual representation of the sandpile. Standard UNIX audio device is used to generate the sound. The *ioctl* C function is used to interact with the device and set its parameters. We found, however, that the large disadvantage of sonification is that various parameters describing the sound can influence each other (i.e., the volume and the frequency of the sound) giving false perceptions of the changes within the system.



### 3.1.6 Conclusions

Many modern measurements of plasma systems provide high-dimensional data sets that are too difficult to study using traditional methods. As the available information becomes more and more complex, new and more advanced ways to explore it must be found. Virtual Reality, and scientific visualization in general, proved to be extremely helpful in understanding the sandpile model's dynamics. The visualization revealed striking similarities between the dynamics of tokamak plasma and that of the sandpile. In particular, the visual examination of the 3-D profiles led us to quantitative studies of transport barriers in tokamaks. We will discuss these results in Chapter 5. Direct visual methods can also be used to verify analytical predictions for the model itself. Indeed, as it has been already mentioned in here, the exact results obtained in *Helander et al.* (1999) could be verified via direct comparison of the self-similar height profile patterns. The method, however, has its limitations when quantitative studies are considered. To obtain more than just general trends in the system's dynamics the visual tools need to be accompanied by other quantitative techniques. These have been described in detail in Chapter 2.

## Chapter 4

# Statistical Analysis of the Sandpile Model

There is increasing evidence that the essential dynamics of a range of naturally occurring systems can be captured by the paradigm of Self-Organized Criticality (SOC). Intriguingly, this may include plasma confinement systems both in the laboratory (tokamak plasma), and in space (solar flares, the earth's magnetosphere). These systems depart from the well established formalisms of SOC where the critical point is approached in the limit of vanishing drive and the true scaling behavior is obtained for arbitrarily large events. Instead, we have physical systems with finite size and highly variable driving rates. Yet, they still exhibit bursty energy release events which are self-similar and exhibit inverse power law statistics. This behavior has been recovered in numerical avalanche models for which one can find fixed points and which exhibit corresponding inverse power law burst statistics. These features are robust, against the drive, for large events. We consider such a model which has a "tuning parameter", that can be used to bring the system away from its fixed point. In natural systems, the time series may be the only observable with sufficient dynamic range to test for self-similarity. We use the model to test if the time series alone is sufficient to quantify the system's proximity to its nontrivial fixed point. If not, this may provide a simple explanation for the apparent ubiquity of SOC in nature.

## 4.1 Finite size scaling for the sandpile model

Finite size scaling of the spatially extended systems is a well established technique. The method, described in details in Chapter 2, is especially suited for the numerical models where the system size can be easily varied. Results of the finite size scaling allow us to relate the features found in the data, obtained from the finite size system, to these predicted by the Renormalization Group (RG) where the limit of infinite system size is taken. Scaling indices found in the critical regime, i.e., when system size  $N \rightarrow \infty$ , allow us to introduce the concept of universality classes and group different numerical realizations of the sandpile based on their critical dynamics. In this section, we will present a finite size scaling analysis of the sandpile model introduced in Chapter 2. Our analysis will be performed using energy dissipated in a single event  $dE$  (2.4) and avalanche length  $dl$  observable. The RG analysis of this sandpile model (*Tam et al.*, 1999), performed for parameter  $L_f = N$ , shows that the avalanche length and the energy dissipated exhibit an inverse power law scaling with index  $-1$ . In the case of  $L_f < N$ , such analysis can not be performed due to a coarse graining procedure that fails on the scales larger than  $L_f$ .

The goal of this investigation is twofold. Firstly, we will obtain scaling indices for the sandpile model using finite size scaling. Such analysis has never been done for this model. Values of scaling indices will allow us to identify a universality class for this model. We will also verify results of the analytical RG analysis for the system with  $L_f = N$ . Our main interest will be in establishing the scaling exponent for the large events. We will, however, also investigate the scaling of the small events. Small scale dynamics of the sandpile is not relevant from the universality class perspective but is important in the modeling of the physical systems where dual scaling regimes may be observed (*Lu and Hamilton*, 1995; *Chapman et al.*, 1999). Our second aim will be to determine if the system's proximity to its fixed point can be quantified using a finite size scaling techniques. To facilitate direct comparison with earlier results and other published work, our analysis will be performed using Probability Distribution Functions (PDIF) rather than Probability Density Functions. We note that, in the case of the power law PDIF with exponent  $\alpha$ , the corresponding density

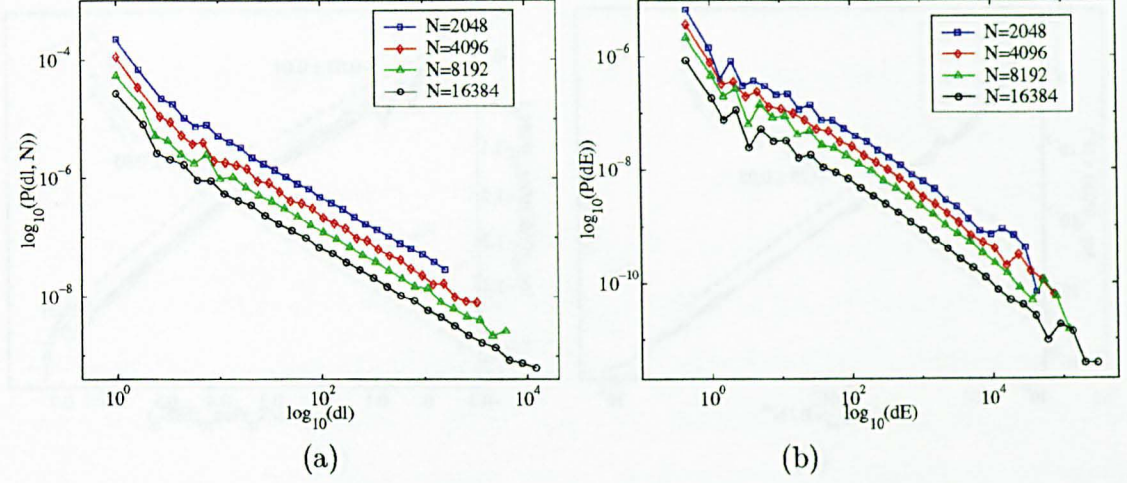


Figure 4.1: PDIFs of the avalanche lengths (a) and dissipated energy (b) for different system's sizes  $N$  and constant control parameter  $L_f$ .

function is also a power law with the exponent  $\alpha + 1$ .

Figure 4.1(a,b) shows the probability distribution functions for the avalanche lengths and the energy dissipated in a single event observed in the sandpile model with varied length  $N$ ,  $L_f = N$  and 2% randomization of the critical gradient. It is immediately visible from the figure 4.1 that the randomization of the critical gradient affects the scaling of small events while the large scale dynamics remains unchanged with a power law index  $\alpha^{dl, dE} = -1$  for both  $dE$  and  $dl$ . The finite size scaling analysis of the PDIFs reveals some differences in scaling between the avalanche lengths, shown in figure 4.2(a) and the dissipated energy presented in figure 4.2(b). The best collapse of the PDIFs for the avalanche lengths is achieved by applying a self-similar finite size scaling (2.29) with parameters  $\alpha^{dl} = 0$  and  $\beta^{dl} = 1$  (used in (2.29)) which can be then written as:

$$P(dl, N) = \frac{1}{N} P_s(dl, N) \quad (4.1)$$

The energy dissipation PDIFs, however, show multi-index scaling consistent with dual regime scaling reported in *Tam et al. (1999)* and *Chapman et al. (1999)*. Consequently, the best collapse of original PDIFs is obtained using the multi-scaling ansatz (2.37) with fitting parameters  $X_0 = 1.0$  and  $N_0 = 0.001$ . Figure 4.2(b) shows how small scale events of the dissipated energy depart from the critical regime



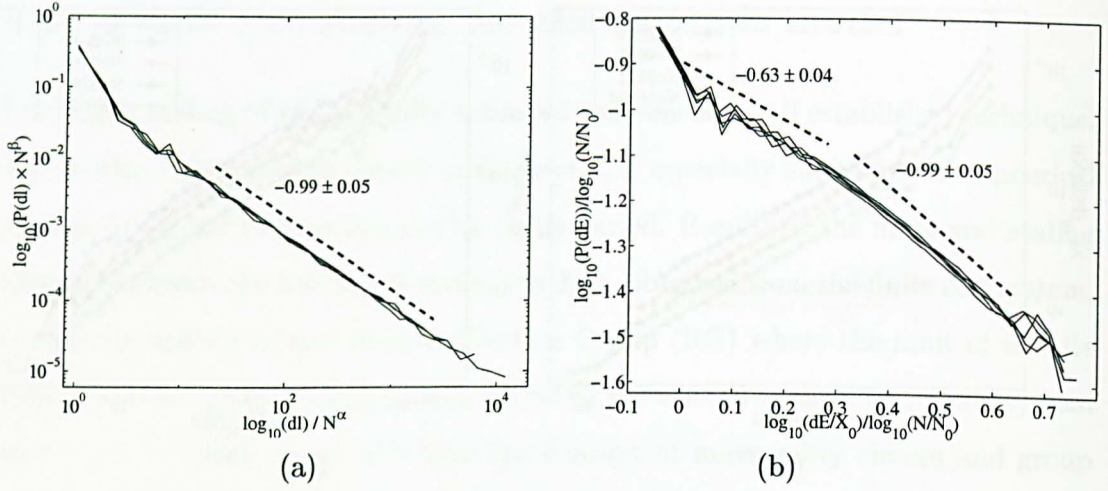


Figure 4.2: Finite size scaling of the avalanche lengths PDIFs (a) and dissipated energy PDIFs (b). Parameter  $L_f = N$  and 2% randomization of the critical gradient was added.

scaling of  $\alpha_1^{dE} = -0.99 \pm 0.05$  and can be well approximated by the second index  $\alpha_2^{dE} = -0.63 \pm 0.04$ . The analysis indicates that the transition point between small and large events regime of the dissipated energy PDIFs also scales with the system's size and, in the graph of the rescaled distributions, it collapses onto the single point. This is a new result that could not be addressed previously by applying RG analysis. As it was already mentioned, the small scale regime is not relevant from the universality point of view as the small events dynamics is model dependent. Indeed, the distribution of small avalanches is dramatically affected by the added stochastic part of the critical gradient and changes with the driving rate. The behavior of the small avalanches is of interest when applying the sandpile to model a particular physical phenomena, where finite size must be assumed from the outset. *Chapman et al.* (1999) used this sandpile model to investigate the dual scaling of the dissipated energy in the substorms of the Earth's magnetosphere. In the same, work it was pointed out that the finite size effects, such as appearance of the mean dissipated energy for the largest events, are also of importance for developing realistic models of the physical systems.

The apparent ubiquity of the critical systems in nature rises an interesting and challenging question: Can criticality be quantified through the observation of

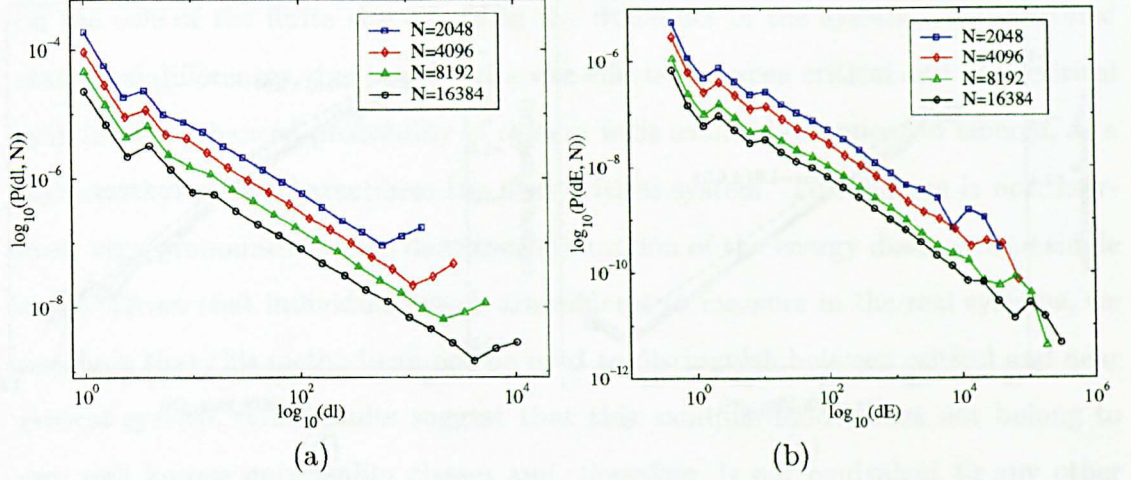


Figure 4.3: PDIFs of the avalanche lengths (a) and dissipated energy (b) for different system's sizes  $N$ ,  $L_f = N/2$  and 2% randomization of the critical gradient.

physical system and data analysis? To address that question, we will now investigate a finite size scaling of the sandpile for the parameter  $L_f < N$ . In this case the system is away from its fixed point and thus is not critical. The challenge lies in quantifying the proximity of the sandpile to its fixed point. If existing statistical methods can not detect the departure of the system from its fixed point then many observed systems, that exhibit power laws and fractal patterns, may not be, strictly speaking, in the critical state.

Figure 4.3(a,b) shows the probability distribution functions for the avalanche lengths and dissipated energy observed in the sandpile model with varied length  $N$ ,  $L_f = N/2$  and 2% randomization of the critical gradient. It is immediately clear that the finite size effects are more pronounced in this mode. This applies especially to the PDIFs of avalanche lengths, which for  $L_f = N$  exhibited nearly perfect length invariance (see figure 4.2(a)). Now, with the departure of the system from the critical regime, the probability of the system size events increases visibly. In the case of the dissipated energy PDIFs, the changes are less visible. In fact, without closer analysis, the dissipated energy PDIFs for  $L_f = N$  and  $L_f = N/2$  could be taken as identical. Figure 4.4(a,b) shows the collapse of the PDIFs for both observable after the multi-fractal ansatz (2.38) was applied. Fitting parameters were taken as  $N_0 = 1.0$ ,  $X_0 = 0.2$  for avalanche lengths and  $N_0 = 0.004$ ,  $X_0 = 1.0$



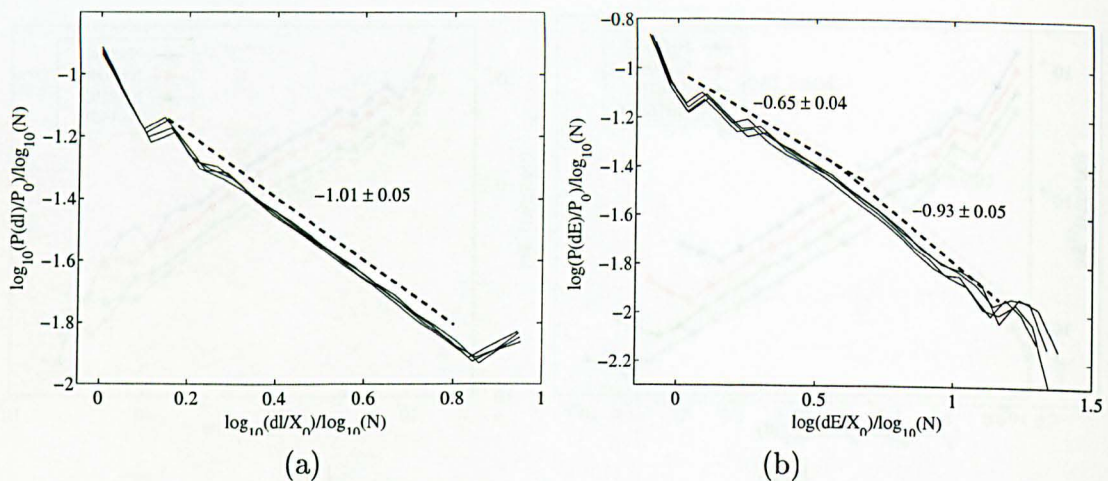


Figure 4.4: Finite size scaling of PDIFs for avalanche lengths (a) and dissipated energy (b) for different system's sizes  $N$ ,  $L_f = N/2$  and 2% randomization of the critical gradient.

for the dissipated energy PDIFs. In this case, neither ordinary scaling nor multi-index approach gave a satisfactory collapse for the large and small scale events. This apparent multi-fractal character of the avalanche length distribution could be, however, misleading. It is clear, from the features of the rescaled PDIFs, that mono-scaling statistics is still dominant on the large number of scales. For these scales, the power law index  $\alpha^{dl} = -1.01 \pm 0.05$  is identical to that obtained from the system with  $L_f = N$ . Multi-fractality appears as a result of the increased probability of avalanches with  $dl > L_f$ . Dissipated energy exhibits higher sensitivity to the departure of the system from its critical regime. The small events scaling, corresponding to the index value of  $\alpha_2^{dE} = -0.65 \pm 0.04$  now extends further towards the large scale events. The dual scaling, observed for  $L_f = N$ , does not provide a good description of the scaling in this case. We observe a smooth transition of the scaling index from the initial value of  $-0.65$  towards  $\alpha_1^{dE} = -0.93 \pm 0.05$  predicted for the large events. Similarly to the case of  $L_f = N$ , the largest  $dE$  events exhibit a clear departure from the power law distribution with the average events size being well defined.

The finite size scaling approach presented here allowed us to study the differences in scaling between systems with varied parameter  $L_f$ . Our results shed light

on the role of the finite size effects in the dynamics of the system. We identified statistical differences, due to the finite size effects, between critical and near critical system. An enhanced probability of system wide avalanches appear to emerge, as a feature, that could characterize the near critical system. This feature is not, however, very pronounced in the distribution function of the energy dissipated in single event. Given that individual events are difficult to measure in the real systems, we conclude that this method can not be used to distinguish between critical and near critical system. Our results suggest that this sandpile model does not belong to any well known universality classes and, therefore, is not equivalent to any other sandpile model.

## 4.2 Self-similarity and length scaling of the time series

An accurate determination of the self-similarity (or self-affinity) exponents is of crucial importance for the theory of critical systems such as SOC sandpile models. Many possible variations of the sandpile algorithm exists but their emergent fundamental features, such as the power law scaling index, are often identical. This universality allows us to focus on the few distinct phenomena, rather than studying all possible sandpile algorithms. Calculation of the fractal dimension allows us to estimate the self-affinity of the time series and characterize the system. In Chapter 2, we introduced a divider or length scaling method and in this section we will use it to obtain the fractal dimension of time series collected from the sandpile model. We start with the analytical estimation of the fractal dimension for the critical model ( $L_f = N$ ) with no randomness. Consider the time series  $E(t)$  for the sandpile with a constant threshold  $g_c$  and the parameter  $L_f$  equal to the length of the grid. We will show, analytically, that the energy curve  $E(t)$  (see 4.5) has a fractal capacity dimension of 1. Figure 4.5(b) shows how this curve may be reconstructed using successive midpoint divisions. Since the avalanches are instantaneous, all vertical segments are perpendicular to the time axis. We also know the length of each vertical segments



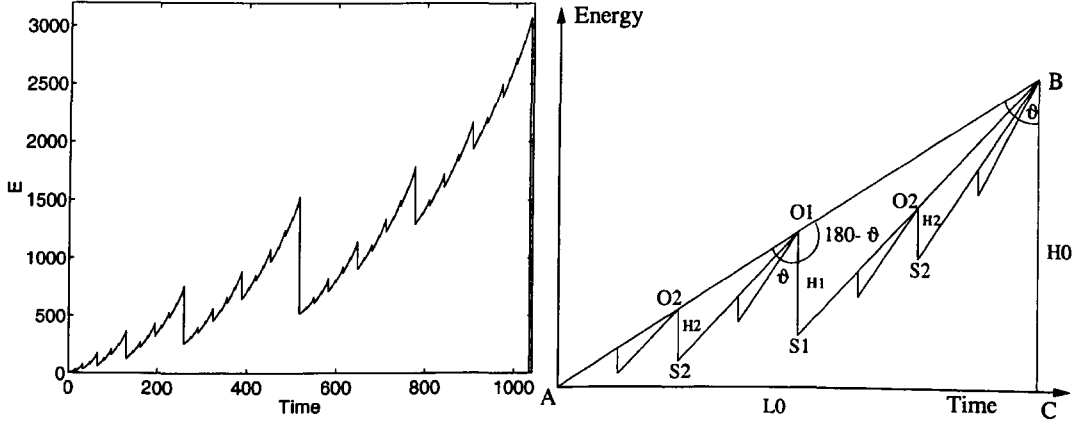


Figure 4.5: (a): The total energy of the sandpile in the stationary state. System Length  $N = L_f = 4096$ , no noise present. (b): Midpoint division used to reconstruct the energy time series.

from the analytical solution by *Helander et al.* (1999):

$$H_1 = H_0/3 \quad \text{and} \quad H_n = H_{n-1}/2 \quad \text{for all } n > 1. \quad (4.2)$$

We start with a triangle  $ABC$ . The length of the curve is then equal to the length of the hypotenuse. Next, we draw a vertical segment from the midpoint of the hypotenuse and connect the lower end  $S_1$  with point  $B$ . The length of the vertical segment should be  $H_1 = H_0/3$ . The total length of the curve is now a sum of the segments  $AO_1$ ,  $O_1S_1$  and  $S_1B$  and can be expressed as:

$$P_1 = H_0 \left( \frac{1}{3} + \frac{1}{2} \sqrt{R^2 + 1} + \frac{5}{6} \sqrt{\left(\frac{3R}{5}\right)^2 + 1} \right), \quad (4.3)$$

where  $H_0$  is the length of the first vertical segment and  $R$  is a ratio of  $L_0/H_0$ . Now, we add two vertical segments in the midpoints of the segment  $AO_1$  and  $S_1B$ . Their length, given by (4.2), are  $H_2 = H_1/2$ . After 3 steps, the combined length of the curve can be written as:

$$P_3 = \frac{H_0}{3} \left[ 3 + \frac{3}{8} \left( \sqrt{R^2 + 1} + 15 \sqrt{\left(\frac{3R}{5}\right)^2 + 1} + 21 \sqrt{\left(\frac{3R}{7}\right)^2 + 1} + 9 \sqrt{\left(\frac{3R}{9}\right)^2 + 1} \right) \right] \quad (4.4)$$

If one carries on this procedure, the energy time series can be obtained with any given accuracy. Closer examination of terms in (4.4) reveals that the total length of

the curve after  $n$ -th division can be written as:

$$S_n = \frac{H_0}{3} \left( n + \frac{1}{2^{n-1}} \sqrt{1 + R^2} + \frac{1}{2^n} \sum_{j=0}^n C_j^n (2j + 3) \sqrt{1 + \left( \frac{3R}{2j + 3} \right)^2} \right), \quad (4.5)$$

where binomial coefficients  $C_j^n$  are given by:

$$C_j^n = \frac{n!}{k!(n - k)!}. \quad (4.6)$$

If we normalize maximum time to be 1 ( $H_0 = 3$ ) then the ratio  $R$  will have a value of  $1/3$ . Applying this in the above formula and assuming  $2j + 3 \gg 1$  we can perform the summation in equation (4.5):

$$\sum_{j=0}^n C_j^n (2j + 3) = 2 \sum_{j=0}^n j C_j^n + 3 \sum_{j=0}^n C_j^n = 2^n (n + 3) \quad (4.7)$$

The second term in (4.5),  $\frac{1}{2^{n-1}} \sqrt{1 + R^2}$ , can be neglected for large values of  $n$ . The final expression for the  $S_n$  can then be reduced to  $S_n = 2n + 3$ . To obtain the fractal dimension, one needs to find the ratio:

$$D = \lim_{n \rightarrow \infty} \frac{\ln(S_n)}{\ln(n)} = \lim_{n \rightarrow \infty} \frac{\ln(2n + 3)}{\ln(n)} \quad (4.8)$$

Clearly, this ratio will converge to 1 for  $n$  approaching infinity. The result highlights an interesting aspect of the fractal dimension estimation, from the finite size sample and with instrumental or physical threshold. The analytical result given by (4.8) is obtained in the limit of the infinite experimental resolution, i.e., when all the relevant scales are present. As we can see in the figure 4.6, however, the fractal dimension  $D(n)$  of the curve for a given  $n$  is well above 1 even for quite large values of  $n$ . This suggests that the fractal dimension, calculated by length measurement of the experimentally observed time series, could, in principle, yield a nontrivial but incorrect fractal dimension  $D(n) > 1$ .

The length scaling was also investigated, numerically, for the different values of the control parameter  $L_f$ . Figure 4.7 shows time series corresponding to three selected values of the  $L_f$  parameter and constant (plates (a),(b),(c)) as well as the randomized (plates (d),(e),(f)) critical gradient. The results of the curve length analysis are shown in figures 4.8. In the case of  $L_f = N$ , added fluctuations of the

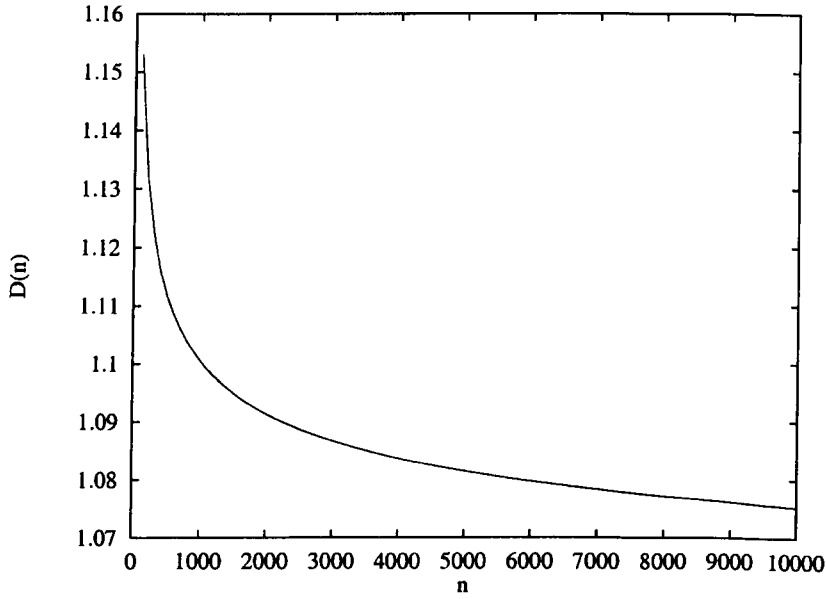


Figure 4.6: Fractal dimension estimation for the energy time series obtained through the successive midpoint division.

critical gradient (up to 2%) did not change the scaling properties of the system. The time series curve is still self-similar. The fractal dimension of 1 can be concluded from the slope of the line. The scaling curve for  $L_f = N/2$  looks very similar. It is clear that the length of the curve scaling can not be used to differentiate between the critical and near critical case. This is also true for the randomized critical gradient where the slopes of the scaling curves are identical. As the  $L_f$  parameter decreases, long avalanches become more probable and their probability distribution is no longer a power law with index  $-1$ . The distribution of the small events is unchanged (for example see Figures 12 and 13 in *Chapman (2000)*). This should give rise to a kink, which indeed can be observed in the scaling curves. The existence of the kink and its location on the scaling curves are consistent with the scale breaking in the probability distribution of the avalanche length in the given region (*Chapman et al., 1999*). This ability of scaling curves to recover features present in the probability distribution suggests that the curve length estimation could be used as an alternative to probability distributions of events. In the case, of the time series from real physical systems the individual events are often convoluted

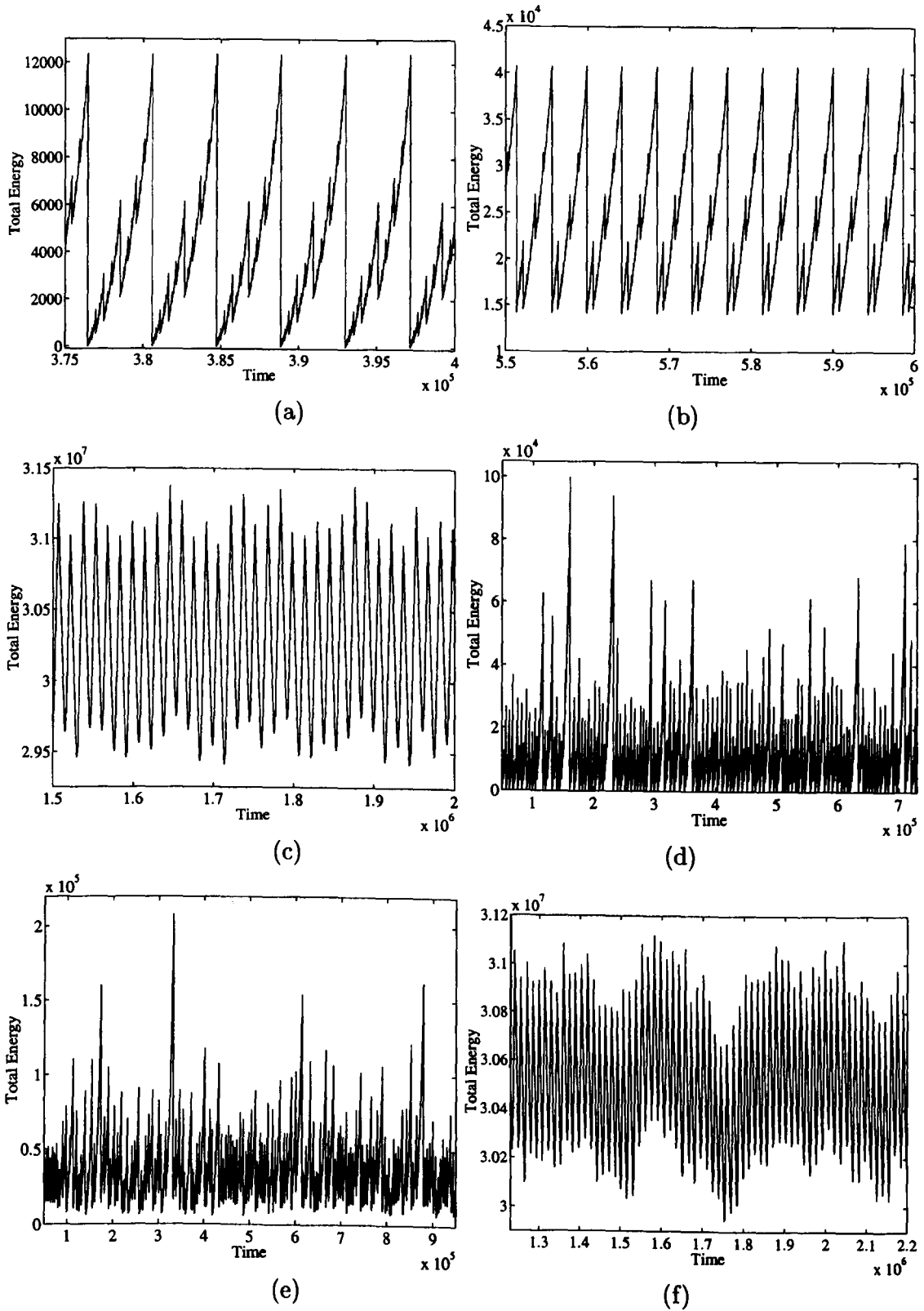


Figure 4.7: (a): Total energy time series for the sandpile with length  $N = 4096$ . (a)  $L_f = N$ , constant critical gradient, (b):  $L_f = N/2$ , constant critical gradient, (c):  $L_f = 48$ , constant critical gradient, (d)  $L_f = N$ , randomized critical gradient, (e):  $L_f = N/2$ , randomized critical gradient, (f):  $L_f = 48$ , randomized critical gradient.

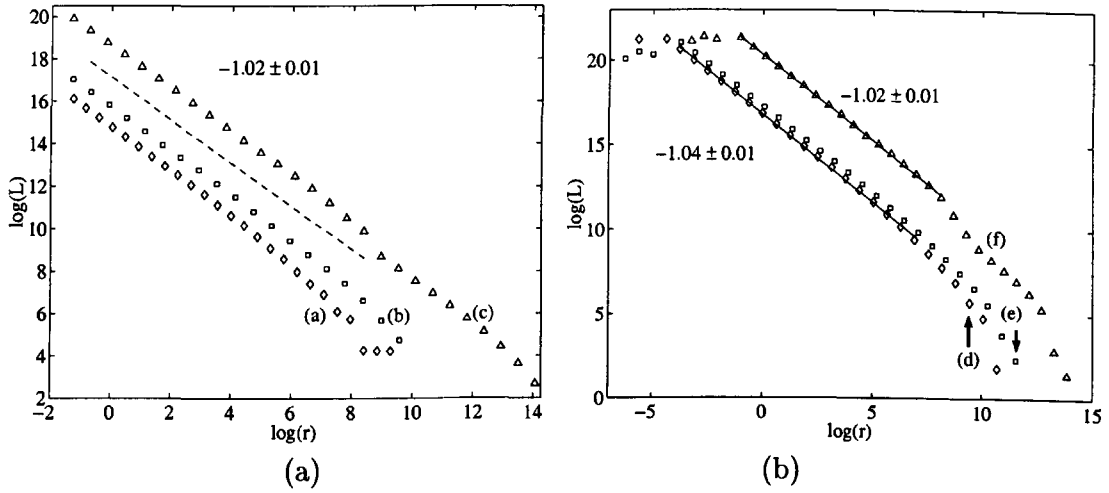


Figure 4.8: Curve length scaling for the energy time series with (a) constant and (b) randomized critical gradients. Letters identify corresponding plates in the figure 4.7.

with sampling and contaminated with other signals. In such scenarios, these events are hard to identify and methods that are less sensitive to external fluctuations are highly desirable.

### 4.3 Phase Space Reconstruction

Let us now turn our attention toward the phase space representation of the system's dynamics. The phase space plots, shown in the figure 4.9, indicate that, when away from the fixed point, a low-dimensional structure emerges. Before the fractal dimension can be estimated from the time series, a phase space reconstruction process needs to be applied to identify the right embedding dimension for the problem (as described in the Section 2.3.2). As the higher order fractal dimension are more sensitive to the scale breaking, we will present our results using correlation dimension. These curves show a local slope of the correlation sum (2.45) computed for the given range of scales  $\epsilon = 1/r$  and different embedding dimensions. If, for all embedding dimensions larger than a minimal one, these curves collapse onto each other and the clear plateau can be found then the correlation dimension is estimated directly as a value of that plateau. The general behavior of the scaling curves is well understood. For the small values of  $r$ , the stochastic part of the dynamics dominates

and the curves diverge and the slope of the correlation sum is proportional to the embedding dimension. For the large values of  $\tau$ , the slope changes again as the edge of the attractor is approached. To eliminate pairs that are close in distance, due to residual time correlation and not their true position in the phase space, space-time plots were used. This technique allows us to determine the maximum window needed for the numerical search of the near neighbors. The optimal maximum window was found to correspond to the value of the parameter  $L_f$  and we used this value in all computations.

#### 4.3.1 Constant critical gradient

We start our analysis with the constant critical gradient model. The selection of the time delay  $\tau$  for the phase space reconstruction is crucial (*Kantz and Schreiber, 1997*). In *Fraser and Swinney (1986)*, a method was proposed for finding an optimal value of the delay parameter by using the first minimum of the mutual information. Figures 4.10–4.12(a) show the mutual information curves calculated for three different values of the control parameter  $L_f$ . The arrows indicate the time delay chosen for each case. We note that the term “first minimum” may be misleading as one needs to assure that all relevant physical scales are included in the reconstructed vectors. In many cases, similarly to one presented here, small minima occurring early in the mutual information curve must be omitted in order to include these scales. The arrows on the the mutual information figures indicate values of the delay  $\tau = 1024, 512, 15$  for parameters  $L_f = N, N/2$  and  $\sim (N/90) = 48$  respectively. Figure 4.7(a) show the time series of the total energy of the sandpile for control parameter  $L_f = N$  and no randomization. Corresponding phase space structure, shown in figure 4.9(a), consists of  $\log_2(N)$  linear structures with point density in each segment decreasing with the dissipated energy. Panel (a) of the figure 4.10 shows the mutual information  $I_m$ . Similarly to the energy time series under investigation, it also exhibits a self-similar character. As mentioned before, the delay parameter was chosen so that all relevant scales contribute to the correlation sum algorithm. Finally, panel (b) shows the local slope of the correlation sum computed

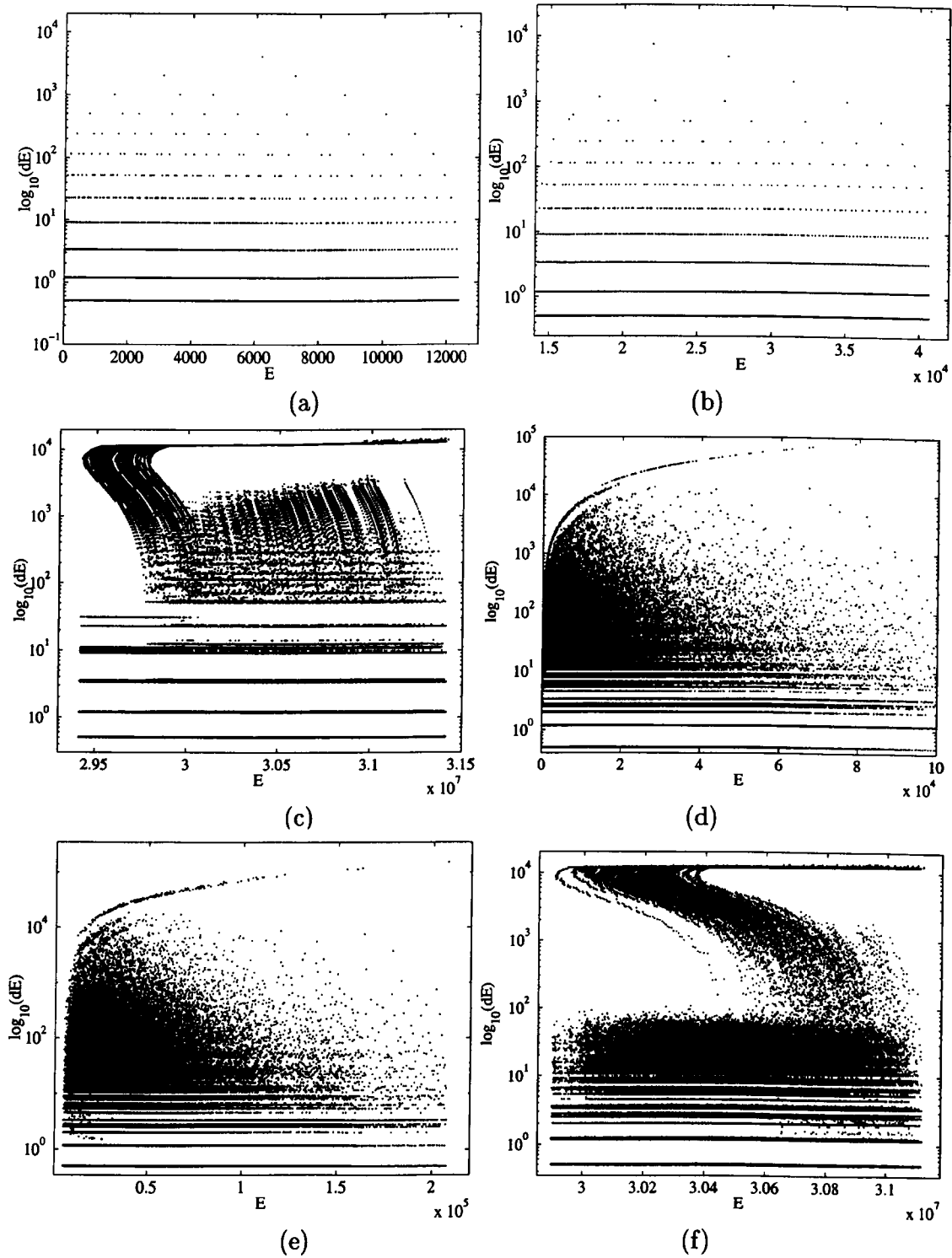


Figure 4.9: Phase space structures. Parameters for each plate correspond to these in the figure 4.7.

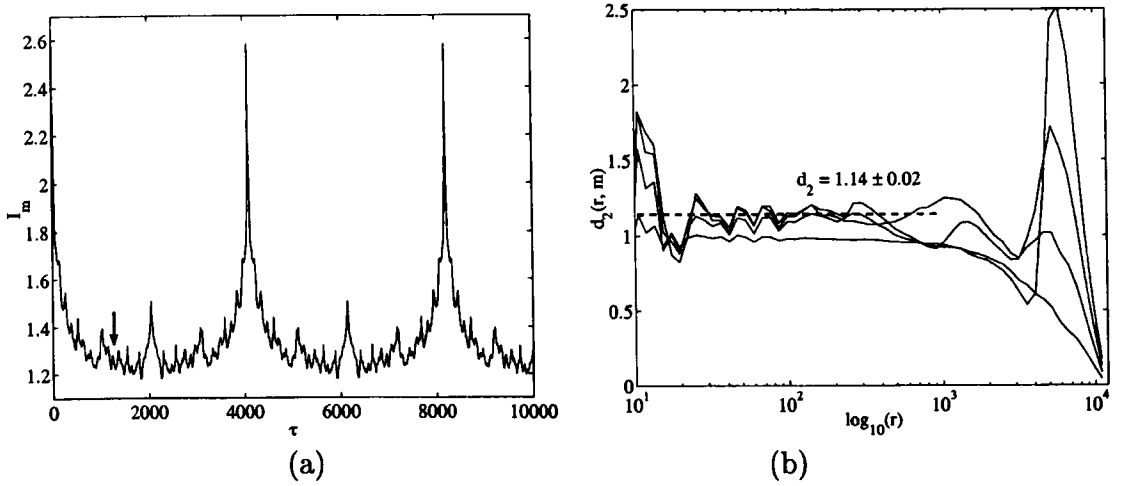


Figure 4.10: Mutual information (a) and the local slope of the correlation sum curve (b). Dashed line represented the estimation of the correlation dimension. System parameters:  $N = 4096$ ,  $L_f = N$  and constant critical gradient.

for the embedding dimensions 1 to 10 and the delay parameters found above. A low correlation dimension  $d_2 = 1.14 \pm 0.02$  found for this parameter range is consistent with the phase space structure shown in figure 4.9(a). We note the excellent convergence of the curves for all embedding dimensions larger then 4.

Figures 4.11(a,b) show the mutual information and the correlation dimension estimates for the control parameter  $L_f = N/2$ . It is immediately clear that the time series (see figure 4.7(b)) and the phase space structure (see figure 4.9(b)) are very similar to these found in the previous case. Both consist of linear segments spaced evenly on the logarithmic scale. This indicates that the system's dynamics is influenced by the fixed point for the large range of the  $L_f$  parameter values. We find the correlation dimension  $d_2 = 1.05 \pm 0.01$ . This estimate is quite different from that found for  $L_f = N$  and the errors are small. The estimate, however, is based only on the slopes of correlation sum extending over about one decade.

A visual inspection of the energy curves presented before, clearly shows the change in system's dynamics for  $L_f = 48$  (see figure 4.7(c)). We now attempt to detect this change using phase space reconstruction. For the low values of  $L_f$ , the system exhibits many features reminiscent of low dimensional chaos, such as, period doubling and intermittency (*Chapman, 2000*). This dynamical region can be



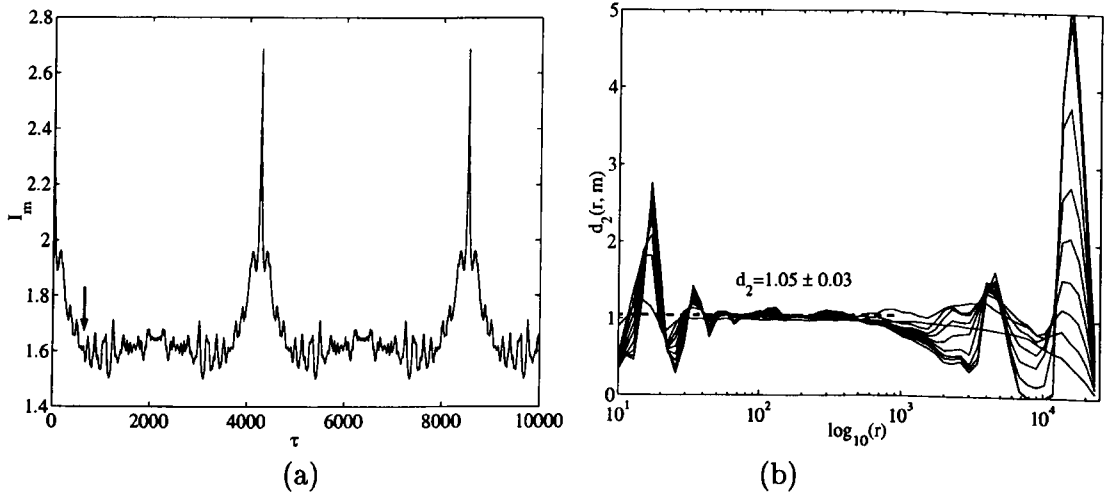


Figure 4.11: Mutual information (a) and the local slope of the correlation sum curve (b). Dashed line represented the estimation of the correlation dimension. System parameters:  $N = 4096$ ,  $L_f = N/2$  and constant critical gradient.

associated with increased probability of the long events, the increased importance of the system interaction with the open boundary and the separation of the small and large scale dynamics. Phase space structure, generated by plotting the total energy of the sandpile against the energy dissipated in the single event, shows the low dimensional structure that is formed between the values of  $10^2$ – $10^4$  of the dissipated energy (see figure 4.9(c)). Clear periodicity of the signal (see figure 4.7(c)) of the total energy can also be observed. Figure 4.12 shows the mutual information and the  $d_2$  estimates for the given parameters. The first minimum of the mutual information occurs for the time delay of  $\sim 20$ , as shown in the insert of the figure 4.12(a). A nontrivial correlation dimension,  $d_2 = 1.33 \pm 0.02$ , can be then obtained from the figure 4.12(b). The plateau extends only throughout the parabolic structure of the phase space structure. The results strongly suggest that two distinct regimes influence system's dynamics. First regime, dominant on small scales, is identical to that found for  $L_f = N$ . The phase space graph 4.9(c) shows linear segments for energy releases up to  $dE \approx 50$ . Large events, with energy dissipated being above 50, are governed by a different, more structured process.

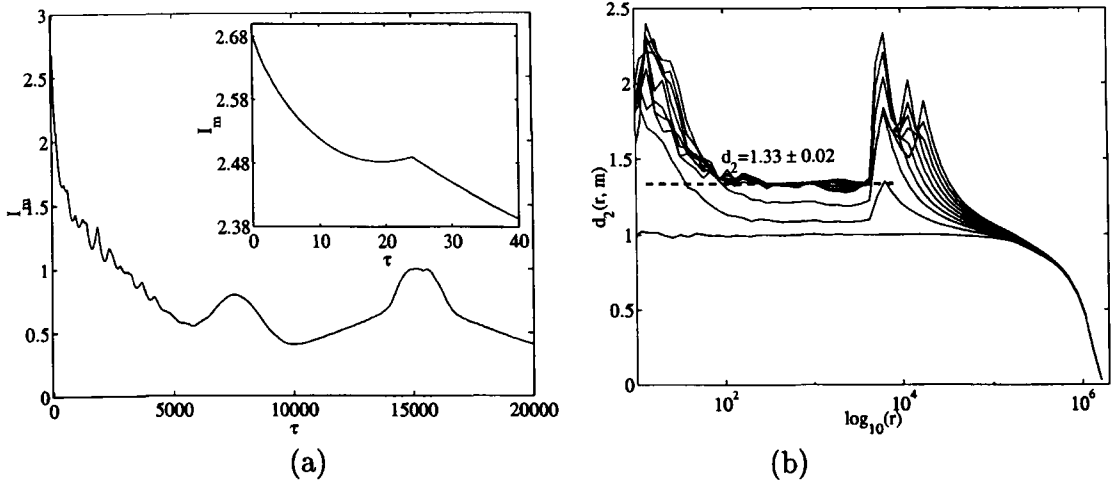


Figure 4.12: Mutual information (a) and the local slope of the correlation sum curve (b). Dashed line represented the estimation of the correlation dimension. System parameters:  $N = 4096$ ,  $L_f = 48$  and constant critical gradient.

#### 4.3.2 Randomized critical gradient

We now turn our attention toward the case with randomized critical gradient. The data will now much more closely resemble an experimental time series where the noise is an omnipresent phenomenon and can not be neglected. It has been shown empirically that the maximal tolerable noise level, for which the correlation dimension of the chaotic system can be estimated, is about 2% (*Kantz and Schreiber, 1997*). We will apply 2% noise level of the critical gradient to simulate such real experimental time series. Figures 4.7(d,e,f) and 4.9(d,e,f) show the energy time series and phase space graphs for the same values of the parameter  $L_f$  as previously, i.e.,  $L_f = N$ ,  $L_f = N/2$  and  $L_f = 48$ . The dynamics in the critical and near critical regimes is affected significantly by fluctuations of the critical gradient. The low-dimensional regime, however, is still dominated by the periodic oscillations. Figures 4.13(a,b) show the mutual information and the estimate of the slope of the correlation sum for  $L_f = N$  and randomized critical gradient respectively. The mutual information changes dramatically even for this, relatively low, level of added fluctuations. Its self-similar nature is no longer observed. We find the first, well pronounced, minimum at  $\tau \approx 1.36 \times 10^4$  and this will be the value of the delay parameter used for the phase space reconstruction process. Interestingly, the scaling

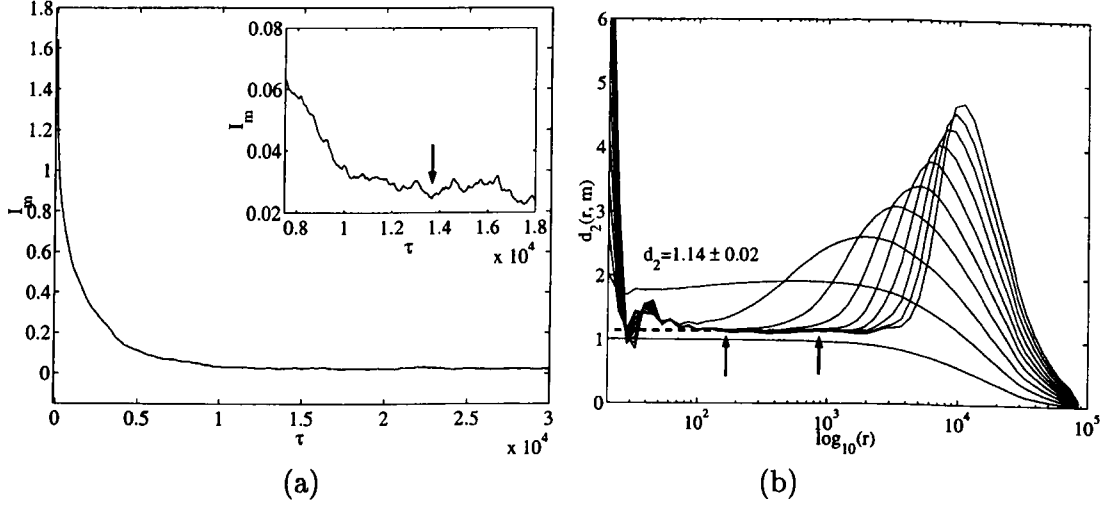


Figure 4.13: Mutual information (a) and the local slope of the correlation sum curve (b). Dashed line represented the estimation of the correlation dimension. System parameters:  $N = 4096$ ,  $L_f = N$  and 2% randomization of the critical gradient.

improves when the randomization of the critical gradient is included in the model. Added fluctuations allow the system dynamics to explore the larger area of the phase space. This is in contrast with the chaotic systems where the noise “spreads” the attractor and destroys the scaling. The estimated value of the correlation dimension is  $d_2 = 1.14 \pm 0.02$ , identical to that found for  $L_f = N$  and constant critical gradient. The different response of the system to the added noise, could be in principle used to distinguish between critical and near critical dynamics. In practise, however, one does not control the level of noise in the observed system and the use of this method is rather limited. Once again, we attempt to quantify the system’s proximity to its critical state. We will test if the difference between a critical and a near critical system could be identified through the phase space reconstruction. We repeat the procedure for the dynamical parameter  $L_f = N/2$  and 2% fluctuations of the critical gradient. As before, the mutual information, shown in figure 4.14(a), has lost its self-similar features. The scaling found through the correlation sum algorithm is even more similar to that of  $L_f = N$  now that the randomization is present. A slight difference between obtained estimated correlation dimensions is too small to quantify the difference between these two cases. Our estimate of the correlation dimension is  $d_2 = 1.10 \pm 0.02$ . We conclude that the correlation

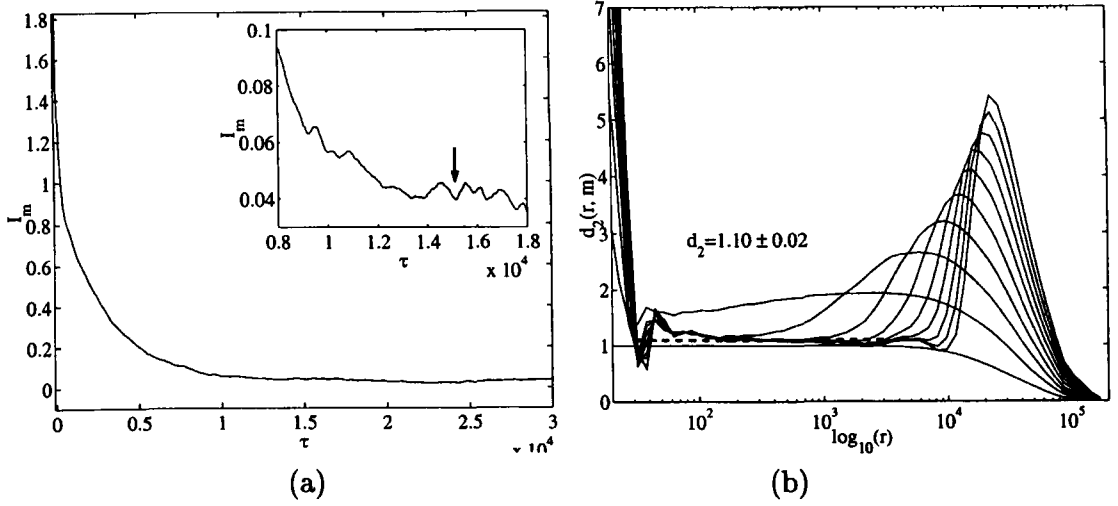


Figure 4.14: Mutual information (a) and the local slope of the correlation sum curve (b). Dashed line represented the estimation of the correlation dimension. System parameters:  $N = 4096$ ,  $L_f = N/2$  and 2% randomization of the critical gradient.

dimension is identical, to within errors, for  $L_f = N$  and  $L_f = N/2$ . Decreasing the value of  $L_f$  we approach the dynamical region where a low-dimensional structure in the phase space can be clearly identified. Figure 4.15(a), the mutual information curve, shows clear periodicity present in the signal. The insert of this figure shows that the first minimum occurs for  $\tau \approx 22$  and we used that value as the time delay parameter in the reconstruction process. The figure 4.15(b) clearly shows that the scaling of the parabolic structure, that was found in the non randomized model, is now absent. Two sharp peaks, marked on the figure with arrows, indicate the edges of the attractor corresponding to dissipated energy between  $\simeq 2 \times 10^2$  and  $\simeq 8 \times 10^3$ . These peaks mark the transition regions between linear segments and the parabolic structure on the phase space graph 4.9(f).

This analysis was repeated for various values of the time delay parameter  $\tau$  to confirm that our results are not sensitive to the small changes in the reconstruction procedure. We also attempted to use the first visible minimum of the mutual information shown in 4.15 (a) and corresponding to  $\tau \approx 1.1 \times 10^4$ . No single scaling was found in that case, however.

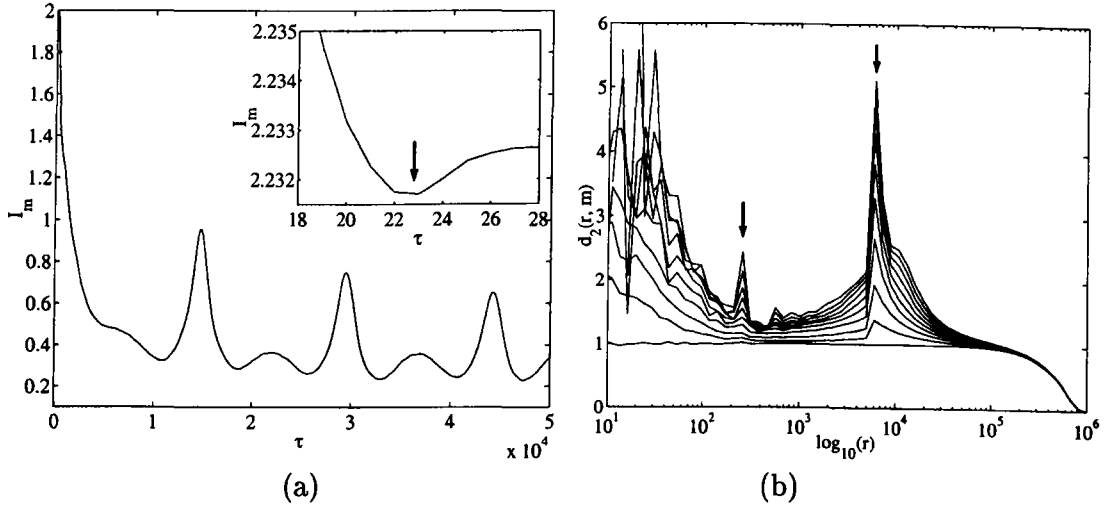


Figure 4.15: Mutual information (a) and the local slope of the correlation sum curve (b). Dashed line represented the estimation of the correlation dimension. System parameters:  $N = 4096$ ,  $L_f = 48$  and 2% randomization of the critical gradient.

## 4.4 Conclusions

Certain statistical features of the times series are being invoked as evidence for SOC. It is important to know whether it is possible to determine, from the time series alone, whether a system is precisely at the fixed point or not. Results of the higher order nonlinear fractal analysis presented in this chapter indicate that:

- The scaling of the critical and near critical system's dynamics can be obtained from the finite size data set, using correlation dimension estimation. The results can not, however, quantify the proximity of the system to its fixed point.
- In the case of non critical system with noise present, the scaling may not be possible to detect. The scale separation can, however, be identify with the aim of the phase space graphs.

The fact that the near critical system can exhibit statistical features characteristic of SOC raises an important question about the role of the criticality in the observed systems. Our inability to distinguish between the critical and near critical system, even with sophisticated non linear analysis, highlights the underlying difficulty in

understanding the common character of SOC. The fact that the system does not need to be precisely at the fixed point to show SOC phenomenology, combined with the results presented in here, may offer a simple explanation for the apparent ubiquity of SOC in nature.

## Chapter 5

# Modeling tokamak plasmas with the Sandpile Model

There is growing interest in relating the observed characteristics of energy transport in both astrophysical and laboratory plasmas to sandpile models that dissipate energy by means of avalanches. The empirical features of a sandpile, for example the scaling of its profile and energy storage capacity with model parameters, may display significant parallels with those of complex plasma systems. In a fusion experiment, parameters such as the turbulent correlation length depend in a complicated, and in many cases unknown, way on a hierarchy of nonlinear, coupled and multi-scale plasma physics processes. The sandpile approach is motivated by the hypothesis that fusion plasmas are complex systems, exhibiting self organization and perhaps SOC. This is well supported by observations of rapid, nonlocal and non diffusive energy transport events in tokamaks (*Carreras and Newman, 1996; Dendy and Helander, 1997*) and large scale numerical simulations (*Garbet and Waltz, 1998; Sarazin and Ghendrih, 1998*). In this chapter, we will discuss significant qualitative parallels between aspects of the observed phenomenology of magnetic fusion plasma confinement systems and the analogous outputs of the model with variable  $L_f$ . Our results strongly suggest that this unity may extend to some of the most distinctive features of toroidal magnetic plasma confinement: enhanced confinement

regimes (“H modes”), edge localized modes (“ELMs”), steep edge gradients (“edge pedestal”) and their observed phenomenological and statistical correlations (*Zhang et al.*, 1998; *Fishpool*, 1998; *Hugill*, 2000). High confinement transport regime, or “H mode”, is a most developed mode of high confinement tokamak operation. Its defining feature is a reduction in transport near the edge of plasma. This leads to the appearance of the steep gradients in temperature and pressure near the edge. These are often referred to as edge pedestals. The high confinement regime is accompanied by edge localized modes (ELMs). ELMs are periodic rapid energy and particle loss events which are restricted, again, to the region near the plasma boundary. An important question is whether the low confinement mode (“L mode”) to H-mode transition necessarily reflects a catastrophic bifurcation of confinement properties or can be associated with a monotonic change in the character of the turbulence (*Hugill*, 2000).

## 5.1 Tokamak-like enhanced confinement phenomenology from the sandpile model

Transitional behavior, resembling that observed in fusion plasmas, has been found in the sandpile algorithms before. For example, *Carreras and Newman* (1996) studied a sandpile with an imposed local sheared flow region which reduces the characteristic avalanche length, thereby affecting confinement. In *Carreras et al.* (1998), changes in the redistribution rule lead to changes in profile stiffness. We will show that key elements of the observed phenomenology emerge naturally from a simple one-dimensional sandpile model, that introduced in Chapter 2. This model’s distinctive algorithmic feature relates to the length scale  $L_f$ , over which the most rapid redistribution occurs. In a context of plasma systems, this could be considered a proxy for turbulent correlation length or eddy size. In *Chapman* (2000) the sandpile is explored for all regimes  $1 < L_f \leq N$  for both constant and fluctuating critical gradient  $g_c$ . We consider the dynamics of the more realistic case with random fluctuations in  $g_c$ . The behavior of the sandpile is essentially insensitive to both the level and



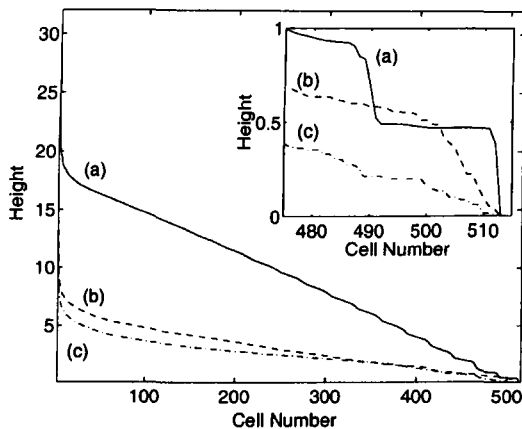


Figure 5.1: Time averaged height profiles of the 512 cell sandpile for  $L_f =$  (a) 50, (b) 150, and (c) 250. Inset: edge structure.

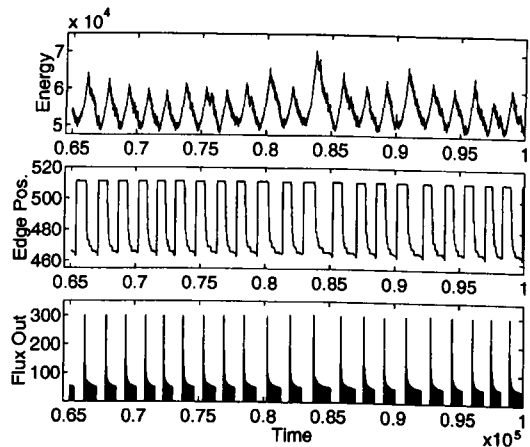


Figure 5.2: Time evolution of the 512 cell sandpile with  $L_f = 50$ : (top) stored energy; (middle) position of last occupied cell; (lower) magnitude and occurrence of mass loss events.

spectral properties of these random fluctuations (*Chapman, 2000; Chapman et al., 1999*). In the limit  $L_f = N$ , where  $N$  is the number of cells in the grid, the sandpile is flattened everywhere behind an unstable cell. A real space RG approach (*Tam et al., 1999*) shows that the robust and scale free dynamics, for the limiting case  $L_f = N$ , corresponds to a nontrivial (repulsive) fixed point. The essential result, reported in *Chapman (2000)* is that different regimes of avalanche statistics emerge, resembling a transition from regular to intermittent dynamics reminiscent of deterministic chaos. The control parameter is the normalized redistribution scale length  $L_f$  which specifies whether the system is close to the nontrivial  $L_f = N$  fixed point.

Height profiles for the sandpile with 512 cells, time averaged over many thousands of avalanches, are shown in 5.1 for three different values of the fluidization length  $L_f$  in the range  $50 \leq L_f \leq 250$ . The sandpile profile shape, stored gravitational potential energy and edge structure (smooth decline or pedestal) correlate with each other and with  $L_f$ . As  $L_f$  is reduced, the edge pedestal steepens and the time averaged stored energy rises. Multiple barriers (regions of steep gradient) appear in trace (a) and to some extent trace (b) of figure 5.1. Time evolution of the sandpile for  $L_f = 50, 150$ , and  $250$ , respectively, is quantified in figures 5.2-5.4. The top traces show total stored energy, the middle traces show the position of

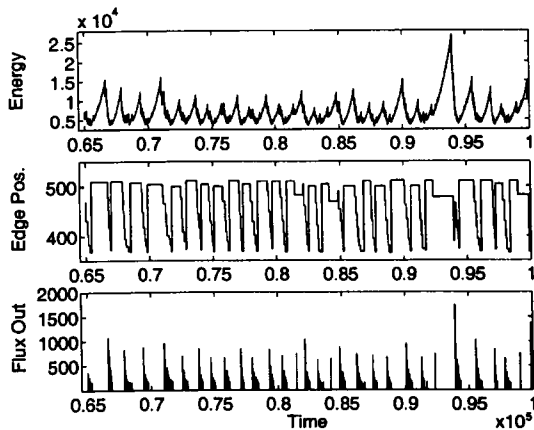


Figure 5.3: As in figure 5.2, for  $L_f = 150$ .

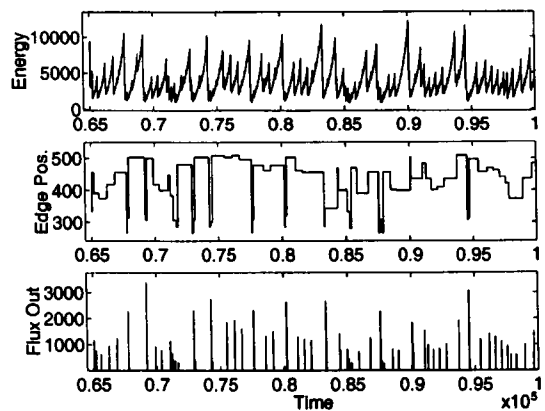


Figure 5.4: As in figure 5.2, for  $L_f = 250$ .

the edge of the sandpile (the last occupied cell) and the bottom traces show the magnitude and occurrence times of mass loss events (hereafter MLEs). During each MLE the sand is lost from the system by being transferred beyond the 512th cell. Time is normalized to the mean inter-avalanche time  $\Delta\tau$  and is proportional to the fueling rate. The sandpile is fueled only at the first cell, so that the great majority of avalanches terminate before reaching the 512th cell. These are classified as internal. While internal avalanches result in energy dissipation and may alter the position of the edge of the sandpile, they do not result in an MLE. Visible periods of quiescence in the middle and lower traces of figures 5.2-5.4 are associated with this lack of MLEs. Conversely, the MLEs are associated with sudden inward movement of the sandpile edge and in this important sense, appear to be edge localized. However, MLEs and the associated inward edge movement are, in fact, the result of systemwide avalanches triggered at the sandpile center (cell  $n = 1$ ). The character of the MLEs changes with  $L_f$ . In the figure 5.2, where the mean and peak stored energy are greatest, the MLEs are similar to each other and occur with some regularity. The regularity of MLE occurrence in figure 5.3 is less marked, the magnitude of the largest MLEs is greater than in figure 5.2 and there is greater spread in MLE size. This trend continues in figure 5.4, which also has the lowest stored energy. These effects correlate with the underlying dynamics of the sandpile. Figure 2.7, discussed in Chapter 2, plots the relation between average stored energy

and  $L_f$  for the  $N = 512$  system and much larger  $N = 4096$  and  $N = 8192$  systems (normalized to the system size  $N$ ). The curves coincide, demonstrating invariance with respect to system size, with an inverse power law with slope close to  $-2$  for  $L_f/N < 1/4$ , and a break at  $L_f \approx 1/4$ . These two regimes yield the quasi-regular and quasi-intermittent dynamics in figures 5.2-5.4 (see also the plot of avalanche length distribution against  $L_f$  in figure 8 of reference *Chapman (2000)*). The parameter  $L_f$  is a measure of proximity of this high dimensional system to the  $L_f = N$  nontrivial fixed point. This determines both the apparent complexity of the time series in figures 5.2-5.4 and the underlying statistical simplicity described below, which is also invariant with respect to system size.

There is systematic correlation between time averaged stored energy  $\langle E \rangle$  and MLE frequency  $f_{MLE}$ , as shown in figure 5.6. To obtain these curves, which are again normalized to system size, we have derived MLE frequencies using a standard algorithm previously applied by *Zhang et al. (1998)* to assign frequencies to ELMs observed in tokamak plasmas in the JET. A number of MLE discharges  $C_{MLE}$  is obtained for a given time interval  $t_2 - t_1$  and the frequency is then calculated as:

$$f_{MLE} = \frac{C_{MLE}(t_1, t_2)}{t_2 - t_1}. \quad (5.1)$$

Since the sandpile often generates bursts of mass loss with structure down to the smallest time scales, which might not be resolvable under experimental conditions, we have followed *Zhang et al. (1998)* in applying a (relatively narrow) measurement window of width  $450\Delta\tau$  to obtain  $f_{MLE}$ . The correlation between  $\langle E \rangle$  and  $f_{MLE}$  is a noteworthy emergent property. Furthermore, figure 5.6's characteristic curve is very similar to that of figure 5.5 taken from *Fishpool (1998)*, which relates measured energy confinement to ELM frequency in JET. Energy confinement time  $\tau_c$  can be defined for the sandpile by dividing the time averaged stored energy  $\langle E \rangle$  by the time averaged energy dissipation rate  $\langle \Delta E \rangle$  (where  $\Delta E$  is the energy dissipated in a single avalanche). The embedded plot of 5.6 shows  $\tau_c$  against MLE frequency  $f_{MLE}$ .

Finally, we explore the situation where there is a secular change in the redistribution algorithm. In figure 5.7,  $L_f$  decreases slowly, continuously and linearly

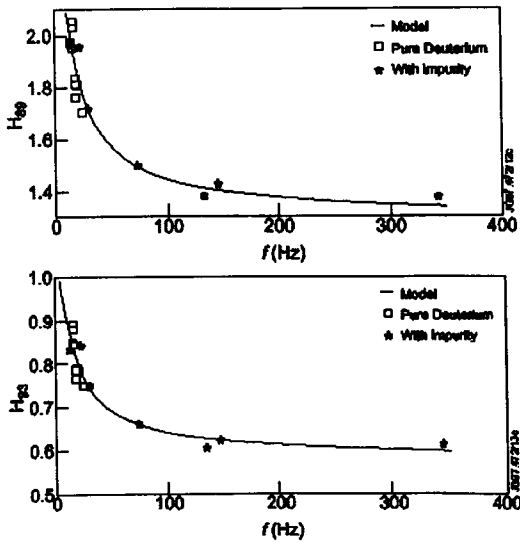


Figure 5.5: Energy confinement versus ELM frequency from  $H_{98}$  (top) and  $H_{93}$  (bottom) measurements. Solid curve corresponds to the model developed in *Fishpool* (1998).

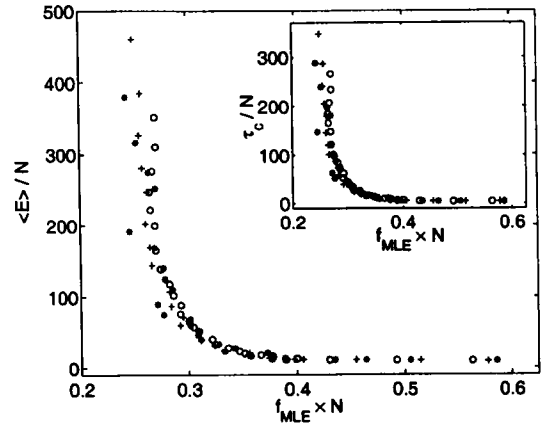


Figure 5.6: Average stored energy versus MLE frequency, and (inset)  $\tau_c$  versus MLE frequency for sandpiles of  $N = 512$ , 4096, and 8192. Energy and MLE frequency are normalized as in figure 5.5.

with time, from one constant value to another, over a period encompassing many tens of thousands of avalanches. There is a corresponding time evolution of the energy confinement properties of the sandpile and of the character of the MLEs. Figure 5.7(top) shows total stored energy as a function of time as  $L_f$  changes from 250 at  $t = 4 \times 10^4$  to 50 at  $t = 1.15 \times 10^5$ , while  $\sim 10^5$  avalanches occur. The system smoothly evolves from low to high confinement over a period of time corresponding to a few tens of MLEs. This is accompanied by a gradual change in character of the time variation in the sandpile edge (position of last occupied cell, figure 5.7(middle)) and of the MLEs (figure 5.7(lower)), from large amplitude to small and from irregular to regular. Figure 5.7 can perhaps be regarded as the analog of, for example, figure 2 of *Zhang et al.* (1998) or figure 2 of *Hugill* (2000). The essential point here is that the sandpile apparently freely explores phase space with changing control parameter  $L_f$ . Characteristic properties of the dynamics (whether quasi-regular or quasi-intermittent) and, correspondingly, confinement properties (such as stored energy and MLE characteristics) smoothly follow changes in this parameter rather

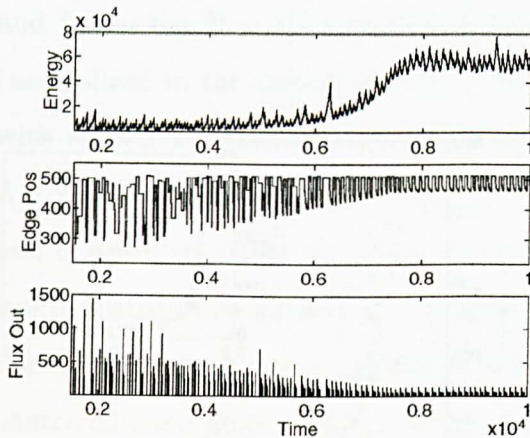


Figure 5.7: Time evolution of (top) stored energy, (middle) sandpile edge position, and (lower) MLEs, as  $L_f$  changes slowly and linearly from 250 to 50.

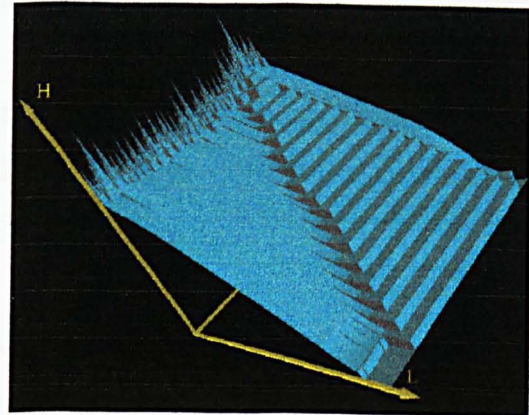


Figure 5.8: Three dimensional view of the sandpile height profile for  $L_f = 50$ . Time evolves along the partially hidden axis. One relaxation phase and one subsequent growth phase are shown.

than exhibiting a sudden phase transition or catastrophe.

## 5.2 Self Organization of Edge and Internal Pedestals in a Sandpile

A distinctive feature of magnetically confined plasmas is that they can sustain local regions having very steep (indeed, almost discontinuous) temperature gradients. Pedestals in the edge temperature are a key feature of the good confinement regimes of tokamaks (“H-modes”) (*Hugill*, 2000). Additionally, advanced operating regimes for tokamaks have now been accessed, which involve the creation of “internal transport barriers” (ITBs). ITBs are step-like features in the temperature profiles internal to the plasma (*Synakowski*, 1998; *Kinsey et al.*, 2001). The occurrence of such structures in externally heated plasma systems that are diffuse, high temperature, and turbulent is surprising. It presents a striking instance of their capacity for macroscopic self-organization. Here, we shall identify how apparently similar structures arise spontaneously in previously discussed sandpile model. Because of the simplicity of this model, it is possible to formally characterize and explain the mechanisms underlying pedestal formation, and to identify links to tokamak plasma behavior.

This approach is complementary to studies that employ large scale numerical simulation of tokamak plasmas, which have had some success in illuminating the subtle interplay between turbulence and bulk flows that may give rise to ITBs (*Kinsey et al.*, 2001).

Evidence for avalanche-type transport from tokamak experiments (*Politzer*, 2000) and numerical simulations (*Garbet and Waltz*, 1998) provides growing support for the applicability in some circumstances of the sandpile paradigm, introduced into fusion plasma physics in recent years (*Newman et al.*, 1996; *Chapman et al.*, 1999). Particularly relevant to the present study are observations and analysis, by *Pedrosa et al.* (1999), of edge plasma turbulence in a range of magnetically confined plasmas. These suggest that edge plasma turbulence, the environment in which H-mode edge pedestals form, which then coexist with the turbulence, self-organizes into a critical state, independent of the size and plasma characteristics of the devices considered. It is known (*Chapman et al.*, 2001c) that, depending on the value of the control parameter  $L_f$ , the statistical behavior of the sandpile model from *Chapman* (2000) displays features reminiscent of enhanced confinement phenomenology in tokamaks. These include the time averaged height profiles, which possess edge pedestals in the good confinement regime. Furthermore, as we have showed in the previous section, the frequency of systemwide avalanches resulting in mass loss scales with stored sandpile energy in the same way as the frequency of edge localized modes (ELMs) scales with stored energy in tokamaks.

The three dimensional plot of figure 5.8 shows sandpile height as a function of position as time evolves, for the good confinement regime with  $L_f = 50$  in a 512 cell system. It displays two distinct phases. First, there is a relaxation phase where the sandpile profile is smooth down to the self-organized edge pedestal, except within a distance  $L_f$  of the core where fueling has a continual local effect. During the relaxation phase mass loss occurs, via many systemwide avalanches closely spaced in time, which carry sand over the sandpile boundary. The relaxation phase terminates with a final systemwide avalanche, after which the growth phase begins. This is characterized by a stationary edge pedestal which resides at the outermost cell of

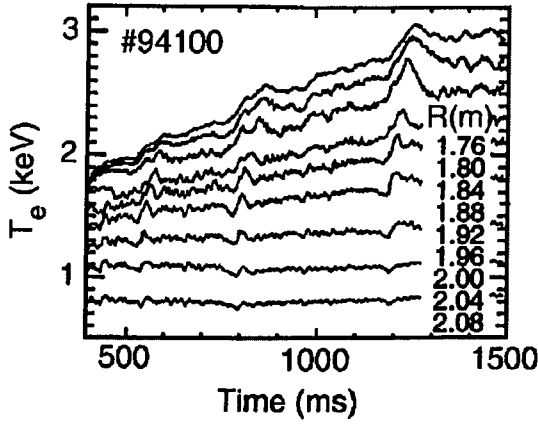


Figure 5.9: Time evolution of the electron temperature at various major radii for DIII-D discharge No. 94100 (*Kinsey et al.*, 2001).

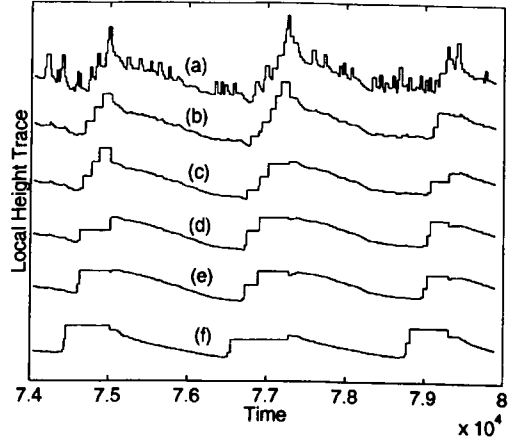


Figure 5.10: Local height of sand as a function of time at different locations in the sandpile relative to the center cell  $n = 1$ : (a)  $n=20$ , (b)  $n=65$ , (c)  $n=100$ , (d)  $n=125$ , (e)  $n=150$  and (f)  $n=300$ . System size  $N = 512$ , control parameter  $L_f = 50$ .

the sandpile. As time progresses, additional pedestals (localized regions of steep gradient just below critical) form successively at positions increasingly close to the core of the sandpile, with average separation  $\sim L_f$ . Each of these is generated at positions where (outward propagating) major internal avalanches have come to rest. The location of the most recently formed (and therefore innermost) internal pedestal propagates inward during the growth phase.

Figure 5.10 is motivated by simultaneous multichannel measurements of tokamak temperature profiles in the presence of ITBs. An examples of such observations is presented in the figure 5.9 adapted from *Kinsey et al.* (2001). Similar observations has been reported in *Burrell et al.* (1998) and in *Kinsey et al.* (2001), also the results of large scale numerical simulations (shown in figure 2 of *Kinsey et al.* (2001)) exhibit a close resemblance to our results. Figure 5.10 shows sandpile height at different positions from the edge to the center. Just over two growth and relaxation phases are shown. The successive formation of internal pedestals is reflected in a stepwise increase in height at any given point during the growth phases. Since the internal pedestals form at locations increasingly close to the core as the growth phase

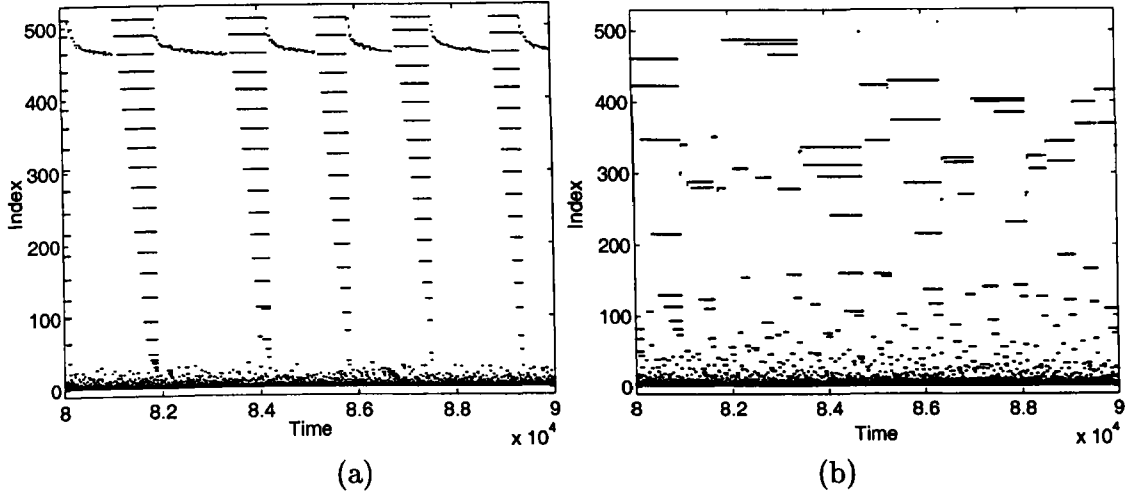


Figure 5.11: Location of cells where the value of the local gradient exceeds  $g_c/2$  for (a)  $L_f = 50$  and (b)  $L_f = 250$ . Zero corresponds to the apex where fueling occurs. The edge pedestal is visible as the uppermost trace.

proceeds, the points within the sandpile that are most affected by the formation of these pedestals, are those closer to the core of the sandpile. Points nearer the edge are only affected by the formation of the first few internal pedestals during the early growth phase. The results shown in figure 5.10 emerge naturally from the dynamics of the sandpile during the growth phase of its good confinement regime. Central to this structure is the unexpected capacity of this sandpile to organize persistent steep pedestals both at the edge and internally.

The role of these internal pedestals and their relationship to the edge pedestal is highlighted in figures 5.11. In this figure, all cells at which the gradient exceeds  $g_c/2$  are marked by black points, while all other cells are left blank. In figure 5.11(a) ( $L_f = 50$ ) data follows five of the growth and relaxation cycles shown in figure 5.10. The edge pedestal is visible close to the sandpile boundary in both the relaxation and the growth phases. Its time behavior is essentially regular and, as we shall see, orders the structure internal to the sandpile. For any  $L_f < N/4$ , the location of each internal pedestal is fixed during a given growth phase, so that they persist as distinguishable features of the time averaged phenomenology of the sandpile. In contrast, figure 5.11(b) shows the behavior for the poor confinement (SOC) regime with  $L_f = 250 > N/4$ . Although the sandpile successively fills and empties, it does



so in an irregular manner. Pedestals can be seen both at the edge and internal to the sandpile, but these are no longer organized in a coherent pattern. The time averaged profile of this sandpile is smooth and corresponds to low energy confinement (see figure 5.1).

A resilient edge pedestal arises for all  $L_f$ ; the pedestal is steep, indeed unresolved, in that the entire change in height occurs between neighboring cells. The location of the edge pedestal is strongly time dependent for large  $L_f$ , whereas for small  $L_f$  it is confined to a region close to the outermost cell of the sandpile. The time averaged profile in the edge region, therefore, depends strongly on  $L_f$ , and the steadyest edge pedestal corresponds to small  $L_f$  and good confinement. Following each avalanche in our algorithm, the value of the critical gradient  $g_c$  is randomized about a mean value at all cells that participated in the avalanche. Nevertheless, the gradient at the edge pedestal remains always close to, but just below, the critical value  $g_c$  as shown in figure 5.12. Elsewhere in the sandpile (for example at its midpoint), except where internal pedestals arise, the gradient is well below  $g_c$ . The internal pedestals appear as barriers to transport: despite their apparent fragility against avalanching (gradient  $g$  close to  $g_c$ ), no sand passes through either the edge or the internal pedestals until the final avalanche that terminates the growth phase. The physical mechanisms and principles underlying the self organization of the edge pedestal and multiple internal pedestals that arise in the sandpile model of Refs. *Chapman* (2000); *Chapman et al.* (2001c) are, therefore, of considerable interest. As a first step, we confirm the hypothesis of *Chapman et al.* (2001c) that the good confinement regime (small  $L_f$ ) corresponds to low dimensional behavior. In figures 5.13 the position of the last occupied cell at time  $t$  is plotted against that at time  $t + \tau$ , where  $\tau = 50$ , for runs with  $L_f = (a)50$ ,  $(b)150$  and  $(c)250$  in a 512 cell system. This is an example of phase space reconstruction, achieved here by embedding (*Ott*, 1993). Figure 5.13(a) shows low dimensional system dynamics that repeatedly follows a simple limit cycle (attractor) around a restricted region of the reconstructed phase space. This implies that the large number of cells in the sandpile have self-organized: their collective dynamics are encapsulated by a small number of dynamical variables. Once  $L_f$  is

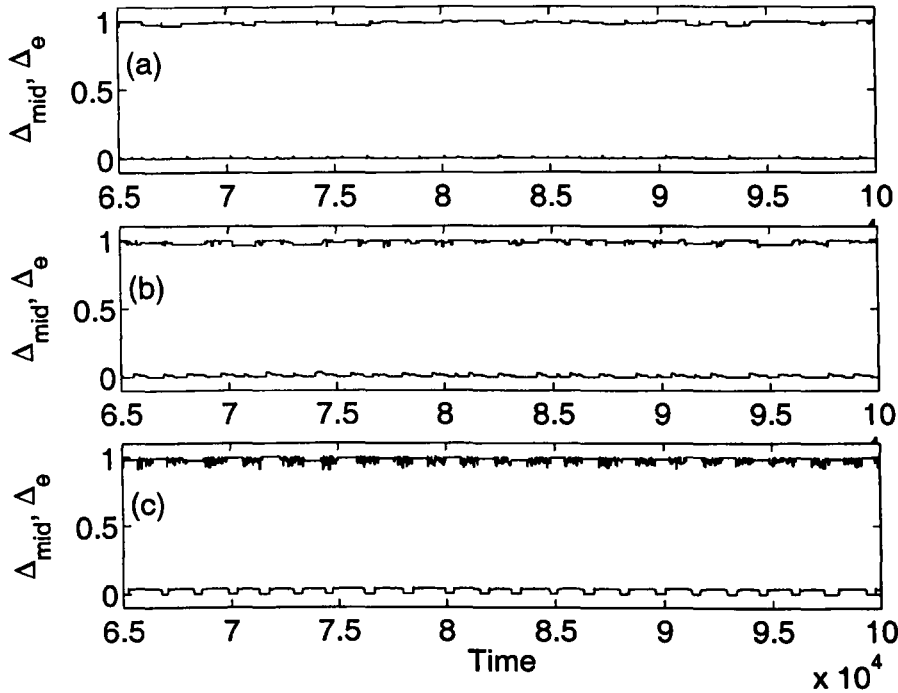


Figure 5.12: Local gradient normalized to the local value of  $g_c$  for cells at the edge ( $\Delta_e$ , upper traces, value close to unity) and halfway into the sandpile ( $\Delta_{mid}$ , lower traces, value close to zero), for  $L_f =$  (top) 250, (center) 150, (bottom) 50.

increased to 150 (figure 5.13(b)), the simple limit cycle seen in figure 5.13(a) bifurcates, and more stochastic behavior is seen in figure 5.13(c) ( $L_f = 250$ ). Thus, increasing complexity of the phase space portrait correlates with deterioration of confinement. The lowest confinement regime corresponds to self-similar avalanche statistics. This is associated with a nontrivial fixed point in the space of the parameter used in *Tam et al.* (1999) to perform rescaling under the RG procedure, corresponding to behavior that is both self-organized and critical (*Sethna et al.*, 2001). Importantly, global relaxation of the sandpile is ultimately achieved by large (systemwide) avalanches for all values of  $L_f$ . When  $L_f$  is of order the system size  $N$ , systemwide avalanches are straightforwardly propagated: because  $L_f \sim N$ , no characteristic scale is imposed by the redistribution process and the dynamics are self-similar and in SOC (*Tam et al.*, 1999). Conversely, when  $L_f$  is significantly distinct from the system size (found empirically to be  $L_f < N/4$ ), there is scale breaking. This leads to broken power law avalanche statistics (*Chapman*, 2000) and

the system is no longer in SOC. By separating the characteristic length scales we also effectively separate the long term growth-relaxation time scale from the time interval between systemwide avalanches. In the SOC regime, such a distinction is not possible. Thus, in the good confinement regime (when  $L_f < N/4$ ) the requirement for self organization is satisfied. The feature evolving on the slow time scale, namely the position of the edge pedestal, is sufficient to determine the details of the internal dynamics. It organizes the sequence of events leading to the successive formation of internal edge pedestals and the time variation of total energy (sand) in the system. In short, the sandpile is entrained to its edge.

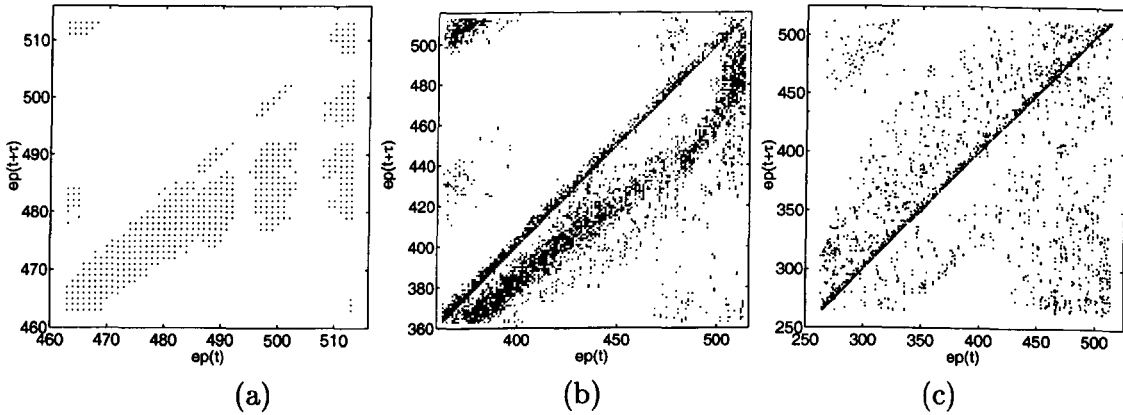


Figure 5.13: Phase space reconstruction of the dynamics of the edge position  $ep(t)$ . Plotted are coordinates  $ep(t)$  versus  $ep(t + \tau)$  for  $\tau = 50$  and  $L_f =$  (a) 50, (b) 150 and (c) 250. The system dynamics explore a larger region of the phase space with increasing values of  $L_f$ . The topology shown is insensitive to the value of  $\tau$  in the range of interest.

### 5.3 Conclusions

By varying a single control parameter in the sandpile algorithm, we have shown correlations between stored energy, confinement times, sandpile profile, sandpile edge structure and the amplitude, frequency and dynamical character of mass loss events. We have also seen how slow secular change in the control parameter produces a smooth evolution in confinement properties. If a single control parameter analogous to  $L_f$  exists for tokamaks, it can, in principle, be found from experimental data by examining scaling with respect to system size. The existence of

such extensive tokamak-like phenomenology, emergent from a very simple system, is a novel discovery. Insofar, as the phenomenological resemblance is close, there is more to be learned. A minimalist interpretation starts from the premise that the sandpile algorithm provides a simple one-parameter model for studying generic nonlocal transport, conditioned by a critical gradient, in a macroscopic confinement system. Changing the value of the single control parameter  $L_f$  then corresponds to altering the range in configuration space over which the transport process operates. It then follows from the results presented here, that this may be the minimum requirement to generate those aspects of tokamak-like confinement phenomenology described. This is a significant conclusion but one can consider a more far reaching one. A possible maximalist interpretation attaches greater weight to recent observations reported in *Carreras and Newman (1996)*; *Rhodes et al. (1999)*; *Politzer (2000)* of avalanching transport in tokamaks and in large scale numerical simulations (*Garbet and Waltz, 1998*; *Sarazin and Ghendrih, 1998*) thereof, and therefore regards the avalanching transport that is built into sandpile algorithms as an additional point of contact with magnetically confined plasmas. One would then infer from the present results that tokamak observations of avalanching transport are deeply linked to the existence of enhanced confinement and ELMs. The confinement physics of our sandpile model offers a robust framework in which a distinctive structure of edge and internal pedestals (previously known only from tokamak plasmas) arises naturally. There is only one control parameter,  $L_f/N$ , which can be considered as a proxy for the lengthscale of turbulent transport, normalized to system size. Provided that this lengthscale is sufficiently short, the underlying system dynamics give rise to persistent, marginally subcritical profile steps whose formation point propagates inwards in the growth phase. Furthermore, the self-organized edge pedestal is continuously present in all phases of the sandpile evolution and positions itself exactly at the sandpile boundary throughout the growth phase. These results are sufficient to indicate that some of the distinctive edge and internal pedestal phenomenology, seen in tokamak plasmas, can also arise in a simpler idealized confinement system, and that they may be linked to the observed avalanching transport phenomena.

## Chapter 6

# Intermittency, scaling and a Fokker-Planck approach to solar wind fluctuations and coupled solar wind-magnetosphere system

In Chapter 2, have we discussed a finite size scaling method that can be applied to a time series obtained from the turbulent system. We also derived a Fokker-Planck equation and have shown how it relates to the rescaling procedure. We will now apply this technique to investigate the solar wind and the coupled solar wind-magnetosphere system. For the solar wind studies, we consider bulk plasma parameters provided by the WIND spacecraft. These are magnetic field magnitude  $B$ , velocity magnitude  $v$ , ion density  $\rho$ , kinetic and magnetic energy density ( $\rho v^2$  and  $B^2$ ) and Poynting flux approximated by  $vB^2$ . Such approximation of the Poynting flux is consistent with ideal MHD where  $\mathbf{E} = \mathbf{v} \times \mathbf{B}$ . We will show that fluctuations in the ion density  $\rho$ , energy densities  $B^2$  and  $\rho v^2$  as well as MHD-approximated Poynting flux  $vB^2$  are self-similar, whereas the fluctuations of speed  $v$  and IMF

magnitude  $B$  are multi-fractal. The mono-scaling nature of these fluctuations suggests a simplified picture of the intermittency in the turbulent energy cascade for these quantities. We also develop a Fokker-Planck model of these fluctuations which allows us to identify the transport coefficients in the plasma. We will compare this stochastic model with the Castaing distribution derived from turbulence.

We will also consider the coupled solar wind-magnetosphere system. Recent work has focused on comparing some aspects of the scaling properties of input parameters such as  $\epsilon$ , given by (1.15) and the AE index (*Davis and Sugiura, 1966*) to establish whether, to the lowest order, they are directly related (*Freeman et al., 2000a; Uritsky et al., 2001*). We use the finite size scaling to directly compare the PDF of the solar wind driver, represented by the  $\epsilon$  parameter with PDFs of the global magnetospheric indices AU, AL and AE. Our results suggest a strong connection between the scaling of the driver and that observed in the indices. This is also supported by the identical, to within the error, value of the rescaling indices found for these quantities and a common temporal scale at which this mono-scaling can no longer be found.

The work presented here has been published in *Hnat et al. (2002a,b)*.

## 6.1 The Dataset

The solar wind is a supersonic, super-Alfvénic flow of the compressible and inhomogeneous plasma. The WIND spacecraft orbits the Earth-Sun  $L1$  point providing magnetic field measurements from the MFI experiment (*Lepping et al., 1995*) and the plasma parameters from the SWE instrument (*Ogilvie et al., 1995*). The WIND solar wind magnetic field and key parameter database used in here comprise over 1.5 million, 46 second averaged samples from January 1995 to December 1998 inclusive. The selection criteria for solar wind data was given by the component of the spacecraft position vector along the Earth-Sun line,  $X > 0$ , and the vector magnitude,  $R > 30$  RE. The data set includes intervals of both slow and fast speed streams. Table 6.1 outlines typical range of values found in the solar wind at  $\sim 1$  Astronom-

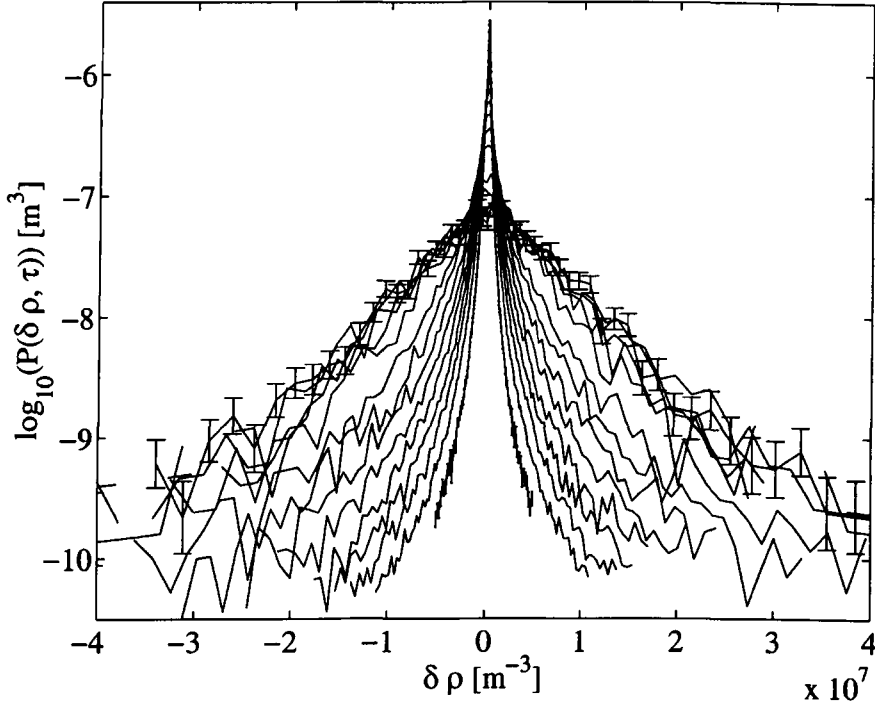


Figure 6.1: Unscaled PDFs of the ion density fluctuations. Time lag  $\tau = 2^k \times 46\text{s}$ , where  $k = 0, 1, 2, \dots, 14$ . Standard deviation of the PDF increases with  $\tau$ . Error bars on each bin within the PDF are estimated assuming Gaussian statistics for the data within each bin.

ical Unit. Similar to other satellite measurements, short gaps in the WIND data file were present. We have omitted any intervals where the gap was larger than 2% to minimize the errors caused by such incomplete measurements. The original data were not averaged nor detrended. Two dominant sampling frequencies, 1/46Hz and 1/92Hz, has been identified in the data set. We use sampling frequency  $f_s$  of 1/46 as our base and treat other temporal resolutions as gaps when the accuracy requires it ( $\tau \leq 92$  seconds).

Geomagnetic indices are obtained from a number of ground magnetometer stations (usually greater than 10) distributed in the latitude region of the northern hemisphere auroral zone. The north-south magnetic perturbation  $\delta B_{NS}$  is measured as, a function of universal time, for each of the stations. The maximum negative excursion of the perturbations  $\delta B_{NS}$  from all stations constitutes AL index. Similarly, maximum positive excursion in  $\delta B_{NS}$  is called the AU index. The difference between these two indices, AU-AL, gives the AE index. The indices AU and AL pro-

Parameter	Value(s) at 1AU
Proton density	$0.4 - 100\text{cm}^{-3}$
Magnetic field	$0.2 - 80\text{nT}$
Flow speed	$200 - 900\text{km/s}$
Proton gyroradius	$80\text{km}$
Proton-proton collision time	$4 \times 10^6\text{s}$

Table 6.1: Typical parameters of the solar wind at 1AU.

vide measure of the individual strengths of eastward and westward electrojets, while AE gives a good estimate of the overall horizontal current strength. Excursions in the AE index from a nominal daily baseline are called magnetospheric substorms and may have durations of tens of minutes to several hours. The AL, AU and AE indices data set investigated here comprises over 0.5 million, 1 minute averaged samples from January 1978 to January 1979 inclusive. The  $\epsilon$  parameter was computed according to (1.15) and (1.16) from the WIND magnetic field and key parameter database described in the previous section. The time series of indices and that of the  $\epsilon$  parameter were obtained in different time intervals and we assume that the samples are long enough to be statistically accurate.

## 6.2 Estimates of the rescaling index

Let  $x(t)$  represent the time series of the studied signal, in our case magnetic field magnitude  $B$ , velocity magnitude  $v$ , ion density  $\rho$ , kinetic energy density  $\rho v^2$ , magnetic field energy density  $B^2$ , the Poynting flux component approximated by  $vB^2$ , Akasofu  $\epsilon$  parameter or any of the geomagnetic indices. A set of time series  $\delta x(t, \tau) = x(t + \tau) - x(t)$  is obtained for each value of non-overlapping time lag  $\tau$ . The PDF  $P(\delta x, \tau)$  is then generated for each time series  $\delta x(t, \tau)$ . We extract the scaling index  $\alpha$  directly from differenced time series of the quantity  $x$  as described in Section 2.2.2. Ideally, we use the peaks of the PDFs to obtain the scaling exponent  $\alpha$ , as the peaks are statistically the most accurate parts of the distributions. In certain cases, however, the peaks may not be the optimal statistical measure for



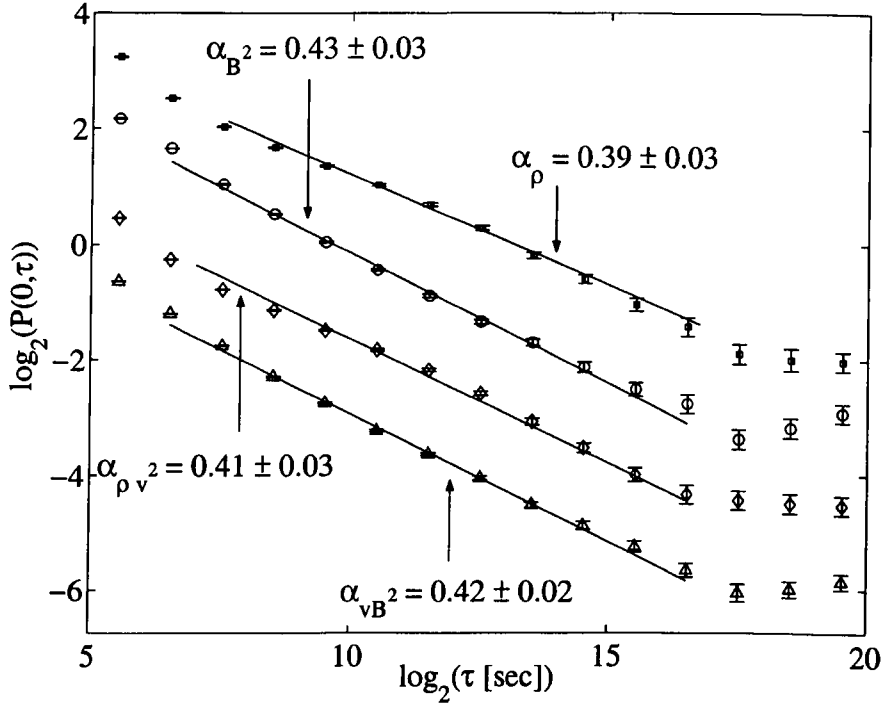


Figure 6.2: Scaling of the peaks  $P(0, \tau)$  of the PDFs for all quantities under investigation:  $\circ$  corresponds to  $\delta B^2$ ,  $\square$  ion density  $\delta \rho$ ,  $\diamond$  kinetic energy density  $\delta(\rho v^2)$  and  $\triangle$  Poynting flux component  $\delta(vB^2)$ . The plots have been offset vertically for clarity. Errors as in figure 6.1.

obtaining the scaling index. For example, the  $B_z$  component of the magnetic field is measured with an absolute accuracy of about 0.1 nT. Such discreteness in the time series introduces large errors in the estimation of the peak values  $P(0, \tau)$  and may not give a correct scaling. However, if the PDFs rescale, we can obtain the scaling exponent from any point on the curve, in principle. We will illustrate that in the next sections where we obtain the rescaling index  $\alpha$  from two points on the curve  $P(0, \tau)$  and  $P(\sigma, \tau)$  for the solar wind. For the  $\epsilon$  parameter and the geomagnetic indices, we will compare  $\alpha$  obtained from the PDF peaks with that given by the temporal scaling of the variance (Hurst exponent, see definition (2.40)).

### 6.3 Scaling in the solar wind bulk plasma parameters

We are now ready to present results of the rescaling procedure as applied to the solar wind bulk plasma parameters. Figure 6.1 shows the unscaled (raw) PDF curves of

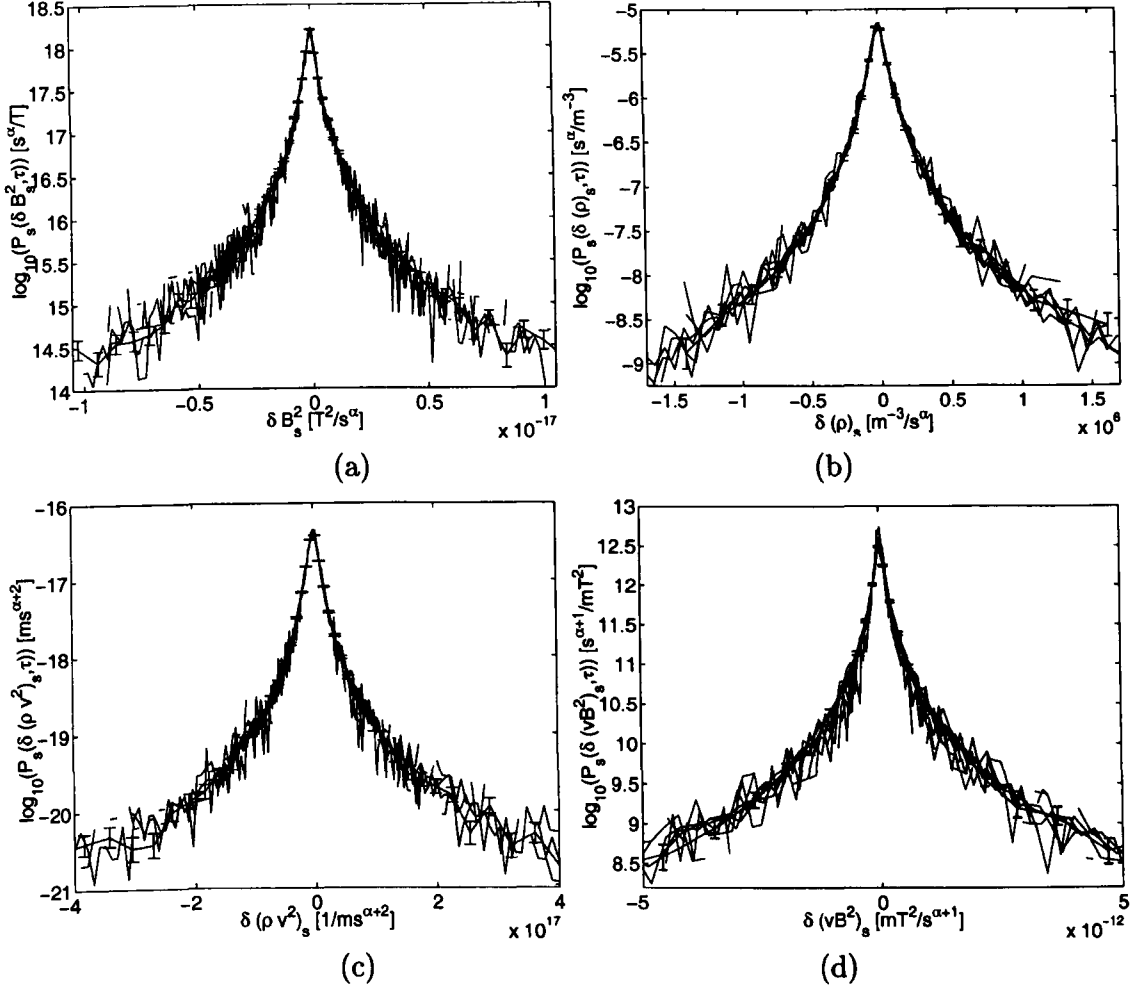


Figure 6.3: One parameter rescaling of the PDF for (a)  $\delta B^2$ , (b)  $\delta \rho$ , (c)  $\delta(\rho v^2)$  and (d)  $\delta(vB^2)$  PDFs. The curves shown correspond to  $\tau$  between  $\sim 2$  minutes and  $\sim 26$  hours. Error bars as in figure 6.1.

the ion density data. These PDFs, like all others presented in this section, were generated with the bin size decreasing linearly toward the center of the distribution. This improves the accuracy with which the peak  $P(0, \tau)$  of each PDF can be located. Although the entire range of data was used to create these PDFs, we truncated the plotted curves for  $|\delta x| \geq 10\sigma(\tau)$ , where  $\sigma(\tau)$  is a standard deviation of the differenced time series for the specific time lag  $\tau$ . Figure 6.2 shows  $P(0, \tau)$  plotted versus  $\tau$  on log-log axes for  $\delta x = \delta(\rho)$ ,  $\delta(\rho v^2)$ ,  $\delta(B^2)$  and  $\delta(vB^2)$ . Straight lines on this plot suggest that the rescaling (2.27) holds for the peaks of the distributions. In Figure 6.2, lines were fitted with  $R^2$  goodness of fit for the range of  $\tau$  between  $\sim 2$

minutes and  $\sim 26$  hours, omitting points corresponding to the first two temporal scales as in these cases the sharp peaks of the PDFs can not be well resolved. The lines suggest self-similarity persists up to intervals of  $\tau \approx 26$  hours. The slopes of these lines yield the exponents  $\alpha$ . These are summarized in Table 6.2 along with the values obtained from analogous plots of  $P(\sigma(\tau), \tau)$  versus  $\tau$  which show the same scale break and the same scaling exponent for  $\delta(\rho)$ ,  $\delta(\rho v^2)$ ,  $\delta(B^2)$  and  $\delta(vB^2)$ , within the error.

Quantity	$\alpha$ from $P(0, \tau)$	$\alpha$ from $P(\sigma, \tau)$	Approx. $\tau_{max}$	PDF scales
$\delta B$	$-0.47 \pm 0.02$	$-0.23 \pm 0.05$	26 hrs	No
$\delta v$	$-0.52 \pm 0.05$	$-0.21 \pm 0.06$	26 hrs	No
$\delta(B^2)$	$-0.43 \pm 0.03$	$-0.42 \pm 0.08$	26 hrs	Yes
$\delta(\rho)$	$-0.39 \pm 0.03$	$-0.37 \pm 0.05$	26 hrs	Yes
$\delta(\rho v^2)$	$-0.41 \pm 0.03$	$-0.37 \pm 0.05$	26 hrs	Yes
$\delta(vB^2)$	$-0.42 \pm 0.02$	$-0.43 \pm 0.06$	26 hrs	Yes

Table 6.2: Scaling indices derived from  $P(0, \tau)$  and  $P(\sigma, \tau)$  power laws.

Within this scaling range, we now attempt to collapse each corresponding unscaled PDF onto a single master curve using the scaling (2.27). Figures 6.3(a,b,c,d) show the result of one parameter rescaling applied to this unscaled PDF of fluctuations in  $\rho$ ,  $\rho v^2$ ,  $B^2$  and  $vB^2$  respectively, for the temporal scales up to  $\sim 26$  hours. We see that the rescaling procedure (2.27) using the value of the exponent  $\alpha$  of the peaks  $P(0, \tau)$  shown in figure 6.2, gives good collapse of each curve onto a single common functional form for the entire range of the data. These rescaled PDFs are leptokurtic rather than Gaussian. This is strongly suggestive of an underlying nonlinear process. All PDFs are symmetric with the exception of the density fluctuations which seem to have higher values for the large positive values as compared to the negative ones. It has been reported previously in *Castaing et al. (1990)* that the PDFs obtained from hydrodynamic turbulence have exponential tails. These look linear on the semi-log plots that are commonly used here and elsewhere in the literature. In the case of the solar wind bulk plasma parameters, we do not find

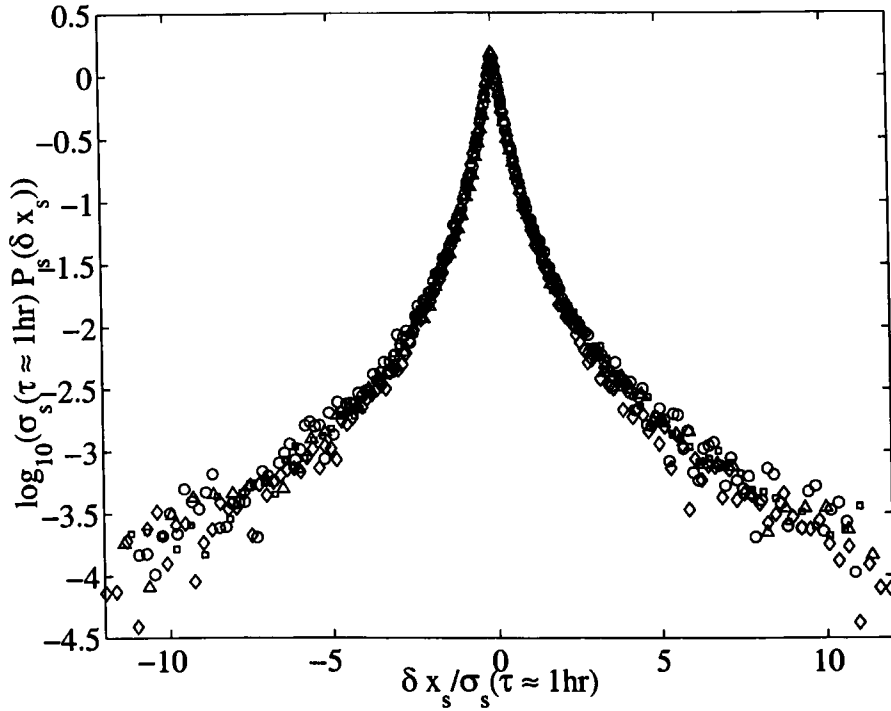


Figure 6.4: Direct comparison of the PDFs of fluctuations for all four quantities.  $\circ$  corresponds to  $\delta(B^2)$ ,  $\square$  ion density  $\delta(\rho)$ ,  $\diamond$  kinetic energy density  $\delta(\rho v^2)$  and  $\triangle$  Poynting flux component  $\delta(vB^2)$ .

such clear exponential cutoff region but rather see stretched exponential tails of the form  $\exp(-A|\delta x|^\mu)$  (Veltri, 1999). We can now directly compare these rescaled PDFs by overlying the curves on the single plot for a particular  $\tau$  within the scaling range. Fig. 6.4 shows these normalized PDFs  $P_s(\delta x_s, \tau)$  for  $\delta x_s = \delta(\rho)_s, \delta(B^2)_s, \delta(\rho v^2)_s, \delta(vB^2)_s$  and  $\tau \approx 1$  hour overlaid on a single plot. The  $\delta x_s$  variable has been normalized to the rescaled standard deviation  $\sigma_s(\tau \approx 1 \text{ hr})$  of  $P_s$  in each case to facilitate this comparison. These normalized PDFs have remarkably similar functional form suggesting a shared process responsible for fluctuations in these four plasma parameters on temporal scales up to  $\tau_{max} \approx 26$  hours.

It has been found previously by Burlaga (2001) that the magnetic field magnitude fluctuations are not self-similar but rather multi-fractal. For such processes, the scaling derived from  $P(0, \tau)$  would not be expected to rescale the entire PDF. To verify this, we applied the rescaling procedure for magnetic field magnitude differences  $\delta B(t, \tau) = B(t + \tau) - B(t)$ . Figure 6.5(a) shows the result of one parameter

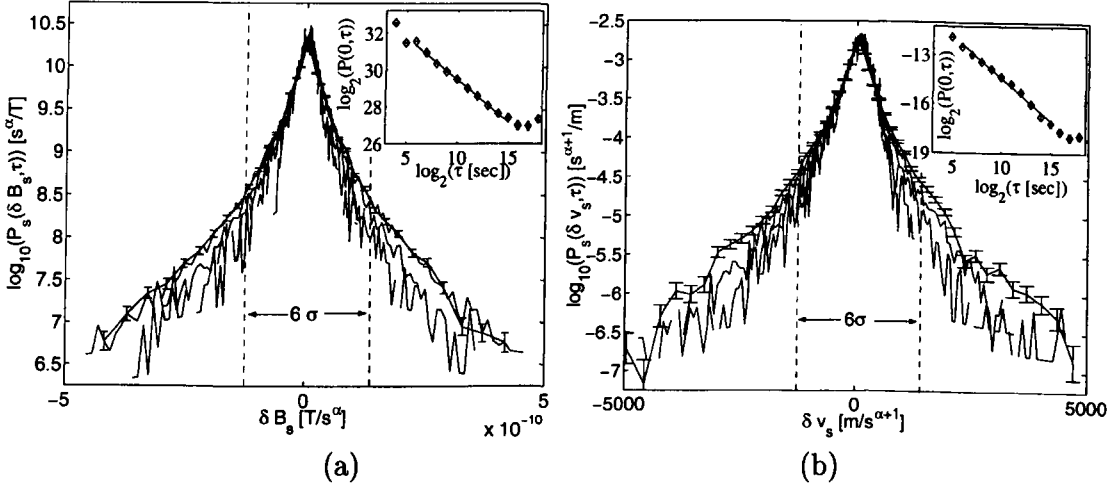


Figure 6.5: One parameter rescaling of the PDF for the fluctuations in the (a) magnetic field magnitude  $B$  and (b) velocity magnitude. The curves shown correspond to  $\tau$  between  $\sim 2$  minutes and  $\sim 26$  hours. Error bars as in figure 6.1.

rescaling applied to the PDFs of the magnetic field magnitude fluctuations. We see that the scaling procedure is satisfactory only up to 3 standard deviations of the original sample, despite the satisfactory scaling obtained for the peaks  $P(0, \tau)$  of the PDFs (see insert of the figure 6.5(a)). This confirms the results of *Sorriso-Valvo et al.* (1999) where a two parameter Castaing fit to values within 3 standard deviations of the original sample yields scaling in one parameter and weak variation in the other. Attempts to improve the collapse by using information in the tails (values  $|\delta B| > 3\sigma$ ) would introduce a significant error in the estimation of the scaling exponent  $\alpha$ . We found similar lack of scaling in the fluctuations of the solar wind velocity magnitude and we show the rescaled PDF in the figure 6.5(b). We stress that the log-log plots of the PDF peaks  $P(0, \tau)$  show a linear region for both velocity and magnetic field magnitude fluctuations (see insert in each figure). Their PDFs, however, do not collapse onto a single curve when the rescaling (2.27) is applied. This lack of mono-scaling is evident when indices derived from  $P(0, \tau)$  and these found for  $P(\sigma, \tau)$  are compared (see Table 6.2).

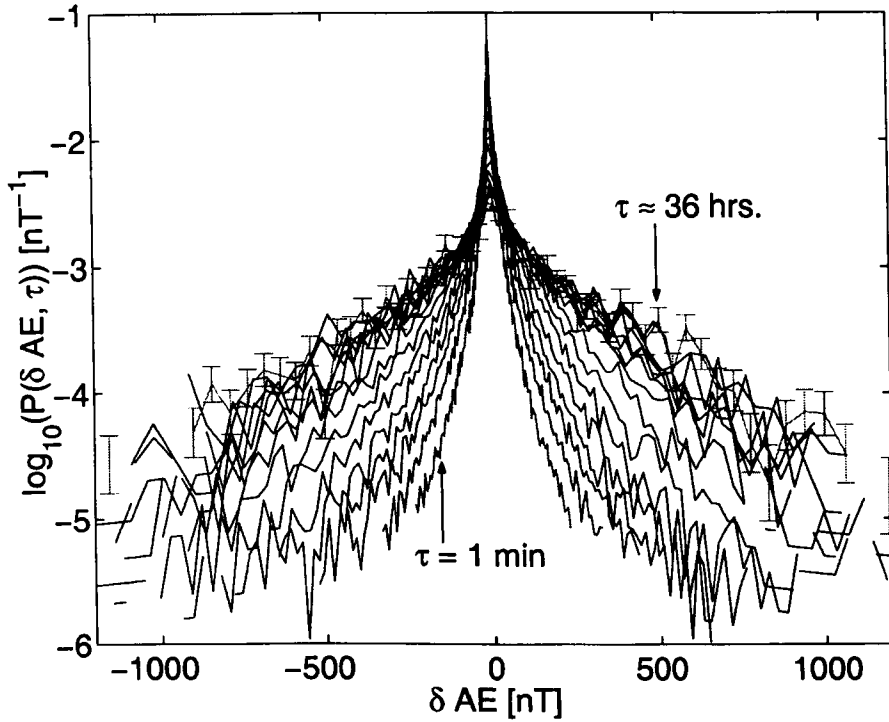


Figure 6.6: Unscaled PDFs of the AU index fluctuations. Time lag  $\tau$  assumes values between 60 seconds and about 36 hrs. Standard deviation of the PDF increases with  $\tau$ . Error bars as in figure 6.1.

## 6.4 Scaling in the solar wind $\epsilon$ and geomagnetic indices

Figure 6.6 shows these PDFs for the  $\delta AU$ . A generic scaling approach is applied to these PDFs. Figure 6.7 shows  $P(0, \tau)$  plotted versus  $\tau$  on log-log axes for  $\delta x = \delta \epsilon$ ,  $\delta AE$ ,  $\delta AU$  and  $\delta AL$ . Straight lines, fitted for the range of  $\tau$  between 4 and 136 minutes, suggest self-similarity persists up to intervals of  $\tau = 97 - 136$  minutes. The slopes of these lines yield the exponents  $\alpha$  and these are summarized in Table 6.4 along with the values obtained from plots of  $\sigma(\tau)$  versus  $\tau$  which show the same scale break. We note that, for the  $\epsilon$  parameter, the scaling index  $\alpha$  obtained from the  $P(0, \tau)$  is different from the Hurst exponent measured from the  $\sigma(\tau)$ . This difference could be a result of the previously discussed difficulties with the  $\epsilon$  data (discreteness of the time series). However, it does appear to be a feature of some real time series (see *Gopikrishnan et al (1999)*, for example). Indeed, such a difference between index  $\alpha$  and a Hurst exponent  $H_\sigma$  is predicted in the case of the fractional

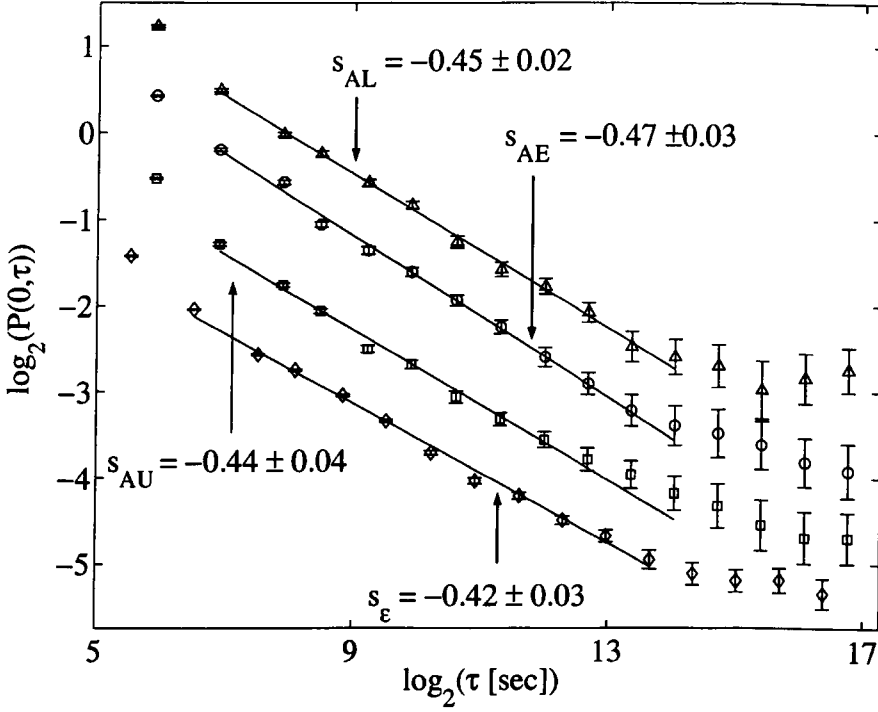


Figure 6.7: Scaling of the peaks of the PDFs for all quantities under investigation:  $\diamond$  corresponds to  $\epsilon$ ,  $\circ$  AU index,  $\triangle$  AL index and  $\square$  the AE index. The plots have been offset vertically for clarity. Error bars as in figure 6.1.

Lévy motion (*Chechkin and Gonchar, 2000*).

We see that, for the  $\epsilon$  as well as the AL and AU indices, there is a range of  $\tau$  up to  $\sim 4.5$  hours for which  $P(0, \tau)$  plotted versus  $\tau$  is well described by a power law  $\tau^{-\alpha}$  with indices  $\alpha = 0.42 \pm 0.03$  for the  $\epsilon$  and  $\alpha = 0.45 \pm 0.02$  and  $\alpha = 0.47 \pm 0.03$  for the AL and AU indices, respectively. Thus the break in scaling at  $\sim 4.5$  hours in the AL and AU indices may have its origin in the solar wind, although the physical reason for the break at this timescale in epsilon is unclear. The break in the AE index, however, appears to occur at a smaller temporal scale of  $\sim 2$  hours, consistent with the scaling break timescale found in the same index by other analysis methods (*Consolini and De Michelis, 1998; Takalo et al., 1993*). This was interpreted by *Takalo et al. (1993)* as due to the characteristic substorm duration. *Takalo et al. (1998)* also reported a scaling break at the same 2 hour timescale for AL, in contrast to the 4 to 5 hour timescale found here. Indeed, one might have expected a substorm timescale to cause the same scaling break in both

the AE and AL indices, because their substorm signatures are so similar in profile (e.g., figure 2 of *Caan et al. (1978)*). The resolution may lie in the difference between analysis of differenced and undifferenced data (*Price and Newman, 2001*).

Quantity	$\alpha$ from $P(0, \tau)$	$\alpha$ from $\sigma(\tau)$	Approx. $\tau_{max}$
$\epsilon$	$-0.42 \pm 0.03$	$0.33 \pm 0.04$	4.5 hrs
AE-index	$-0.44 \pm 0.03$	$0.43 \pm 0.03$	2.1 hrs
AU-index	$-0.47 \pm 0.03$	$0.47 \pm 0.02$	4.5 hrs
AL-index	$-0.45 \pm 0.02$	$0.45 \pm 0.02$	4.5 hrs

Table 6.3: Scaling indices derived from  $P(0, \tau)$  and  $\sigma(\tau)$  power laws.

Figures 6.8(a,b,c,d) show the result of the one parameter rescaling applied to the unscaled PDF of the  $\delta\epsilon$  and the fluctuations of indices, respectively, for the temporal scales up to  $\sim 4.5$  hours. We see that the rescaling procedure (2.27) using the value of the exponent  $\alpha$  of the peaks  $P(0, \tau)$  shown in Figure 6.7, gives good collapse of each curve onto a single common functional form for the entire range of the data. These rescaled PDFs are leptokurtic rather than a Gaussian and are thus strongly suggestive of an underlying turbulent process.

The successful rescaling of the PDFs now allows us to perform a direct comparison of the PDFs for all four quantities. Figure 6.9 shows these normalized PDFs  $P_s(\delta X, \tau)$  for  $\delta X = \delta\epsilon$ ,  $\delta AE$  and  $\tau \approx 1$  hour overlaid on a single plot. The  $\delta X$  variable has been normalized to the rescaled standard deviation  $\sigma_s(\tau \approx 1hr)$  of  $P_s$  in each case to facilitate this comparison. We then find that AE and  $\epsilon$  fluctuations have indistinguishable  $P_s$ . The PDFs of  $\delta AU$  and  $\delta AL$  are asymmetric such that  $-\delta AL$  fits  $\delta AU$  PDF closely (see insert in the figure 6.9); when overlaid on the PDFs of the  $\delta\epsilon$  and  $\delta AE$  these are also indistinguishable within errors. This provides strong evidence that the dominant contributions to the AE indices come from the eastward and westward electrojets of the approximately symmetric DP2 current system that is driven directly by the solar wind (*Freeman et al., 2000a*). The mono-scaling of the investigated PDFs, together with the finite value of the samples' variance, indicates that a Fokker-Planck approach can be used to study the dynamics of the unscaled



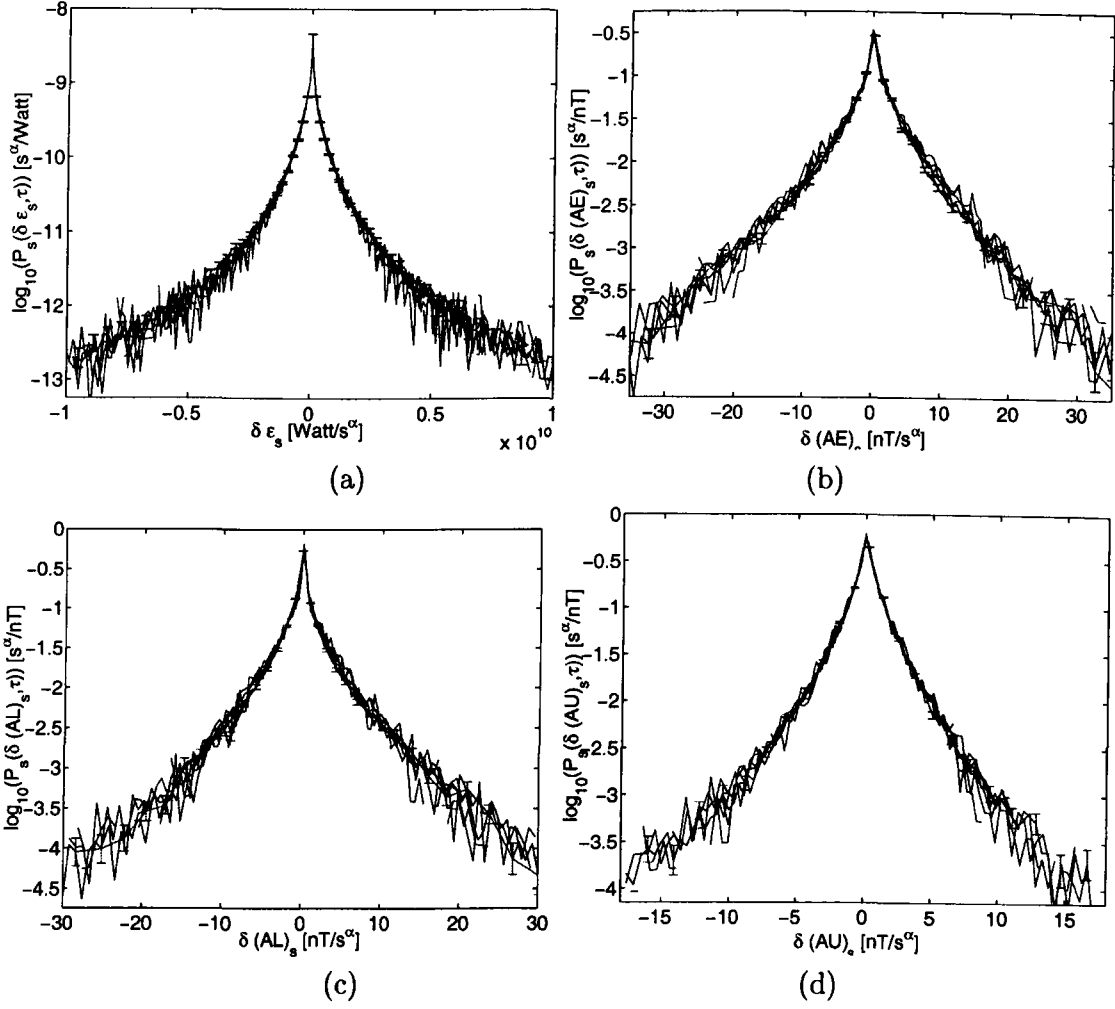


Figure 6.8: One parameter rescaling of the fluctuation PDF for (a) $\epsilon$  parameter, (b)AE index, (c)AL index and (d)AU index. The curves shown correspond to  $\tau$  between 46 seconds and  $\sim 4.5$  hours.

PDFs within their temporal scaling range.

## 6.5 Modelling the data

The rescaling technique applied in the previous sections indicates that, for certain temporal scales, PDFs of certain solar wind bulk plasma parameters can be collapsed onto a single master curve. The challenge now lays in developing physical models that can describe the functional form of this curve. Here, we consider two approaches. The first one is a statistical approach where we assume that the fluctuations can be described by a stochastic Langevin equation. The second method is

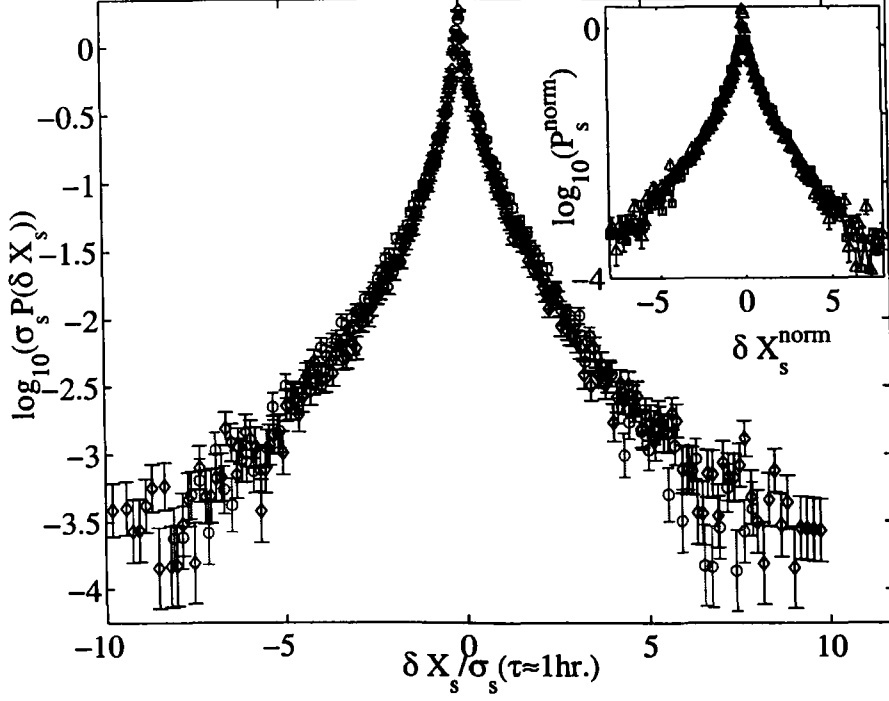


Figure 6.9: Direct comparison of the fluctuations PDFs for  $\epsilon$  ( $\diamond$ ) and AE index ( $\circ$ ). Insert shows overlaid PDFs of AU( $\square$ ) and  $-AL$ ( $\triangle$ ) fluctuations.

to assume the fluctuations are the result of the nonlinear energy cascade and derive the corresponding PDF form for the rescaled PDFs (Castaing distribution).

### 6.5.1 Diffusion model

The Fokker-Planck equation (FPE) provides an important link between statistical studies and the dynamical approach expressed by the Langevin equation (*Sornette, 2000*). In the most general form, FPE can be written as:

$$\frac{\partial P}{\partial \tau} = \nabla_{\delta x} (A(\delta x)P + B(\delta x)\nabla_{\delta x}P), \quad (6.1)$$

where  $P \equiv P(\delta x, \tau)$  is a PDF for the differenced quantity  $\delta x$  that varies with time  $\tau$ ,  $A(\delta x)$  is the friction coefficient and  $B(\delta x)$  is related to a diffusion coefficient which we assume to vary with  $\delta x$ . For certain choices of  $A(\delta x)$  and  $B(\delta x)$ , a class of self-similar solutions of (6.1) satisfies the rescaling relation given by (2.27). This scaling is a direct consequence of the fact that the FPE is invariant under the transformation  $\delta x \rightarrow \delta x \tau^{-\alpha}$  and  $P \rightarrow P \tau^{\alpha}$ .

It can be shown (see Appendix A) that equations (2.27) and (6.1) combined with power law scaling of the transport coefficients  $A(\delta x)$  and  $B(\delta x)$  lead to the following equation for the PDF:

$$\frac{\partial P}{\partial \tau} = \frac{\partial}{\partial(\delta x)} \left[ (\delta x)^{1-1/\alpha} \left( a_0 P + b_0 \delta x \frac{\partial P}{\partial(\delta x)} \right) \right]. \quad (6.2)$$

In (6.2)  $a_0$  and  $b_0$  are constants,  $\alpha$  is the scaling index derived from the data and  $P(\delta x)$  and  $\delta x$  are unscaled PDF and fluctuations respectively. Written in this form, equation (6.2) immediately allows us to identify the functional form of the diffusion coefficient, namely  $D(\delta x) \propto (\delta x)^{2-1/\alpha}$ . In Appendix A, we show how (6.2) can be also expressed as:

$$\frac{b_0}{a_0}(\delta x_s) \frac{dP_s}{d(\delta x_s)} + P_s + \frac{\alpha}{a_0}(\delta x_s)^{1/\alpha} P_s = C. \quad (6.3)$$

The partial differential equation (6.3) can be solved analytically and one arrives at the general solution in the form:

$$P_s(\delta x_s) = \frac{a_0}{b_0} \frac{C}{|\delta x_s|^{a_0/b_0}} \exp \left( -\frac{\alpha^2}{b_0} (\delta x_s)^{1/\alpha} \right) \int_0^{\delta x_s} \frac{\exp \left( \frac{\alpha^2}{b_0} (\delta x'_s)^{1/\alpha} \right)}{(\delta x'_s)^{1-a_0/b_0}} d(\delta x'_s) + k_0 H(\delta x_s), \quad (6.4)$$

where  $k_0$  is a constant and  $H(\delta x_s)$  is the homogeneous solution:

$$H(\delta x_s) = \frac{1}{(\delta x_s)^{a_0/b_0}} \exp \left( -\frac{\alpha^2}{b_0} (\delta x_s)^{1/\alpha} \right). \quad (6.5)$$

We then attempt to fit the predicted solution (6.4) to the normalized rescaled PDFs. The results of such a fit for the fluctuations of the kinetic energy density PDF is shown in the figure 6.10 (solid line). This fit is obtained with the following parameters  $a_0/b_0 = 2.0$ ,  $b_0 = 10$ ,  $C = 0.00152$ ,  $k_0 = 0.0625$  and  $\alpha = 0.41$  as derived from the rescaling procedure. We note that the figure is a semi-log plot and emphasizes the tails of the distribution. For a different value of the ratio  $a_0/b_0$ , the fit around the smallest fluctuations could be improved. Equation (6.4) can not, however, properly model the smallest fluctuations as it diverges for  $\delta x_s \rightarrow 0$ .

Let us now assume that a Langevin equation in the form

$$\frac{d(\delta x)}{dt} = \beta(\delta x) + \gamma(\delta x)\xi(t) \quad (6.6)$$

can describe the dynamics of the fluctuations. In (6.6) the random variable  $\xi(t)$  is assumed to be  $\delta$ -correlated, i.e.,

$$\langle \xi(t)\xi(t+\tau) \rangle = \sigma^2\delta(\tau). \quad (6.7)$$

This condition is fulfilled in the data analysis by forming each time series  $\delta x(t, \tau)$  with non-overlapping time intervals  $\tau$  and was also verified by computing the autocorrelation function of the differenced time series. Introducing a new variable,  $z = \int_0^{\delta x} 1/\gamma(\delta x')d(\delta x')$ , equation (6.6) can be written as:

$$\frac{dz}{dt} = \frac{\beta(z)}{\gamma(z)} + \xi(t). \quad (6.8)$$

One can immediately obtain a F-P equation that corresponds to the Langevin equation (6.8) (*van Kampen*, 1992). We can then compare this FPE with that given by (6.2) to express coefficients  $\beta(\delta x)$  and  $\gamma(\delta x)$  in terms of  $a_0$  and  $b_0$  (see Appendix B). Defining  $D_0 = \langle \xi^2(t) \rangle / 2$  we obtain:

$$\gamma(\delta x) = \sqrt{\frac{b_0}{D_0}}(\delta x)^{1-\frac{1}{2\alpha}}, \quad (6.9)$$

and

$$\beta(\delta x) = [b_0(1 - \frac{1}{2\alpha}) - a_0](\delta x)^{1-\frac{1}{\alpha}}. \quad (6.10)$$

Equation (6.6) together with definitions of its coefficients (6.9) and (6.10) constitutes a dynamical model for the fluctuations in the solar wind quantities. From (6.9) and (6.10), we see that the diffusion of the PDF of fluctuations in the solar wind is of comparable strength to the advection ( $a_0/b_0 \approx 2$ ). We stress that the advection and diffusion processes that we discuss here are of the probability in parameter space for fluctuations and do not refer to the integrated quantities.

### 6.5.2 Castaing model

We now, for comparison, consider a model motivated directly by a cascade in energy, that is, the Castaing model. This empirical model was developed for the spatial velocity fluctuations recorded from controlled experiments in wind tunnels (*Castaing*

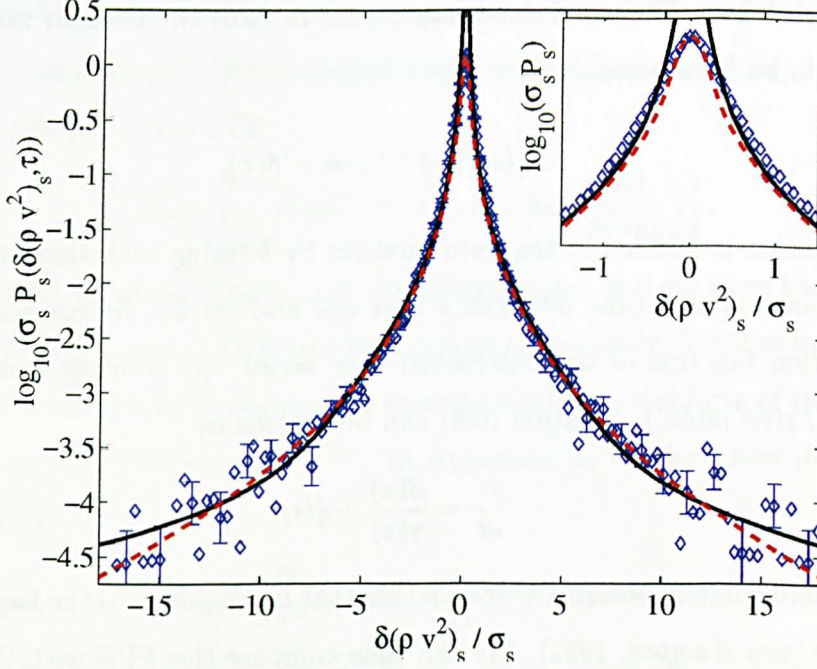


Figure 6.10: Example of the fit of the PDF functional form predicted by a Fokker-Planck description (6.4) (solid line) and a Castaing model (dash line) to the fluctuations PDF of the  $\delta(\rho v^2)$  bulk parameter.

*et al.*, 1990; *van Atta and Park*, 1972). The underlying idea of this approach is that, for constant energy transfer rate between spatial scales, all quantities should exhibit a Gaussian distribution of fluctuations. The intermittency is then introduced to the PDF through the fluctuations of the variance  $\sigma$  of that Gaussian distribution. A log-normal distribution is assumed for the variance  $\sigma$ :

$$Q(\sigma) = \frac{1}{\sqrt{2\pi\lambda}} \exp\left(-\frac{\ln^2(\sigma/\sigma_0)}{2\lambda^2}\right) d(\ln(\sigma)), \quad (6.11)$$

where  $\sigma_0$  is the most probable variance of the fluctuations and  $\lambda$  is the variance of  $\ln(\sigma)$ . Combining these two hypothesis, Castaing proposed the following functional form for the observed PDF:

$$P_\lambda(\delta x) = \frac{1}{2\pi\lambda} \int_0^\infty \exp\left(-\frac{(\delta x)^2}{2\sigma^2}\right) \exp\left(-\frac{\ln^2(\sigma/\sigma_0)}{2\lambda^2}\right) \frac{d\sigma}{\sigma^2}. \quad (6.12)$$

The dashed line in the figure 6.10 shows the Castaing curve fitted with parameters  $\lambda = 1.275$  and  $\sigma_0 = 0.225$  to the  $\delta(\rho v^2)$  PDF.

We can now compare the rescaled PDFs with both FPE and Castaing predicted curves which are shown in figure 6.10. We can see from the figure that

both models provide an adequate fit to the  $\delta(\rho v^2)_s$  PDF, and hence will also describe the PDF of other scaling bulk plasma parameters. Both curves, however, fall significantly below observed PDF values for  $|\delta(\rho v^2)_s| \leq 2$ , although the Castaing distribution fits the peak of the PDF very well (see insert in figure 6.10). This departure from the experimental PDF, in the case of the Castaing distribution, may reflect the difference between hydrodynamics and MHD turbulence.

## 6.6 Conclusions

In this section, we have applied a generic PDF rescaling method to fluctuations of the solar wind bulk plasma parameters,  $\epsilon$  parameter that measures the energy flux entering the magnetosphere and geomagnetic indices AU, AL and AE. In the case of the solar wind, we find that, consistent with previous work, magnetic field and velocity magnitudes do not exhibit mono-scaling whereas PDFs of fluctuations in  $B^2$ ,  $\rho$ ,  $\rho v^2$  and  $vB^2$  can be rescaled with just one parameter for temporal scales up to  $\sim 26$  hours (*Hnat et al.*, 2002c). All investigated PDFs show intermittency on these temporal scales. Consequently, their PDFs are leptokurtic and show increased probability of large fluctuations compared to that of the normal distribution. Fluctuations on large temporal scales,  $\tau > 26$  hours, seem to be uncorrelated and their PDFs converge toward a Gaussian. The self-similarity of fluctuations associated with energy densities and Poynting flux is intriguing and suggests a simplifying picture of intermittency in the energy cascade. The fact that all quantities share the same PDF, to within errors, is strongly suggestive of a single underlying process. This is also supported by the similar values of the scaling exponents.

Similar results were found in the investigation of the  $\epsilon$  parameter and the global magnetospheric indices. Firstly, the similar values of the scaling exponent and the leptokurtic nature of the single PDF that, to within errors, describes fluctuations on time scales up to  $\tau_{max}$  in  $\epsilon$  and the indices provide an important quantitative constraint for models of the coupled solar wind-magnetosphere system. One possibility is that, up to  $\tau_{max} \sim 4$  hours, fluctuations in AU and AL are directly reflecting those seen in the turbulent solar wind. The data also suggest that AE index departs

from this scaling on shorter time scale of  $\tau_{max} \sim 2$  hours. Importantly, identifying a close correspondence in the fluctuation PDF of  $\epsilon$ , AE, AU and AL may simply indicate that fluctuations in the indices are strongly coupled to dayside processes and are thus weak indicators of the fluctuations in nightside energy output. We stress, however, that practically an approximate collapse of PDFs is an indicator of a dominant mono-fractal trend in the time series, i.e., this method may not be sensitive enough to detect multi-fractality that could be present only during short time intervals. It is then possible that our method simply detects a dominant mono-fractal component in the time series associated with the solar wind energy input into magnetosphere, while the magnetospheric processes, such as turbulent reconnection, may contribute only during short time intervals.

We also presented a Fokker-Planck approach that allowed us to obtain a functional form of the rescaled PDFs and a Langevin equation for the dynamics of the observed fluctuations in the solar wind. The model shows that both advective and diffusive transport need to be invoked to describe the dynamics of the fluctuations. The presence of the advective term in our FPE means that the probability of finding fluctuations of a given size grows linearly in time. We are currently exploring different physical process (11 years solar cycle, for example) that could provide such mechanism in nature. The calculated diffusion coefficient is of the form  $D(x_s) \propto (\delta x_s)^{2-1/\alpha}$ . We obtained a good fit of the model to our rescaled PDFs over at least 10 standard deviations. We also examined a Castaing model and found a set of fit parameters for which both Castaing distribution and our diffusion model have nearly identical form. Since both FPE model and Castaing distribution fit our rescaled PDFs in the similar fashion we conclude that their moments should exhibit same variation with time lag  $\tau$ .

And last but not least, this work confirms that statistical intermittency of the PDF can be accompanied by the statistical self-similarity of the fluctuations. Previously it was found that such behavior is possible if the fluctuations are treated as random variables with a Lévy distribution. Here, we find similar behavior for the scaling indices that are subdiffusive and well outside the Lévy range.

## Chapter 7

# Conclusions

In this work, two alternative approaches to scaling phenomena in space and laboratory plasma have been explored. Confined plasma systems exhibit complex dynamics that can not be easily described by equations of motion. This complexity arises as a result of strong coupling between processes occurring on many spatial and temporal scales, all equally relevant to the behavior of the system. Statistical features of complex systems can emerge as a unifying and simplifying aspect of their behavior. Among them, scaling—a direct consequence of the lack of a characteristic spatial or temporal scale—is one of the fundamental characteristics of complex systems.

### 7.1 Conclusions from the sandpile model study

The first approach to scaling considered here was an avalanching sandpile model. This model, described in details in Chapter 2, has a single control parameter  $L_f/N$  that allows us to study its dynamics in a critical state as well as away from it. Although the basic dynamical rules, prescribed in the numerical algorithm, are quite simple the emergent behavior of the system is complex. In the course of this study, we have used advanced visualization methods for qualitative studies of the model as well as quantitative time series analysis techniques (*Hnat and Chapman, 2000*).



### 7.1.1 Qualitative results

Advanced Virtual Reality visualization software, used for qualitative studies of the sandpile behavior, has been presented in Chapter 3. There, we have discussed algorithms for data reduction and surface optimization applied in the software as well as results obtained from the visualization. We have analyzed two different surface optimization methods—triangulated irregular network (TIN) algorithm (*Chow*, 1997; *Lindstrom and Turk*, 1998) and a level of detail (LOD) algorithm introduced in *Lindstrom et al.* (1994). We concluded that the LOD method is much more efficient for multi-scale visualization when fast responses to user's interrupts are also required. We emphasize that problems encountered during the development of this VR software are generic problems in visualization of large multi-scale (fractal) structures. Algorithms developed for our software can be used to optimize any three-dimensional structure with large number of detail. They are especially suitable for scientific data as one can control the level of information lost during the optimization process.

When applied to 3D sandpile height profiles, this method allowed us to select a region of interest, in space and time, and explore the trends, otherwise hidden among the vast amounts of data. The following list presents qualitative results obtained from the visualization:

1. In the case of  $L_f = N$  and constant critical gradient, a self-similar character of the total energy time series corresponds to a self-similar pattern of the height profile (see figure 2.5(a,b)). This also confirmed already known results published in *Helander et al.* (1999).
2. In the case of  $L_f = N$  and 2% randomization of the critical gradient, long internal avalanches appear as seen in figure 2.6(a,b).
3. In the case of  $L_f \ll N$ , two distinctive regions of behavior can be identified. A growth phase, with characteristic step-like features, is followed by a relaxation phase where systemwide avalanches lead to many clustered energy dissipation events. During this relaxation phase, the edge of the sandpile is retracted back

whereas during the growth phase the edge is always positioned at the last cell of the grid.

4. In the case of  $L_f \ll N$ , the continuous fueling at the cell  $n = 1$  affects region within distance  $\sim L_f$  cells. This region always exhibits features characteristic of  $L_f = N$  case.

This observations were used extensively during the development of a tokamak-like sandpile model discussed in Chapter 5.

### 7.1.2 Quantitative results

In Chapter 4, we investigated scaling of the sandpile model for the critical and near critical regime. Three different techniques have been used to characterize the scaling and to identify length scales where the scale break occurs in various cases. First, we applied a finite size scaling method to investigate the scaling of avalanche length and dissipated energy probability distributions for the critical system. We found that the avalanche length distribution exhibits a finite size scaling for the system with  $L_f = N$ . The scaling exponent obtained from this scaling is  $\alpha = -1$ . The dissipated energy PDIF, however, does not exhibit a finite size scaling and we then used a multi-scaling ansatz to collapse PDIFs from systems of different sizes  $N$ . This procedure suggests two dominant scaling regimes with  $\alpha_1 = -0.65 \pm 0.04$  for the small scale events and  $\alpha_2 = -0.93 \pm 0.05$  for the large dissipated energies. The scaling index  $\alpha_2$  is consistent with that reported previously in *Tam et al. (1999)* where the RG method was used. We also found that a multi-fractal approach needs to be applied to obtain a satisfactory collapse of all PDIFs for the near critical system. In this case, when  $L_f = N/2$ , we used multi-fractal ansatz (2.38) and found the scaling index for the avalanche length is still  $-1$ , in the region where the clear power law can be identified. Scaling of the dissipated energy PDIFs resembles closely that found in the case of  $L_f = N$  with indices yielding the same values, within error bars. Interestingly, the statistical features of the dissipated energy data are very similar for both cases with  $L_f = N$  and  $L_f = N/2$ . These results also

highlight the difficulties in quantifying the proximity of the physical system to its fixed point. Values of scaling indices obtained here suggest that this sandpile model does not belong to any known universality class.

Geometrical features of the time series are sometimes used to quantify scaling characteristics of a physical process. In Chapter 4, we have obtained, analytically, the fractal dimension of the total energy time series for the system with  $L_f = N$  and constant critical gradient. Our method is based on the scaling of the length of a given curve with the size of the ruler. This result shows that the curve itself is self-similar and has a trivial fractal dimension of 1. The result is obtained in the limit of the system size  $N \rightarrow \infty$ . For the finite size physical system, where size  $N$  is fixed, this condition can be approximated only when the resolution of experimental measurements is infinitely high. Such observations would allow us to sample all relevant scales of the curve. We then discussed the impact of the finite resolution measurements on the determination of the fractal dimension of the time series curve. We also performed numerical studies of the curve length scaling for the system with different values of  $L_f$  and with randomized critical gradient. We found that the fractal dimensions of all the investigated curves were close to 1. We note, mathematically, intriguing form of the mutual information curve for the system with constant critical gradient and  $L_f = N$  (see figure 4.10(a)). This curve closely resembles a Weierstrass function given by:

$$W(x) = \sum_{n=0}^{\infty} b^n \cos(a^n \pi x), \quad (7.1)$$

where  $a$  is an odd number,  $b \in (0, 1)$  and  $ab > 1 + 3\pi/2$ . This function, just like the total energy trace, is continuous but not differentiable at any point.

Finally, we performed a phase space reconstruction of the sandpile dynamics and quantified the complexity of the phase space structures. A correlation sum was obtained for every structure and a correlation fractal dimension was then estimated. For the system with constant critical gradient we were able to differentiate between critical and near critical system. Estimates of their fractal dimensions were different with high confidence level of 95%. We have also found a nontrivial value of  $d_2 =$

$1.33 \pm 0.02$  for the system with  $L_f = 48 \ll N$  and constant critical gradient. Interestingly, when the 2% randomization of the critical gradient was considered, estimates of the fractal dimension for the critical and near critical system gave identical values of  $d_2 = 1.14 \pm 0.02$ , to within errors. This result is supported by the character of the phase space structures that are very similar for these two cases (see figure 4.9(d,e)). We found that the scaling of the correlation sum is destroyed by added randomization for small value of  $L_f = 48$ . In that case, we are only able to identify edges of the distinctive dynamical regions that may, perhaps, correspond to a growth and a relaxation phases of the sandpile cycle.

### 7.1.3 Application of the sandpile model

In Chapter 5, we have shown how close phenomenological parallels can be identified between our sandpile and the tokamak plasma behavior. Extensive discussion of our results was given in the Conclusions of Chapter 5. We provide a list of major results obtained from that study.

1. Distinctive features, such as steep edge gradients, edge localized modes, low and high confinement regimes and internal transport barriers, seen in tokamak plasmas can also arise in a simpler idealized confinement system and they may be linked to the observed avalanching transport phenomena.
2. Correlations between stored energy, confinement times, sandpile profile, sandpile edge structure and the amplitude, frequency and dynamical character of mass loss events are very similar to these found in tokamak plasma.
3. If a single control parameter analogous to  $L_f/N$  exists for tokamaks, it can, in principle, be found from experimental data by examining scaling with respect to system size.
4. The low confinement mode is equivalent to a critical state of the system with no characteristic spatial scale. The H-mode or the high confinement mode arises when the rapid systemwide transport has been suppressed. This corresponds to small values of  $L_f$  parameter in the sandpile. In such case, a number of

transport barriers emerge within the system allowing for an increased amount of energy to be stored.

5. Transition between L-mode and H-mode can be achieved by smooth evolution of the control parameter.

The results of this investigation should be considered in a wider context of a search for a minimal set of physical principles that underline complex tokamak plasma behavior. In the absence of the fully developed theory of turbulence in plasma and considering the lack of long, stationary experimental observations identifying simple model, whose phenomenology closely resembles that of tokamak plasma is very important (*Krommes*, 2002). We also stress that a number of recent observations confirmed the existence of rapid radial avalanching transport in tokamak (*Rhodes et al.*, 1999; *Politzer*, 2000). The results further suggest a test of the depth of the physical analogy that we have found, as follows. If the analogy is deep, there will exist one or a few dimensionless control parameters, linked to the properties of the turbulent transport, that entirely determine the key features of the confinement phenomenology. For example, these parameters would control the extent to which global confinement is entrained to edge pedestal dynamics. The search for such parameters, for example by further application of the techniques of nonlinear time series analysis to edge plasma measurements as initiated in *Pedrosa et al.* (1999), is potentially highly rewarding.

## 7.2 Conclusions from the finite size scaling and a Fokker-Planck approach to space plasmas

In Chapter 6, we have applied a finite size scaling, described in Section 2.2, to two space plasma systems—the solar wind and the coupled solar wind-magnetosphere system (*Hnat et al.*, 2002a,b). The method used in this investigation is generic and model independent. It allows us to identify quantities that exhibit statistical mono-scaling. Interestingly, such mono-scaling can coexist with statistical intermittency defined as the existence of the very large events as compared to the average.

Scaling indices derived from this method can be treated as a measure of this intermittency that is also exhibited as a departure of the PDF from a Normal distribution. And last but not least, the method allows us to directly compare the PDFs for different investigated quantities and develop a diffusion based model of the PDF dynamics.

### 7.2.1 Solar wind fluctuations

In the case of the solar wind, we have identified four quantities whose fluctuations exhibit mono-scaling for temporal scales up to  $\sim 26$  hours. Their PDFs are leptokurtic and show increased probability of large fluctuations, compared to that of the normal distribution. Fluctuations on large temporal scales,  $\tau > 26$  hours, seem to be uncorrelated and their PDFs converge toward a Gaussian. The self-similarity of fluctuations associated with energy densities and Poynting flux is intriguing and suggests a simplifying picture of intermittency in the energy cascade. It indicates that, on average, the energy transfer rate is a constant from one scale to the next. This, in turn, implies that the energy cascade, in terms of these quantities, is self-similar. This self-similarity should be reflected in the plasma fluid equations, when written in terms of these mono-scaling quantities.

In recent years, two alternative paradigms have been proposed for the origin of the solar win fluctuations (*Dobrowolny et al.*, 1980). The first approach assumes that the solar wind is a passive medium and observed fluctuations are low-frequency Alfvén waves that originated at the solar corona. This is supported by observations that over 90% of these fluctuations are consistent with pure Alfvén waves (*Horbury and Schmidt*, 1999). The second paradigm treats the solar wind as an active highly nonlinear system with fluctuations arising in situ in manner similar to that of hydrodynamic turbulence (*Goldstein and Roberts*, 1999). Single point measurements can not uniquely determine which mechanism is dominant. Indeed, to verify that the observations are consistent with the turbulence theory, for example, ideally one needs to study a structure function constructed from a range of spatial locations in the plasma. However, single point data taken over long intervals in the solar wind

can yield strongly suggestive results as we have shown in Chapter 6.

The results of the PDF rescaling analysis are consistent with underlying turbulent process generating the fluctuations. We have illustrated this by fitting a Castaing distribution (*Castaing et al.*, 1990) to the rescaled PDFs. We have also shown, however, that a simpler diffusive model can be developed to approximate observed PDFs with the same accuracy. Such a diffusive model, operating in the probability space of the observed fluctuations, may have certain advantages over turbulent models. For example, one can derive a corresponding Langevin equation for such model that allows one to generate a time series of the fluctuations with statistical properties identical to that observed in the solar wind.

### 7.2.2 Coupled solar wind-magnetosphere system

Results of this investigation strongly suggest that geomagnetic indices are measures of the dayside processes associated with the solar wind coupling to the Earth magnetic field. This is strongly supported by the identical values of the scaling indices as well as the similar shape of the rescaled PDF curves. The results also shed new light on the reconnection processes occurring on the dayside. Assuming that all energy input given by  $\epsilon$  from (1.15) comes from the reconnection type processes our results suggest that these processes are relevant on all temporal scales up to  $\sim 4$  hours. The geomagnetic indices are often considered a measure of activities in the Earth magnetosphere. Our research, however, does not confirm that. A possible explanation of this results could lie in bursty and rapid character of these activities. As we pointed out in Chapter 6, our method may not be sensitive enough to detect short multi-fractal components in the time series.

### 7.2.3 Results from the Fokker-Planck model

A dynamical model of the solar wind fluctuations has been presented in Chapter 6. This model allowed us to obtained transport coefficients for the fluctuations. In particular we have identified a diffusion coefficient to be of the form  $D(x_s) \propto (\delta x_s)^{2-1/\alpha}$ . The model also gives an estimated functional form of the rescaled PDF

curve. We used this function to fit the PDFs over at least 10 standard deviations. The fit is satisfactory everywhere, except for the peaks of the distribution where our solution diverges. We have compared our model with that of *Castaing et al.* (1990) and we have concluded that both can approximate our PDFs quite well. Since both F-P model and Castaing distribution fit our rescaled PDFs in the similar fashion we conclude that their moments should exhibit same variation with time lag  $\tau$ . We have also demonstrated that a Langevin equation can be derived from our model (*Hnat et al.*, 2002c).

### 7.3 Future work

- Observations from tokamaks are difficult to analyze as they often incorporate measurements from different modes of operation. Average confinement time in JET is about 1 second and during the measurement a transition between L-mode and H-mode often occurs. Providing that a satisfactory (long and stationary) data set can be obtained, future work should concentrate on identifying scaling properties of the tokamak plasma and the dimensionality of the dynamics in different modes. Prediction from our sandpile study is that L-mode dynamics should be high dimensional (SOC like) whereas H-mode should exhibit low dimensionality.
- Mono-scaling of the solar wind fluctuation for quantities investigated in Chapter 6 extends to maximum temporal scale of  $\sim 26$  hours. It is an open question why we do not detect a scale break for the temporal scales where coherent structures become dominant. Studies of fluctuations from the solar region (corona) could shed some light on this interesting issue.
- Further research of space plasmas could also include analysis of the spatial data. This could be facilitated by obtaining measurements from few spacecraft (WIND, ACE, CLUSTER II) and should provide a point of contact with analytical turbulence studies where results are given in terms of the spatial quantities (structure functions).



- Analytical studies could focus on determining the connection between mono-scaling found for energy densities of solar wind fluctuations and MHD equations for the plasma. A Fokker-Planck equation, obtained for the rescaled PDF, can be solved numerically with given initial and boundary conditions.

## Appendix A

# Fokker-Planck model of solar wind fluctuations

Let  $P(\delta x, \tau)$  be a homogeneous function that satisfies scaling (2.27). Our aim is to find functional form of the coefficients  $A(\delta x)$  and  $B(\delta x)$  for which  $P(\delta x, \tau)$  is a solution of a F-P equation (6.1). Using (2.27) we can now rewrite (6.1) to read:

$$\begin{aligned} -\frac{\alpha}{t^{\alpha+1}} \left( P_s + \delta x_s \frac{dP_s}{d(\delta x_s)} \right) &= \frac{P_s}{t^\alpha} \frac{dA(\delta x)}{d(\delta x)} + \frac{A(\delta x)}{t^{2\alpha}} \frac{dP_s}{d(\delta x_s)} \\ &+ \frac{1}{t^{2\alpha}} \frac{dB(\delta x)}{d(\delta x)} \frac{dP_s}{d(\delta x_s)} + \frac{B(\delta x)}{t^{3\alpha}} \frac{dP_s}{d(\delta x_s)}. \end{aligned} \quad (\text{A.1})$$

If all terms in the rhs of (A.1) are to contribute and for  $P(\delta x_s)$  to remain a function of  $\delta x_s$  only we must have:

$$\frac{A(\delta x)}{t^{\alpha-1}} = a(\delta x_s) \quad \text{and} \quad \frac{B(\delta x)}{t^{2\alpha-1}} = b(\delta x_s). \quad (\text{A.2})$$

Both  $A(\delta x)$  and  $B(\delta x)$  must then be of form:

$$A(\delta x) = a_0(\delta x)^\eta \quad \text{and} \quad B(\delta x) = b_0(\delta x)^\nu, \quad (\text{A.3})$$

where  $a_0$  and  $b_0$  are constants. Changing variables to the rescaled  $\delta x_s$  and substituting (A.3) into (A.2) we express exponents  $\eta$  and  $\nu$  in terms of the rescaling index  $\alpha$  derived from the data. We then get:

$$\eta = 1 - \frac{1}{\alpha} \quad \text{and} \quad \nu = 2 - \frac{1}{\alpha}, \quad (\text{A.4})$$

which allows to write the final power law form of  $A(\delta x)$  and  $B(\delta x)$ :

$$A(\delta x) = a_0(\delta x)^{1-\frac{1}{\alpha}} \quad \text{and} \quad B(\delta x) = b_0(\delta x)^{2-\frac{1}{\alpha}}. \quad (\text{A.5})$$

Substituting these expressions into F-P equation (6.1) we obtain (6.2) from Section

4. Using these results the term  $\frac{dA(\delta x)}{d(\delta x)}$  on the rhs of (A.1), for example, becomes:

$$\frac{dA(\delta x)}{d(\delta x)} = \left(1 - \frac{1}{\alpha}\right) a_0(\delta x)^{-\frac{1}{\alpha}}. \quad (\text{A.6})$$

Performing similar algebra on all terms in (A.1) we arrive to equation:

$$-\alpha \frac{d(\delta x_s P_s)}{d(\delta x_s)} = \frac{d}{d(\delta x_s)} \left[ (\delta x_s)^{1-\frac{1}{\alpha}} \left( a_0 P_s + b_0(\delta x_s) \frac{dP_s}{d(\delta x_s)} \right) \right]. \quad (\text{A.7})$$

Integrated once trivially we obtain equation (6.3)

$$\frac{b_0}{a_0}(\delta x_s) \frac{dP_s}{d(\delta x_s)} + P_s + \frac{\alpha}{a_0}(\delta x_s)^{\frac{1}{\alpha}} dP_s = C, \quad (\text{A.8})$$

where  $C$  is the constant of integration.

## Appendix B

# Langevin equation for solar wind fluctuations

Consider the following Langevin type of equation:

$$\frac{d(\delta x)}{dt} = \beta(\delta x) + \gamma(\delta x)\xi(t), \quad (\text{B.1})$$

where the random variable  $\xi(t)$  is assumed to be  $\delta$ -correlated, i.e.,

$$\langle \xi(t)\xi(t+\tau) \rangle = \sigma^2\delta(\tau). \quad (\text{B.2})$$

Introducing a new variable  $z = \int_0^{\delta x} 1/\gamma(\delta x')d(\delta x')$ , equation (B.1) can be written as:

$$\frac{dz}{dt} = \Gamma(z) + \xi(t), \quad \text{where} \quad \Gamma(z) = \frac{\beta(z)}{\gamma(z)}. \quad (\text{B.3})$$

One can immediately obtain a F-P equation that corresponds to the Langevin equation (B.3) and reads:

$$\frac{\partial P(z, \tau)}{\partial \tau} + \frac{\partial}{\partial z} (\Gamma(z)P(z, \tau)) = D_0 \frac{\partial^2 P(z, \tau)}{\partial^2 z}, \quad (\text{B.4})$$

where  $D_0 = \sigma^2/2$ . The probability is an invariant of the variable change so that  $P(\delta x)d(\delta x) = P(z)dz$  and we can then rewrite (B.4) for  $P(\delta x, \tau)$ :

$$\frac{\partial P}{\partial \tau} = \frac{\partial}{\partial(\delta x)} \left[ \left( D_0 \gamma(\delta x) \frac{d\gamma(\delta x)}{d(\delta x)} - \beta(\delta x) \right) P + D_0 \gamma^2 \frac{\partial P}{\partial(\delta x)} \right]. \quad (\text{B.5})$$

Comparing (B.5) with the F-P equation (6.2) we can identify:

$$D_0 \gamma^2 = (\delta x)^{1-\frac{1}{\alpha}} b_0 \delta x, \quad (\text{B.6})$$

and then we must demand that:

$$\frac{D_0}{2} \frac{d\gamma^2(\delta x)}{d(\delta x)^2} - \beta(\delta x) = a_0 (\delta x)^{1-\frac{1}{\alpha}}. \quad (\text{B.7})$$

In summary we have shown that the F-P equation given by (6.2) is equivalent to the stochastic Langevin equation (6.6) where coefficients  $\beta$  and  $\gamma$  are given by:

$$\gamma = \sqrt{\frac{b_0}{D_0}} (\delta x)^{1-\frac{1}{2\alpha}}, \quad (\text{B.8})$$

and

$$\beta = \left[ b_0 \left( 1 - \frac{1}{2\alpha} \right) - a_0 \right] (\delta x)^{1-\frac{1}{\alpha}}. \quad (\text{B.9})$$

# Bibliography

- Amaral, Luis A. Nunes and Kent Bækgaard Lauritsen, Universality classes for rice-pile models, *Phys. Rev. E* **56**, 231–234, 1997.
- Angelopoulos, V. *et al.*, Bursty bulk flows in the inner central plasma sheet, *J. Geophys. Res.* **59**, 4027–4039, 1992.
- Bak, P., C. Tang and K. Weisenfeld, Self-organized criticality: An explanation of the  $1/f$  noise, *Phys. Rev. Lett.* **59**, 381–384, 1987.
- Barnsley, M. F., R. L. Devaney, B. B. Mandelbrot, H. O. Peitgen, D. Saupe, R. F. Voss, *The Science of Fractal Images*, Springer-Verlag, NY, 1988.
- Biskamp, D., *Nonlinear Magnetohydrodynamics*, Cambridge Monographs on Plasma Physics 1, Cambridge, 1993.
- Bohr, T., M. H. Jensen, G. Paladin and A. Vulpiani, *Dynamical Systems Approach to Turbulence*, Cambridge University Press, Cambridge, 1998.
- Burlaga, L.F., Lognormal and multifractal distributions of the heliospheric magnetic field, *J. Geophys. Res.* **106**, 15,917–15,927, 2001.
- Burrell, K. H. *et al.*, Effects of  $E \times B$  velocity shear and magnetic shear in the formation of core transport barriers in the DIII-D tokamak, *Plasma Phys. Control. Fusion* **40**, 1585, 1998.
- Caan, M. N., R. L. McPherron, and C. T. Russell, The statistical magnetic signature of magnetospheric substorms, *Planet. Space Sci.* **26**, 269, 1978.

- Carbone, Vincenzo, Pierluigi Veltri and Roberto Bruno, Experimental Evidence for Differences in the Extended Self-Similarity Scaling Laws between Fluid and Magnetohydrodynamic Turbulent Flows, *Phys. Rev. Lett.* **75**, 3110–3113, 1995.
- Carreras, B. A., D. Newman, V. E. Lynch, and P. H. Diamond, A model realization of self-organized criticality for plasma confinement, *Phys. Plasmas* **3**, 2903–2911, 1996.
- Carreras, B. A., V. E. Lynch, P. H. Diamond and M. Medvedev, On the stiffness of the sand pile profile, *Phys. Plasmas* **5**, 1206–1208, 1998.
- Castaing, B., Y. Gagne and E. J. Hopfinger, Velocity Probability Density Functions of High Reynolds Number Turbulence, *Physica D* **46**, 177–200, 1990.
- Chang T., Low-dimensional Behavior and Symmetry Breaking of Stochastic Systems Near Criticality: Can these Effects be Observed in Space and in the Laboratory?, *IEEE Trans. Plasma Sci.* **20**, 691, 1992.
- Chang T., Self-organized criticality, multi-fractal spectra, sporadic localized reconnections and intermittent turbulence in the magnetotail, *Phys. Plasmas* **6**, 4137–4145, 1999.
- Chapman, S. C., R.O. Dendy, G. Rowlands, A sandpile model with dual scaling regimes for laboratory, space and astrophysical plasmas, *Phys. Plasmas* **6**, 4169–4177, 1999.
- Chapman, S. C., Inverse cascade avalanche model with limit cycle exhibiting period doubling, intermittency, and self-similarity, *Phys. Rev. E* **62**, 1905–1911, 2000.
- Chapman, S. C. and N. W. Watkins, Avalanching and Self Organised Criticality: a paradigm for magnetospheric dynamics?, *Space Sci. Rev.* **95**, 293, 2001.
- Chapman, S. C., R. O. Dendy, B. Hnat, A simple avalanche model for astrophysical and laboratory confinement systems, *Phys. Plasmas* **8**, 1969, 2001.
- Chapman, S.C., R. O. Dendy, B. Hnat, A sandpile model with tokamak-like enhanced confinement phenomenology, *Phys. Rev. Lett.* **86**, 2814, 2001.

- Chechkin, A. V., and V. Yu. Gonchar, A model for persistent Levy motion, *Physica A* **277**, 312–326, 2000.
- Chen, K., P. Bak and S.P. Obukov, Self-organized criticality in a crack-propagation model of earthquakes, *Phys. Rev. A* **43**, 625–630, 1991.
- Chow, M. M., Optimized Geometry Compression for Real-Time Rendering, *Proceedings of the IEEE Visualization '97*, 1997.
- Clemmow, P. C. and J. P. Dougherty, *Electrodynamics of particles and plasmas*, Advanced Book Classics, Addison-Wesley Publishing Co., Inc., Canada, 1990.
- Conway G. D. *et al.*, Suppression of Plasma Turbulence During Optimized Shear Configurations in JET, *Phys. Rev. Lett.* **84**, 1463–1466, 2000.
- Consolini, G., M. F. Marcucci, M. Candidi, Multifractal structure of auroral electrojet index data, *Phys. Rev. Lett.* **76**, 4082–4085, 1996.
- Consolini, G., and P. De Michelis, Non-Gaussian distribution function of AE-index fluctuations: Evidence for time intermittency, *Geophys. Res. Lett.* **25**, 4087–4090, 1998.
- Consolini, G., and T. Chang, Complexity, magnetic field topology, criticality, and metastability in magnetotail dynamics, *J. Atmos. Sol.-Terr. Phys.* **64**, 541–549, 2002.
- Crutchfield, J. P. and B. S. McNamara, Equations of motion from a data series, *Complex Systems* **1**, 417, 1987.
- Crutchfield, J. P. and K. Young, Inferring statistical complexity, *Phys. Rev. Lett.* **63**, 105, 1989.
- Davis, T. N., and M. Sugiura, Auroral electrojet activity index *AE* and its universal time variations, *J. Geophys. Res.* **71**, 785–801, 1966.
- Dendy, R. O. and P. Hallender, Sandpiles, silos and tokamak phenomenology: a brief review, *Plasma Phys. Control. Fusion* **39**, 1947–1961, 1997.



- Dendy, R. O., P. Hallender and M. Tagger, On the role of self-organised criticality in accretion systems, *Astron. Astrophys.* **337**, 962–965, 1998.
- Diamond, P. H. and T. S. Hahm, On the dynamics of turbulent transport near marginal stability, *Phys. Plasmas* **2**, 3640–3649, 1995.
- Dobrowolny, M., A. Mangeney and P. Veltri, Fully Developed Anisotropic Hydro-magnetic Turbulence in Interplanetary Space, *Phys. Rev. Lett.* **45**, 144–147, 1980.
- Fishpool, G. M., Loss of confinement due to reduction of the edge pedestal in JET, *Nucl. Fusion* **38**, 1373–1380, 1998.
- Forman, M. A. and L. F. Burlaga, Exploring the Castaing Distribution Function to Study Intermittency in the Solar Wind at L1 in June 2000, *AIP Conference Proceedings*, Woodbury, NY, 1087–1090, 2000.
- Fraser, A. and H. Swinney, Independent coordinates for strange attractors from mutual information, *Phys. Rev. A* **33**, 1134–1140, 1986.
- Freeman, M. P., N. W. Watkins and D. J. Riley, Evidence for a solar wind origin of the power law burst lifetime distribution of the AE indices, *Geophys. Res. Lett.* **27**, 1087–1090, 2000.
- Freeman, M. P., N. W. Watkins and D. J. Riley, Power law distribution of burst duration and interburst interval in the solar wind: Turbulence or dissipative self-organized criticality, *Phys. Rev. E* **62**, 8794–8797, 2000.
- Frisch U., *Turbulence. The legacy of A.N. Kolmogorov*, Cambridge University Press, Cambridge, 1995.
- Garbet X. and R. Waltz, Heat flux driven ion turbulence, *Phys. Plasmas* **5**, 2836–2845, 1998.
- Goldstein, M. L. and D. A. Roberts, Magnetohydrodynamic Turbulence in the solar wind, *Phys. Plasmas* **6**, 4154–4160, 1999.

- Gopikrishnan, P., V. Plerou, L. A. Nunes Amaral, M. Meyer and H. E. Stanley, Scaling of the distribution of fluctuations of financial market indices, *Phys. Rev. E* **60**, 5305–5316, 1999.
- Grassberger, P. and L. Procaccia, Measuring the strangeness of strange attractors, *Physica D* **9**, 189–208, 1983.
- Haken H., *Synergetics. An Introduction; Nonequilibrium Phase Transition and Self-Organization in Physics, Chemistry and Biology*, Springer-Verlag, Berlin, 1978.
- Halsey, T. C., H. Jensen, L. P. Kadanoff, I. Procaccia and B. I. Shraiman, Fractal measures and their singularities: The characterization of strange set, *Phys. Rev. A* **33**, 1141–1151, 1986.
- Helander, P., S. C. Chapman, R. O. Dendy, G. Rowlands and N. W. Watkins, Exactly solvable sandpile with fractal avalanching, *Phys. Rev. E* **59**, 6356–6360, 1999.
- Hentschel, H. G. E., and I. Procaccia, Relative diffusion in turbulent media: The fractal dimension of clouds, *Phys. Rev. A* **29**, 1461–1471, 1984.
- Hicks, H. R. and B. A. Carreras, Quasicoherent fluctuations associated with a transport barrier in the sandpile model, *Phys Plasmas* **8**, 3277–3281, 2001.
- Hnat, B. and S. C. Chapman, Visualization of multi-scale datasets in numerical models of complex systems, *CIDAC* **2**, 235, 2000.
- Hnat, B., S. C. Chapman, A. Ynnerman, Virtual Reality as a tool for exploring astrophysical systems, Proc ICPP, 2000.
- Hnat, B., S. C. Chapman, G. Rowlands, N. W. Watkins, W. M. Farrell, Finite size scaling in the solar wind magnetic field energy density as seen by WIND, *Geophys. Res. Lett.* **29**(10), 2002GL016054, 2002.
- Hnat, B., S. C. Chapman, G. Rowlands, N. W. Watkins, M. P. Freeman, Scaling in solar wind epsilon and AU, AL and AE indices as seen by WIND, *Geophys. Res. Lett.*, in press, 2002GL016054, 2002.

- Hnat, B., S. C. Chapman and G. Rowlands, Intermittency, scaling and the Fokker-Planck approach to fluctuations of the solar wind bulk plasma parameters as seen by the WIND spacecraft., submitted to *Phys. Rev. E*, 2002.
- T. S. Horbury and J. M. Schmidt, Development and Effects of Turbulence in Connection with CIRS, *Space Sci. Rev.* **89**, 61–76, 1999.
- Hugill, J., Edge turbulence in tokamaks and the L-mode to H-mode transition, *Plasma Phys. Control. Fusion* **42**, R75–R91, 2000.
- Hwa, Terence and Mehran Kardar, Avalanches, hydrodynamics and discharge events in models of sandpiles, *Phys. Rev. A* **45**, 7002, 1992.
- Ivashkevich, E. V. and V.B. Priezzhev, Introduction to the sandpile model, *Physica A* **254**, 97–116, 1998.
- Jacson, J. D., *Classical Electrodynamics, second edition*, Jofn Wiley and Sons, New York, 1975.
- H. J. Jensen, *Self-Organized Criticality, first edition*, Cambridge University Press, Cambridge, 1998.
- Kadanoff, L.P., S.R. Nagel, L. Wu and S.-m Zhou, Scaling and Universality in avalanches, *Phys. Rev. A* **39**, 6524–6537, 1989.
- Kaneko, Kunihiku, *Theory and applications of coupled map lattices*, John Wiley & Sons, New York, 1992.
- Holger Kantz and Thomas Schreiber, *Nonlinear Time Series Analysis*, Cambridge University Press, Cambridge, 1997.
- Kinsey, J. E., G. M. Staebler, K. H. Burrell, M. E. Austin, and R. E. Waltz, Dynamic Modeling of Stepwise Internal Transport Barrier Formation in DIII-D Negative-Central-Shear Discharges, *Phys. Rev. Lett.* **86**, 814–817, 2001.
- Klimas, A. J., D. Vassiliadis, D. N. Baker and D. A. Roberts, The organized non-linear dynamics of the magnetosphere, *J. Geophys. Res.* **101**, 13089–13113, 1996.

- Kolmogorov, A.N., A refinement of previous hypotheses concerning the local structure of turbulence in a viscous incompressible fluid at high Reynolds number, *J. Fluid Mech.* **13**, 82-85, 1962.
- Krall, Nicholas A. and Alvin W. Trivelpiece, *Principles of plasma physics*, San Francisco Press, Inc., San Francisco, 1986.
- Krommes, J. A., Fundamental statistical description of plasma turbulence in magnetic fields, *Phys. Reports* **360**, 1-352, 2002.
- Lepping, R. P., M. Acuna, L. Burlaga, W. Farrell, J. Slavin, K. Schatten, F. Mariani, N. Ness, F. Neubauer, Y. C. Whang, J. Byrnes, R. Kennon, P. Panetta, J. Scheifele, and E. Worley, The WIND Magnetic Field Investigation, *Space Sci. Rev.* **71**, 207, 1995.
- Lindstrom, P., D. Koller, W. Ribarsky, L. F. Hodges, N. Faust, G. Turner, *Real-Time, Continuous Level of Detail Rendering of Height Fields*, Proceedings of SIGGRAPH 94 Conference, 1994.
- Lindstrom, P., and G. Turk, Fast and Memory Efficient Polygonal Simplification, *Proceedings of IEEE Visualization '98*, Research Triangle Park, North Carolina, pp. 279-286, 1998.
- Lu, E.T., and R.J. Hamilton, Avalanches and Distribution of Solar Flares, *Astrophys. J.* **380**, L89, 1991.
- Lui, A. T. Y., *et al.*, Is the Dynamic Magnetosphere an Avalanching System?, *Geophys. Res. Lett.* **27**, 911, 2000.
- Mantegna, R. N., & H. E. Stanley, Scaling behaviour in the dynamics of an economic index, *Nature* **376**, 46, 1995.
- Mantegna, R. N., & H. E. Stanley, *An Introduction to Econophysics*, Cambridge University Press, Cambridge, 2000.

- Milovanov, A. V. and L. M. Zelenyi, Fracton excitations as a driving mechanism for the self-organized dynamical structuring in the solar wind, *Astrophys. Space Sci.* **264**, 317, 1998.
- Mineshige, S., M. Takeuchi and H. Nishimori, Is a black hole accretion disk in a self-organized critical state?, *Astrophys. J.* **435**, L125–L128, 1994.
- Newman, D. E., B. A. Carreras, P. H. Diamond, and T. S. Hahm, The dynamics of marginality and self-organized criticality as a paradigm for turbulent transport, *Phys. Plasmas* **3**, 1858–1866, 1996.
- Ogilvie, K. W., D. J. Chornay, R. J. Fritzenreiter, F. Hunsaker, J. Keller, J. Lobell, G. Miller, J. D. Scudder, E. C. Sittler, R. B. Torbert, D. Bodet, G. Needell, A. J. Lazarus, J. T. Steinberg, J. H. Tappan, SWE, a comprehensive plasma instrument for the wind spacecraft, *Space Sci. Rev.* **71**, 55–77, 1995.
- Osborne, A. R., A. Provenzale, *Physica D* **35**, 357, 1989.
- E. Ott, *Chaos in Dynamical Systems* Cambridge Univ. Press, p 93, 1993.
- Padhye, N. S., C. W. Smith and W. H. Matthaeus, Distribution of magnetic field components in the solar wind plasma, *J. Geophys. Res.* **106**, 18,635–18,650, 2001.
- Paret, J. and P. Tabeling, Intermittency in the two-dimensional inverse cascade of energy: Experimental observations, *Phys. Fluids* **10**, 3126–3136, 1998.
- Pedrosa, M. A. *et al.*, Empirical Similarity of Frequency Spectra of the Edge-Plasma Fluctuations in Toroidal Magnetic-Confinement Systems, *Phys. Rev. Lett.* **82**, 3621–3624, 1999.
- Perreault, Paul and S.-I. Akasofu, A study of geomagnetic storms, *Geophys. J. R. astr. Soc* **54**, 547–573, 1978.
- Politzer, P. A., Observation of Avalanchelike Phenomena in a Magnetically Confined Plasma, *Phys. Rev. Lett.* **84**, 1192–1195, 2000.

- Price, C. P., and D. E. Newman, Using the R/S statistic to analyze AE data, *J. Atmos. Sol.-Terr. Phys.* **63**, 1387–1397, 2001.
- Rhodes, T. L., R. A. Moyer, R. Groebner, E. J. Doyle, R. Lehmer, W. A. Peebles and C. L. Rettig, Experimental evidence for self-organized criticality in tokamak plasma turbulence, *Phys. Lett. A* **253**, 181–186 , 1999.
- Sarazin Y. and P. Ghendrih, Intermittent particle transport in two-dimensional edge turbulence, *Phys. Plasmas* **5**, 4214–4228, 1998.
- Sethna, J. P., K. A. Dahmen & C. R. Myers, Crackling noise, *Nature* **410**, 242–250, 2001.
- Schertzer D., L. Larchevêque, J. Duan, V.V. Yanovsky and S. Lovejoy, Fractional Fokker-Planck equation for nonlinear stochastic differential equations driven by non-Gaussian Lévy stable noise, *J. Math. Phys.* **41**, 200–212, 2001.
- Schmittbuhl, J., J-P. Vilotte, S. Roux, Reliability of self-affine measurements, *Phys. Rev. E* **51**, 131–147, 1995.
- Sitnov, M. I., A. S. Sharma, K. Papadopoulos, D. Vassiliadis, J. A. Valdivia, A. J. Klimas, D. N. Baker, Phase transition-like behavior of the magnetosphere during substorms, *J. Geophys. Res.* **105**, 12955–12974, 2000.
- Snappen, Kim, Self-organized pinning and interface growth in a random medium, *Phys. Rev. Lett.* **69**, 3539–3542, 1992.
- Sole, R.V., and S. C. Manrubia, Extinction and self-organized criticality in a model of large-scale evolution, *Phys. Rev. E* **54**, R42-R45, 1996.
- Sornette, D., *Critical Phenomena in Natural Sciences; Chaos, Fractals, Selforganization and Disorder: Concepts and Tools*, Springer-Verlag, Berlin, 2000.
- Sorriso-Valvo, L., V. Carbone, P. Veltri, G. Consolini and R. Bruno, Intermittency in the solar wind turbulence through probability distribution functions of fluctuations, *Geophys. Res. Lett.* **26**, 1801–1804, 1999.

- Sorriso-Valvo, L., V. Carbone, P. Giuliani, P. Veltri, R. Bruno, V. Antoni and E. Martines, Intermittency in plasma turbulence, *Planet. Space Sci.* **49**, 1193-1200, 2001.
- Synakowski, E. J., Formation and structure of internal and edge transport barriers, *Plasma Phys. Control. Fusion* **40**, 581-596, 1998.
- Takalo, J., J. Timonen., and H. Koskinen, Correlation dimension and affinity of AE data and bicolored noise, *Geophys. Res. Lett.* **20**, 1527-1530, 1993.
- Takalo J., and J. Timonen., Comparison of the dynamics of the AU and PC indices, *Geophys. Res. Lett.* **25**, 2101-2104, 1998.
- Tsurutani, B. T., M. Sugiura, T. Iyemori, B. E. Goldstein, W. D. Gonzalez, S. I. Akasofu, E. J. Smith, The nonlinear response of AE to the IMF  $B_z$  driver: A spectral break at 5 hours, *Geophys. Res. Lett.* **17**, 279-282, 1990.
- Tu, C.-Y. and E. Marsch, MHD Structures, Waves and Turbulence in the Solar Wind: Observations and Theories, *Space Sci. Rev.* **73**, 1-210, 1995.
- Uritsky, V. M., A. J. Klimas and D. Vassiliadis, Comparative study of dynamical critical scaling in the auroral electrojet index versus solar wind fluctuations, *Geophys. Res. Lett.* **28**, 3809-3812, 2001.
- van Atta, C., J.T. Park, *Statistical Self-Similarity and Inertial Subrange Turbulence*, Lecture Notes in Physics, Volume 12, Edited by M. Rosenblatt and C. Van Atta, Springer Verlag, Berlin, pp. 402-426, 1972.
- van Kampen, N.G., *Stochastic Processes in Physics and Chemistry*, North-Holland, Amsterdam, 1992.
- Veltri, Pierluigi, MHD turbulence in the solar wind: self-similarity, intermittency and coherent structures, *Plasma Phys. Control. Fusion* **41**, A787-A795, 1999.
- Vespignanni, A., S. Zapperi and L. Pietronero, Renormalization approach to self-organized critical behavior of sandpile models, *Phys. Rev. E* **51**, 1711-1724, 1995.

- Vespignanni A. and S. Zapperi, Order Parameter and Scaling Fields in Self-Organized Criticality, *Phys. Rev. Lett.* **78**, 4793–4796, 1997.
- Vespignanni A., and S. Zapperi, How self-organized criticality works: A unified mean-field picture, *Phys. Rev. E* **57**, 6345–6362, 1998.
- Vassiliadis, D., A. J. Klimas, J. A. Valdivia, and D. N. Baker, The Nonlinear Dynamics of Space Weather, *Adv. Space. Res.* **26**, 197–207, 2000.
- Vlahos, L., M. Georgoulis, R. Kluiving and P. Paschos, The statistical flare, *A&A* **299**, 897–911, 1995.
- Vörös, Z., P. Kovács, Á. Juhász, A. Körmendi and A. W. Green, Scaling laws from geomagnetic time series, *Geophys. Res. Lett.* **25**, 2621–2624, 1998.
- Tam S. W., Tom Chang, S. C. Chapman and N. W. Watkins, Analytical determination of power law index for the Chapman et al. sandpile (FSOC) analog for magnetospheric activity – renormalization group analysis, *Geophys. Res. Lett.* **27**, 1367, 2000.
- Tikhanov, A. N. and A. A. Samarskii, Equations of Mathematical Physics, Reprinted by Dover, New York, 1988.
- Watt, Alan, and Mark Watt, *Advanced Animation and Rendering Techniques*, Addison-Wesley, NY, 1998.
- Watkins, N. W., S. C. Chapman, R. O. Dendy, P. Helander and G. Rowlands, Robustness of collective behaviour in strongly driven avalanche models: magnetospheric implications, *Geophys. Res. Lett.* **26**, 2617, 1999.
- Zhang, W., B. J. D. Tubbing and D. J. Ward, The effect of ELMs on energy confinement in JET, *Plasma Phys. Control. Fusion* **40**, 335–346 , 1998.